9-23-2022 2:00 PM

An in vivo investigation of short-ranged structural connectivity in the human brain

Jason Kai, *The University of Western Ontario*

Supervisor: Khan, Ali R., *The University of Western Ontario*

A thesis submitted in partial fulfillment of the requirements for the Doctor of Philosophy degree in Medical Biophysics

Abstract

Short-ranged connectivity comprise the majority of connections throughout the brain, joining together nearby regions and contributing to important networks that facilitate complex function and cognition. Despite constituting the majority of white matter in the brain and their importance, studies examining short-ranged connections have thus far been limited in part due to the challenges associated with identifying and validating them. Tractography, a computational technique for reconstructing axon trajectories from diffusion magnetic resonance imaging, has been commonly used to identify and study major white matter connections (e.g. corticospinal tract), which are easier to identify relative to the short-ranged connections. The use of additional constraints (e.g. geometry, regions of interest) together with tractography has enabled the ability to identify short-ranged connections of interest, such as the "U"-shaped tracts residing just below the cortical surface, and the subcortical connectome tracts found deeper in the brain.

In this thesis, we aimed to quantify the reliability of such techniques for studying the short-ranged connections and applied them to examine changes to short-ranged connectivity in patients with first episode schizophrenia. First, the reliability of identifying short-ranged, "U"-shaped tracts is examined in Chapter 2, leveraging geometric constraints for identifying the "U"-shaped geometry together with clustering techniques to establish distinct tracts. Here, we use two different clustering techniques, applying them to two datasets to study both the reliability of identifying short-ranged, "U"-shaped tracts across different subjects and in a single individual (across different sessions). In Chapter 3, the reliability for identifying the subcortical connectome (short-ranged connections between subcortical structures) is evaluated. Connectivity of the deep brain is often hard to recapitulate due to the multiple orientations contributing to complex diffusion signals. Thus, we leveraged regions of interest determined through histological data to aid identification of the short-ranged connections in the compact region. Finally, Chapter 4, uses the techniques from Chapter 2 in combination with quantitative measures sensitive to microstructural changes to study changes to short-ranged, "U"-shaped tracts in the frontal lobes of patients with first-episode schizophrenia (FES). By studying the short-ranged connections in patients with FES, biomarkers associated with clinical presentation may be elucidated and may aid the current understanding to improve future treatment. Overall, the projects presented here quantify the reliability of current techniques for investigating short-ranged connectivity and provide a framework for evaluating future techniques. Additionally, the techniques evaluated here can be used to elucidate new findings and improve treatment in clinical populations.

Keywords: diffusion magnetic resonance imaging, diffusion tensor imaging, tractography, short-ranged structural connectivity, reliability, schizophrenia

Summary for Lay Audience

Similar to how roads and highways join nearby cities, basic human functions are made possible through the structural connections (e.g. roads and highways) that connect different regions of the brain (e.g. cities). Much like the roads (joining local landmarks) and highways (joining cities far apart), the brain also has both short and long-ranged connections. Using diffusion magnetic resonance imaging (dMRI), scientists are able to study these connections non-invasively. As with any technique, especially one that is used to non-invasively study the brain, confidence of a method improves with reliability. That is, when a method is applied multiple times, similar results should be produced across different healthy individuals. The current thesis evaluates the reliability of current techniques to study the short-ranged connections of the human brain.

Once reliability of the techniques to study connections of the brain has been established, the same techniques can be applied to examine how such connections can change due to disease. For example, we can measure properties such as the integrity along the length of the connection. In a patient, we may see reduced integrity along it's length, similar to how a pothole may be encountered along a highway between two cities. Such changes may identify important associations with experienced symptoms and help us understand the progression of disease. Furthermore, identifying these changes can help to improve the treatment administered through better understanding of how the brain changes.

Short-ranged connections found just below the surface of the brain demonstrate a unique "U"-shaped geometry. Using geometric constraints with tractography, reliability of identifying these connections are evaluated both across different individuals and in the same individual at different timepoints in Chapter 2. Chapter 3 examines the reliability of short-ranged connections found connecting regions deep below the surface of the brain. Identification of these deep connections is complicated due to the various crossing connections muddying the signal in a small, condensed region. After establishing reliability in Chapter 2, we use the same technique to identify similar connections, examining for changes along its length in patients with first-episode schizophrenia. Altogether, we quantify the reliability of current methods for investigating short-ranged connections, while also providing a framework for evaluating new techniques in the future. Furthermore, we demonstrate how these techniques can be used to improve our current understanding of changes to the brain's connections due to schizophrenia or other diseases.

Co-Authorship Statement

Chapter 1:

J. Kai — sole author

Chapter 2:

J. Kai — data processing, analysis, wrote manuscript

A.R. Khan — project conception, reviewed manuscript

Chapter 3:

J. Kai — project conception, methodology, analysis, wrote manuscript

A.R. Khan — methodology, resources, reviewed manuscript

R.A.M. Haast — project conception, methodology, reviewed manuscript

J.C. Lau — project conception, reviewed manuscript

Chapter 4:

J. Kai — methodology, analysis, wrote manuscript

M. Mackinley — data collection, reviewed manuscript

A.R. Khan — methodology, resources, reviewed manuscript

L. Palaniyappan — project conception, reviewed manuscript

Chapter 5:

J. Kai — sole author

Dedicated to my mother (媽媽; 吳淑美) and father (爸爸; 奚祖義), who worked hard through difficult times and made so many sacrifices for our family.

Acknowledgments

First, I would like to express my gratitude to my supervisor, Dr. Ali Khan, for giving me an opportunity to join his lab, providing mentorship and support over the past 6 years. The incredible experience has brought along countless opportunities and have helped develop new skills. I am also grateful to have witnessed the growth of the lab and have had the chance to work along-side an amazing group of people.

I would also like to extend my thanks to my advisory committee, Dr. Sandrine de Ribaupierre, Dr. Aaron Ward, and Joe Gati, who provided invaluable guidance throughout this degree.

There are a number of incredible individuals that also helped to shape this experience. To the many past and present members of the Khan lab, thank you for the many discussions that have been had over coffees, at the grad club or over a hockey / basketball game. To Drs. Jordan DeKraker, Roy Haast, Jonathan Lau, and Loxlan Kasa for your guidance since I first joined the lab. To Dr. Olivia Stanley and Tristan Kuehn for their help with Brainhack Western events and their willingness to help with any programming or software related questions.

To all of the friends I've made since I've started this journey - Dr. Dickson Wong, Dr. Geoffrey Ngo, Hossein Rejali, Dimuthu Hemachandra, Brad Karat, Mary Taylor, and many more, thank you for making this experience a memorable one and providing a sense of normalcy during these past few uncertain years.

None of this would have been possible without the unwavering love and support of my parents and the sacrifices they have made. Thank you for teaching me to be curious, to persevere through difficult times, and for encouraging me to try new things no matter what they are.

To our dog, Finnegan, thanks for providing unconditional love and for sometimes being a great therapy dog. You are always there to bring me down to earth by biting my ankles or cuddling on the couch / floor during a low.

To my partner, Lauren Smith, I am forever grateful for your endless love and support. Thank you for pushing me to be my best self and for helping me live a more balanced lifestyle. I am excited to continue our adventures together.

Contents

List of Figures

List of Tables

List of Appendices

List of Abbreviations, Symbols, and Nomenclature

General Terminology

σ	Standard deviation
μ	Average
3D	3-dimensional
3T	3 Tesla
ANCOVA	Analysis of covariance
ANOVA	Analysis of variance
ANTS	Advanced normalization tools
AD	Alzheimer's disease
AFD	Apparent fibre density
ASD	Autism spectrum disorder
CGI-S	Clinical global impression scale
CSF	Cerebrospinal fluid
CST	Corticospinal tract
CV	Coefficient of variation
DBS	Deep brain stimulation
DSM	Diagnostic and statistical manual of mental disorders
DUP	Duration of untreated psychosis
ENIGMA	Enhancing Neuroimaging Genetics through Meta-Analysis consortium
FES	First episode schizophrenia
FOV	Field of view
GM	Grey matter
GPE	Globus pallidus externa
GPI	Globus pallidus internus
HCP	Human Connectome Project
ICC	Intraclass correlation
MCI	Mild cognitive impairment
MD	Mediodorsal nuclei of the thalamus
MS	Multiple sclerosis
NHP	Non-human primates
PANSS-8	Positive and negative syndrome scale - 8 items
PD	Parkinson's disease
QB	QuickBundle
ROI	Region of interest
SC	Spectral clustering
SOFAS	Social and occupational functioning assessment scale
STN	Subthalamic nucleus
VA	Ventroanterior nucleus of the thalamus
VLa	Ventrolateral anterior nucleus of the thalamus
VLp	Ventrolateral posterior nucleus of the thalamus
wDSC	Weighted Dice similarity coefficient
WM	White matter

Medical Imaging Terminology

AxD	Axial diffusivity
CSD	Constrained spherical deconvolution
dMRI	Diffusion magnetic resonance imaging
DTI	Diffusion tensor imaging
DWI	Diffusion weighted imaging
FA	Fractional anisotropy
FOD	Fibre orientation distribution
HARDI	High angular resolution diffusion imaging
iFOD2	Second-order integration over fiber orientation distributions
MD	Mean diffusivity
MP2RAGE	Magnetization prepared rapid gradient echo
MRI	Magnetic resonance imaging
MSMT-CSD	Multi-shell, multi-tissue constrained spherical deconvolution
NODDI	Neurite orientation dispersion and density imaging
NHP	Non-human primate
NMR	Nuclear magnetic resonance
PGSE	Pulsed gradient spin-echo
RD	Radial diffusivity
RF	Radiofrequency
SIFT	Spherical-deconvolution informed filtering of tractograms
SIFT2	Spherical-deconvolution informed filtering of tractograms, version 2
T1w	T1-weighted
TE	Echo time
TI	Inversion time
TR	Repetition time

Terms Introduced by this Thesis

LHSC	London Health Sciences Center
MDF	Minimum average, direct-flip
PEPP	Prevent and Early Intervention Psychosis Program
TMT-B	Trail Making Test

Chapter 1

Introduction

1.1 Motivation and overview

The human brain is composed of an abundance of neurons making up the grey matter (GM) joined together by myelinated axons comprising the white matter (WM). Axons that join the same regions tend to form bundles (or tracts) [1], facilitating communication between the connected regions. Existence of complex, structurally connected networks of brain regions are associated with function and cognition [2]. These networks are composed of heterogeneous tracts varying in length and trajectory. While there have been extensive studies investigating tracts joining distant brain regions, much less is known about the short-ranged tracts which make up the majority of connections that can be found throughout the brain [3]. Practical and technical limitations associated with reconstruction methods pose a challenge in studying the brain's structural connectivity. Additionally, individual subject variability adds an additional degree of difficulty of identifying corresponding tracts across individuals.

In this introductory chapter, a brief review of short-ranged tracts, found below the surface and in the deep regions of the brain, is provided. Methods of investigating the structural connections are explored with a detailed focus on diffusion magnetic resonance imaging (MRI), a non-invasive technique. Recent studies investigating short-range connectivity in both healthy and clinical populations are also reviewed.

1.2 Structural connectivity

Of the structural connectivity found within the brain, the myelinated axons joining the different brain regions and forming complex networks can be broadly categorized into three groups: (1)

intracortical, (2) short-ranged, or (3) long-ranged tracts. Intracortical axons are the shortest of the three axon groups, with a tendency to project within the GM and are difficult to study in humans with current *in vivo* methods [1]. Long-ranged tracts are the longest of the three groups, joining distant brain regions with trajectories projecting between distant regions as well as into the regions deep below the cortical surface. These tracts also demonstrate similar trajectories across individuals [4] and have been studied extensively relative to the other two groups. The final group of axons are the short-ranged tracts, which can be further separated into two sub groups: cortico-cortical and subcortico-subcortical. Cortico-cortical tracts are between the intracortical and long-ranged tracts in length and can be found just below the cortical surface, closest to the GM. These tracts are also referred to as "U"-fibres (after the shape of its trajectory, following along the gyri and sulci) and comprise the superficial white matter together with intracortical axons. It has been hypothesized that the tract length of the superficial WM is inversely proportional to the total density of the group of tracts (e.g. shorter tracts comprise a larger volume of WM) [1]. Deep below the surface of the brain, subcortico-subcortical tracts can be found, connecting the structures within the compact region surrounding the ventricles and near the brainstem [5]. Figure 1.1 displays examples of short-ranged and long-ranged tracts.

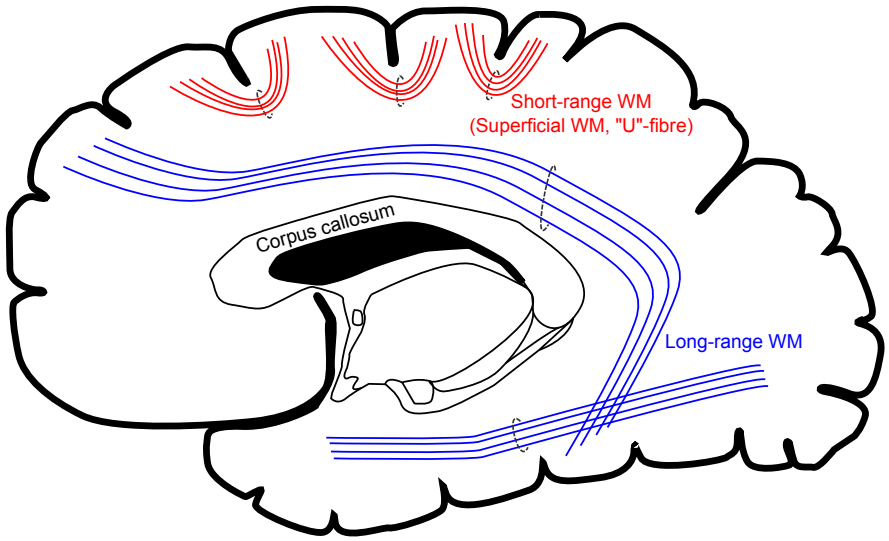

Figure 1.1: Example of long-ranged tracts (blue) and short-ranged, "U"-shaped tracts (red) found within the brain. Not shown in this figure are the intracortical and subcortico-subcortical tracts.

The following subsections will explore the short-ranged structural connectivities of the brain, specifically the "U"-fibres and subcortico-subcortical tracts respectively, in more detail.

1.2.1 "U"-shaped WM

Existence of short-ranged tracts was first acknowledged in the late 19th century, described initially as short association fibres found immediately below the grey matter of the cortex [3, 6]. The trajectory of the "U"-shaped tracts follow along the cortical folds, starting from one gyrus, projecting downwards towards the sulcus before curving back upwards toward the nearby gyri. Theodor Meynert noted the "U"-shaped projections may connect more than adjacent gyri, extending to nearby gyri that are two or more folds away and having an important role in cognition [7, 8]. Meynert's observations led him to believe that short-ranged tracts were not local to a specific region, but could be found throughout the brain.

Initial studies of "U"-shaped tracts primarily involved the occipital lobe, followed by the frontal lobe shortly after in post-mortem brains, patient observations and experimental animal studies [8]. Some of the earliest mappings of "U"-fibres resulted from separating the fibres along their natural fissures by involving fixed brain tissue and gas-compressed liquid carbon dioxide [8, 9]. These early mappings identified the primary trajectory of numerous short-ranged fibres found throughout the human brain [8]. Of the brain's WM, "U"-shaped fibres often develop into late adulthood and are amongst the last to be fully myelinated (with some exceptions in the occipital lobe) [10]. The late maturation relative to the long-ranged tracts tends to result in thinner myelination encapsulating the axon and may offer less protection as a result, increasing the vulnerability to disease processes [10]. Studies involving patient populations with neurological and psychiatric conditions have implicated the "U"-shaped tracts, identifying abnormalities in tract densities and quantitative metrics associated with microstructural properties [11, 12].

1.2.2 Subcortico-subcortical WM

Deep GM structures are often involved in key cognitive and functional processes, with structures like the thalamus acting as a hub of information processing [13–15]. These structures, much like GM structures found more superficially, are also connected by WM tracts that enable the relaying of information. Deep GM structures can be found connecting to either cortical areas or to other nearby deep GM structures [5]. Knowledge of the WM tracts connecting deep GM structures was primarily discovered through studies of animal models and descriptions dating back to the late 19th century [13]. Through tracer studies involving non-human primates (NHP), valuable knowledge regarding the terminal ends of the deep subcortical WM tracts has been gained, but detailed information of associated trajectories have remained elusive [13]. In studies of the human brain, post-mortem tissue dissection can be performed with Klingler's

method, a freeze-thaw technique coupled with careful, time-consuming layer-by-layer peeling of WM tissue [16]. This technique has been applied to reveal the trajectory of certain WM tracts, however identification of the specific tract revealed is difficult. Nonetheless, identification of the deep WM is important as they form the connections of important functional and cognitive networks [5] (see example shown in Figure 1.2). Furthermore, it has been shown that there are important surgical targets, such as for therapeutics, where deep brain stimulation has been applied in treating some movement disorders [17].

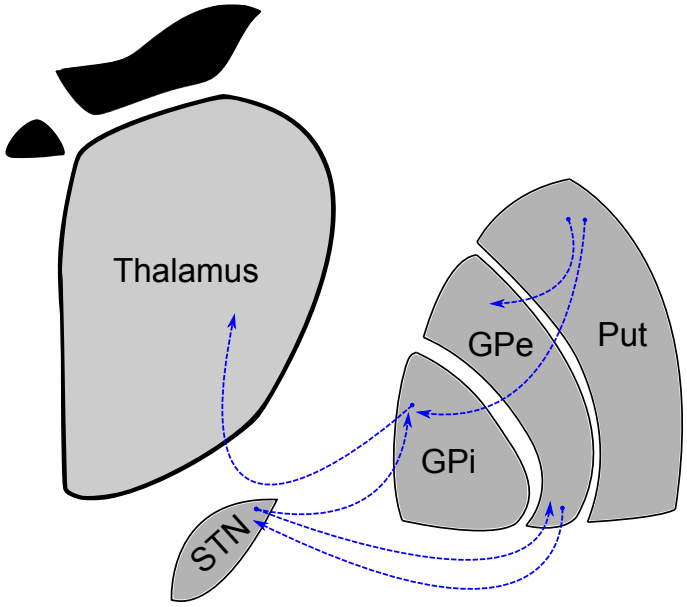

Figure 1.2: Example of connections between subcortical structures (located in the deep brain). These connections have been identified as part of the motor circuit and connect to other regions of the brain (e.g. cerebellum, cortex, brainstem) that are not shown.

Recent advances in imaging techniques may provide non-invasive approaches to studying the short-ranged, deep subcortical connectivity, as well as the short-ranged "U"-shaped WM.

1.3 Magnetic resonance imaging

Magnetic resonance imaging (MRI) has been widely adopted in the field of neuroimaging to study the brain's anatomical structure, function, and connectivity. The history of MRI begins in the early 20th century with nuclear magnetic resonance (NMR). First described in 1938, Isidor Rabi observed the ability to detect the magnetic resonance of atomic nuclei in molecular beam experiments [18] and the same phenomenon was independently observed to occur in liquids and solids by Felix Bloch and Edward Purcell in 1946 [19, 20]. More than two decades later, Richard Ernst developed the Fourier transform technique for NMR spectroscopy in 1966, sug-

gesting the frequency response of an observed signal contained more explicit information and could be utilized for spatial encoding [21]. Paul Lauterbur and Peter Mansfield independently described localization of signals using magnetic field gradients in 1973, which form the foundation of present day MRI [22, 23]. In 1975, the application of Fourier transforms for image formation was described [24], leading to the first human magnetic resonance images captured in 1977. Another study of note is the foundational work for diffusion MRI described by Erwin Hahn in 1950 to observe molecular diffusion in liquids [25].

In the following subsections, the fundamentals of MRI, extending to diffusion MRI (dMRI), is described, along with diffusion models (both statistical models used throughout this thesis and biophysical models), and tractography, a technique derived from information acquired with dMRI to investigate brain connectivity.

1.3.1 Basics of MRI

Derived from NMR, magnetic resonance imaging captures the signal emitted from the nucleus of an atom with a magnetic moment (nuclear spin) causing it to act as a tiny magnet as a result of an odd number of protons or neutrons [26, 27]. When placed in a static external magnetic field (B_0), such as the main magnetic field of an MRI, the nuclear spins attempt to align in one of two orientations: parallel (a lower energy state) or anti-parallel (a higher energy state) [26, 27]. Due to the differences in energy states, the majority of nuclear spins will align in parallel resulting in a net magnetization ($\vec{M}$) in the direction of the external field [26,27]. By convention, the direction of the field is longitudinal along the $\vec{z}$ direction. The protons in this field continue to precess at the Larmor frequency determined by:

$$f_0 = B_0 \times \frac{\gamma}{2\pi} \tag{1.1}$$

The prcession frequency is proportional to the external magnetic field by a gyromagnetic ratio ($\gamma/2\pi$) for a given atomic nuclei. Found in abundance as water in the human body, hydrogen has a gyromagnetic ratio of 42.576 MHz/T [26].

In the presence of only the external magnetic field, the net magnetization at equilibrium can be computed with the following equation:

$$\vec{M}_0 = \frac{\rho\gamma^2\hbar\vec{B}_0}{4k_BT} \tag{1.2}$$

where ρ is the proton density, $\hbar$ is Plank's constant, k_B is Boltzmann's constant and T is the temperature (in Kelvin). The net magnetization, as defined by equation 1.2, can be influenced to improve sensitivity to the emitted signal by increasing the density of protons, increasing the strength of the external magnetic field, or by decreasing the temperature.

The net magnetization experienced is much smaller than the magnetization of the external magnetic field, making it difficult to separate the signal from the magnetic field [26]. Instead, a transmit radiofrequency (RF) coil is used to apply a RF pulse (B_1), exciting the spins to a higher energy state to tip the net magnetization, typically perpendicular to the main magnetic field, where protons continue to precess in-phase at the Larmor frequency. When the application of the RF pulse is stopped, the spins begin to dephase rapidly, returning to its equilibrium state [26]. As the net magnetization returns to equilibrium, a fading electrical signal is induced. Rather than record this dampening signal, a receiver RF coil records an echo of this original signal, created by applying additional RF pulses (described in the following subsection) [26].

In addition to the magnet that produces the main magnetic field and the RF coils, the MRI also consists of 3 orthogonal gradient coils which aid in spatially localizing the signal by linearly altering the magnetic field [26, 27]. Relative to the main magnetic field, these perturbations are much smaller in magnitude. The minor linear changes in field strength spatially encode the atomic nuclei by altering the frequency and phase of the nuclear spins and also enable selection of slices of interest of an imaged object [26]. By varying the time and magnitude that gradient and RF coils are turned on (e.g. MRI sequence), images with particular characteristics can be produced (Figure 1.3).

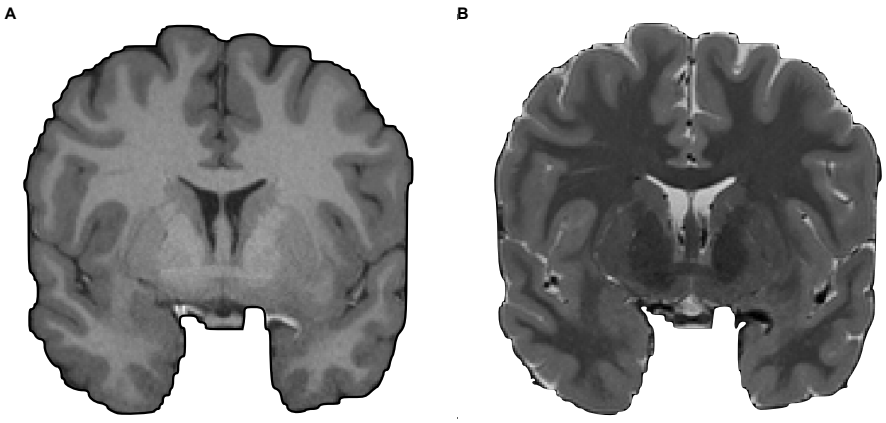

Figure 1.3: Two images of the same individual is displayed with different contrasts, acquired by altering the parameters of the MRI sequence: (A) T1-weighted (B) T2-weighted.

1.3.2 Diffusion MRI

Diffusion is the motion molecules experience due to thermal agitation, otherwise known as Brownian motion. In an unconstrained environment, the diffusion process appears isotropic (i.e. equal in all directions). However, in a constrained environment, such as within the brain, the diffusion of water molecules is impeded by the barriers created from surrounding cell walls and axonal fibres [28]. These barriers result in an anisotropic diffusion of water molecules with a preferential direction parallel to its barriers. An example is shown in Figure 1.4. Using diffusion-sensitive sequences, MRI can capture 3-dimensional (3D) volumes sensitive to a particular direction of diffusion, enabling probing of microstructural environments [29].

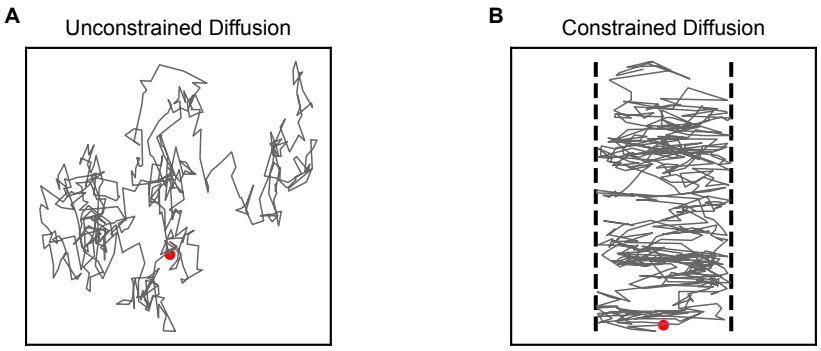

Figure 1.4: Example of molecule diffusing in an (A) unconstrained environment vs (B) constrained environment. The red dot indicates the starting position. In the constrained environment, the diffusion is hindered such that the preferential direction of diffusion is parallel to the barrier (dashed lines).

First developed by Edward Stejskal and John Tanner in 1965, the pulsed gradient spin echo (PGSE) sequence (also referred to as the Stejskal-Tanner sequence) [30] can be used to observe diffusion in the form of signal attenuation. An example of a PGSE sequence is shown in Figure 1.5. Briefly, spin-echo pulse sequences apply two excitation RF pulses: (1) a 90° pulse tipping the net magnetization perpendicular to the main magnetic field and (2) a 180° pulse applied some time following the 90° pulse causing the nuclear spins which were dephasing to rephase, creating an echo [26, 27]. In a PGSE sequence, on either side of the 180° RF pulse, are two identical gradients placed symmetrically to create a diffusion-sensitive signal. The first gradient induces a unique phase change in the nuclear spins to spatially encode the position of the atomic nuclei. Following the 180° RF pulse, in the absence of diffusion, the second gradient results in an identical phase change, resulting in no net displacement of the atomic nuclei and subsequently no signal attenuation [26]. If diffusion occurs, the second gradient would induce a phase change much different than the first gradient and a signal attenuation would be observed [26, 28, 30]. The diffusion-weighted signal can be computed with following

equation:

$$S = S_0 e^{-bD} \tag{1.3}$$

where S_0 is the initial signal, D is the diffusion coefficient of the tissue (measured in mm^2/s) and b is the diffusion attenuation factor (measured in s/mm^2). The diffusion attenuation factor, also termed "b-value" is often used to describe the diffusion weighting associated with a particular diffusion sequence [28].

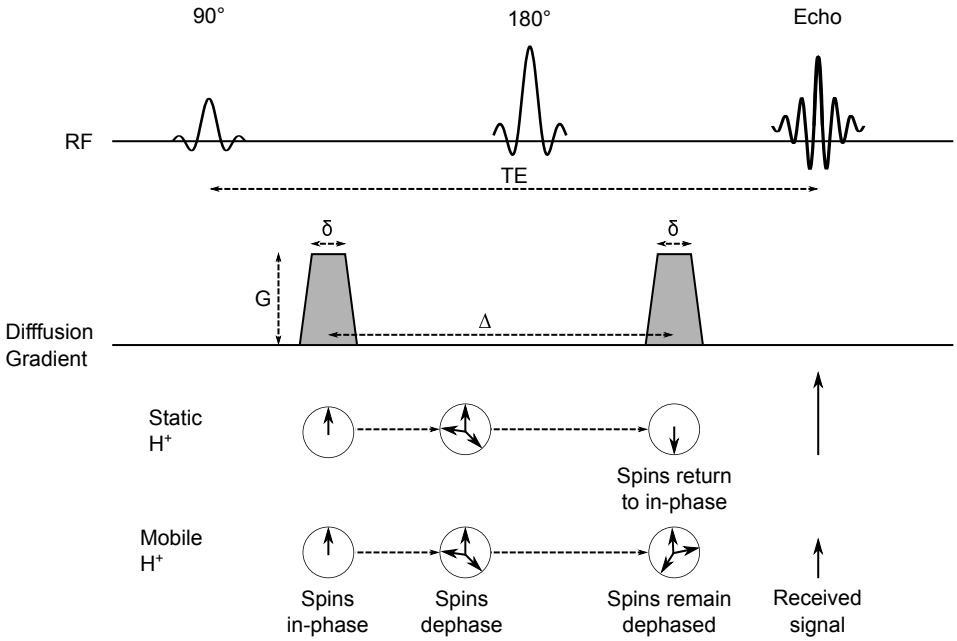

Figure 1.5: Example of a PGSE sequence is shown, displaying both apply and receive RF pulses and diffusion gradients. Not seen are the imaging gradients for slice selection, phase encoding and frequency encoding. First a 90° RF pulse is applied, followed by a 180° RF pulse some time later. On either side of the 180° RF pulse are two identical diffusion gradients. In the presence of diffusion, an attenuated signal (echo).

By manipulating the gradient strength (G), gradient pulse width (δ), and the timing between the two diffusion gradients (Δ), the diffusion weighting can be altered [28]. The b-value can be numerically determined by:

$$b = \gamma^2 G^2 \delta^2 (\Delta - \frac{\delta}{3}) \tag{1.4}$$

Diffusion imaging typically acquires multiple 3D diffusion weighted volumes sensitive to specific directions interspersed with non-diffusion weighted (b=0 s/mm^2) volumes. Early diffusion imaging studies that acquired multiple directions relied on a single diffusion weighting, referred to as "single-shell" diffusion. This enabled the ability to perform simple diffusion modelling. In recent years, studies have increasingly employed diffusion sequences acquiring diffusion volumes with multiple diffusion weightings, referred to as "multi-shell" diffusion,

in order to perform complex diffusion modelling and can enable separation of different tissue components (e.g. WM vs GM vs cerebrospinal fluid). Both a simple diffusion model and one of the complex diffusion models will be explored in detail in the following subsection.

1.3.3 Diffusion models

As noted in the previous subsection, diffusion is anisotropic when impeded. This anisotropy was observed in 1990 by Michael Moseley, who noted a contrast change in the diffusion weighted image of the brain dependent on the direction the diffusion measurement was taken [29]. A year later, Phillip Douek suggested this finding could be used to map the brain's axonal fibres [31], laying the foundation to what would eventually lead to diffusion tractography (described in the following subsection). In 1994, Peter Basser proposed the use of tensors to describe the local diffusivity, coining the term diffusion tensor imaging (DTI) [32]. The diffusion tensor is described by:

$$D = \begin{bmatrix} D_{xx} & D_{xy} & D_{xz} \\ D_{yx} & D_{yy} & D_{yz} \\ D_{zx} & D_{zy} & D_{zz} \end{bmatrix} \tag{1.5}$$

where the off-diagonal terms are redundant (e.g. $D_{xy} = D_{yx}$). The diffusion tensor can be defined by acquiring diffusion weighted acquisitions along the 3 principal and 3 off-principal directions with an additional non-diffusion weighted (b=0 s/mm^2) acquisition to compute diffusivity. Following determination of the tensor terms, the eigenvalues of the diffusion tensor can be computed to model the local diffusion as an ellipsoid, describing the ellipsoid's principal axes (see Figure 1.6). If the diffusion is anisotropic, the diffusion ellipsoid's long-axis is oriented in the main direction of diffusion. However, if the diffusion is isotropic, the three eigenvalues of the diffusion tensor are equal and the ellipsoid takes on a spherical shape.

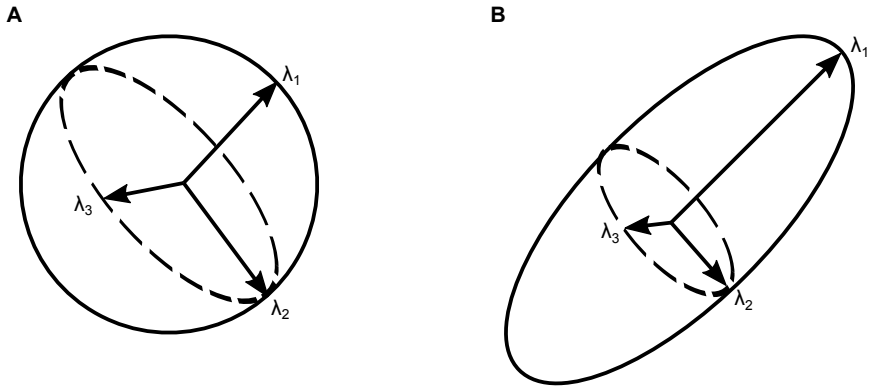

Figure 1.6: Examples of (A) isotropic and (B) anisotropic diffusion tensors are shown. In an isotropic tensor, $\lambda_1 \approx \lambda_2 \approx \lambda_3$. In an anisotropic tensor, $\lambda_1 > \lambda_2 \geq \lambda_3$, where λ_1 describes the primary diffusion direction.

DTI not only provided a way to model the local diffusivity with an ellipsoid, but also provided a means to describe the diffusivity with scalar metrics:

Mean diffusivity (MD) describes the average diffusion in the three principal directions:

$$MD = \frac{\lambda_1 + \lambda_2 + \lambda_3}{3} \tag{1.6}$$

Axial diffusivity (AxD) reflects the magnitude of diffusion in the tensor's principal direction:

$$AxD = \lambda_1 \tag{1.7}$$

Radial diffusivity (RD) describes the average magnitude of diffusion in the tensor's perpendicular (secondary and tertiary) directions:

$$RD = \frac{\lambda_2 + \lambda_3}{2} \tag{1.8}$$

Fractional anisotropy (FA) is a value between 0 (completely isotropic) to 1 (completely anisotropic) reflecting the diffusion's degree of anisotropy:

$$FA = \sqrt{\frac{(\lambda_1 - \lambda_2)^2 + (\lambda_2 - \lambda_3)^2 + (\lambda_1 - \lambda_3)^2}{2(\lambda_1^2 + \lambda_2^2 + \lambda_3^2)}} \tag{1.9}$$

With its relative simplicity, DTI was adopted for many *in vivo* studies of the brain and is still widely used in present day investigations. Scalar metrics are often correlated with cognition and sometimes identified as potential biomarkers of disease. However, it was also noted early

on that as a result of its simplicity and assumption of a single diffusion orientation, it may fail to correctly model the diffusion in regions where barriers are complex [33]. Figure 1.7 demonstrates examples of complex orientations that can be encountered. One such example are regions where two separate axonal fibre bundles with differing orientations may cross resulting in either a single principal orientation or the appearance of isotropic diffusion when modelled. In reality, imaging voxels often contain multiple axonal orientation configurations [34], limiting the accuracy of the simplistic DTI model.

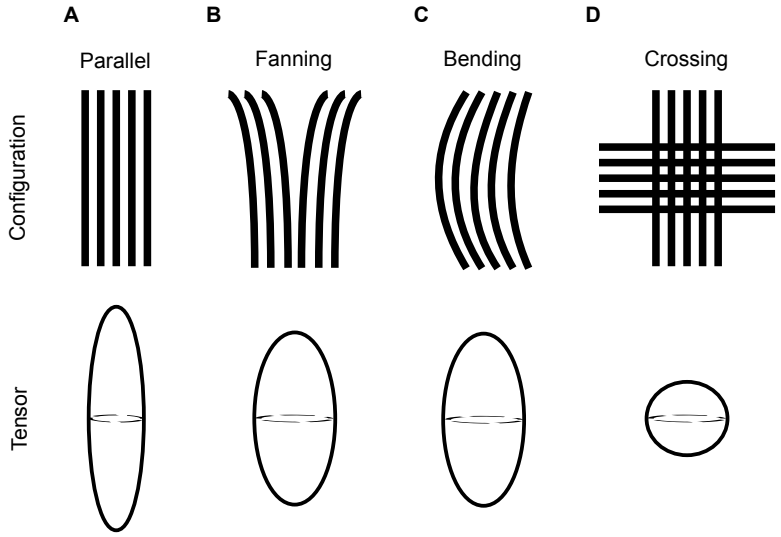

Figure 1.7: Different possible orientations encountered within the brain are shown and described in the context of DTI: (A) Parallel, a single coherent orientation forming an anisotropic tensor. (B) Fanning, anisotropic tensor that has increased radial diffusivity due to increased perpendicular diffusion (C) Bending, anisotropic tensor appearing less anisotropic, similar to fanning. (D) Crossing, a case of perpendicular crossing results in an isotropic appearing diffusion tensor.

To overcome some of the limitations of DTI, including the orientation assumption, some studies have adopted the high angular resolution diffusion imaging (HARDI) technique, first described in 2002 by Daniel Alexander [35]. A diffusion acquisition is typically considered HARDI when a large number of unique gradient directions are employed (e.g. > 30 directions). The HARDI technique enables the ability to model multiple axonal orientations within an imaging voxel by relying on the signal from the different gradient directions. Each direction-sensitive diffusion signal can be thought of as a point on a sphere, where a spherical harmonic series can be used to model the data. One such model used throughout the studies in this thesis is the constrained spherical deconvolution (CSD) model.

First proposed in 2004 for dMRI, spherical deconvolution models the fibre orientation distribution (FOD) function, which represent the fraction of fibres along an orientation [36]. The

spherical harmonic representation of the diffusion signal is modelled as a convolution, computed by the following equation:

$$S(\theta, \phi) = R(\theta) \circledast F(\theta, \phi) \tag{1.10}$$

where $R(\theta)$ is the axially symmetric response function and $F(\theta, \phi)$ represents the FOD function.

To obtain the FOD function, a deconvolution is performed between the diffusion signal and response function, which can be estimated from the diffusion profile, ideally in regions with a high degree of anisotropy, which consequently represents a single fibre orientation. Additionally, the maximum spherical harmonic order is determined by the number of gradient directions, with improved angular resolution and a higher sensitivity to noise at higher harmonic orders [36]. The number of directions required for a given spherical harmonic order can be computed:

$$N = \frac{(l + 1)(l + 2)}{2} \tag{1.11}$$

where N is the number of gradient directions and l is the spherical harmonic order.

Contribution from noise may introduce physically impossible, negative valued FODs [36]. The constrained spherical deconvolution model removes negative values by imposing a non-negativity constraint [37]. Using diffusion phantoms and a HARDI acquisition, the CSD model has been shown to resolve multiple fibre orientations with crossing angles up to 30° [38].

The two previously described models (DTI and CSD) describe the behaviour of diffusion (i.e. describe the orientation) and are also sometimes referred to as statistical models [39]. Statistical models make no assumptions about the underlying tissue structures, but can indirectly characterize the microstructural environment [39]. Biophysical models have also been derived from dMRI, providing relevant estimates to biological properties of tissue [39]. Assumptions are made regarding the orientation of the tissue when applying biophysical models in order to estimate parameters describing different tissue compartments (e.g. intra-axonal vs extra-axonal vs CSF). One such example of a biophysical model is the Neurite Orientation Dispersion and Density Imaging (NODDI) model, which as its name suggests, estimate the neurite density and orientation dispersion to describe the microstructural environment [40].

1.3.4 Tractography

The previously described statistical models are two of many developed diffusion models, which can be used to estimate the local diffusion orientations within an imaging voxel. By following the local orientations voxel-by-voxel, the trajectory of an axon can be estimated (see Figure 1.8).

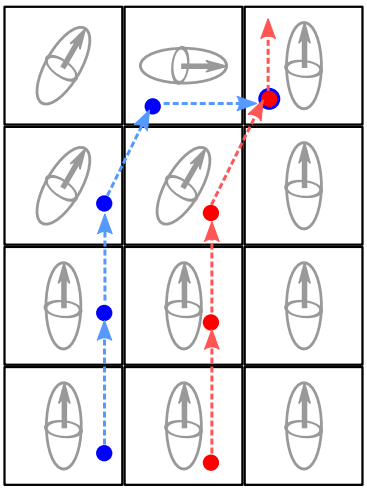

Figure 1.8: Simplified example demonstrating tractography processing of following local orientations. Here two different streamlines are generated (red and blue), each following the primary diffusion orientation in each voxel.

Computationally, the axonal trajectories are represented by a streamline, which are generated by resolving the curve which join a discrete set of directions. The method of estimating axonal trajectories from dMRI is known as tractography, where generated streamlines are stored as tractograms. Additionally, tractography also requires a set of seeds, which represent the spatial locations where tracking begins, and a set of stopping parameters, in which streamline propagation is terminated. Tractography can be broadly categorized into two groups of algorithms: deterministic and probabilistic [41].

Deterministic tractography algorithms propagate streamlines in a predictable manner. Commonly, streamlines are propagated in the direction most similar to the previous propagation step [42, 43] until termination criteria are met (e.g. maximum angle, minimum FA). Early tractography studies adopted deterministic approaches to reconstruct axonal trajectories of the brain. While these methods are able to reproduce the main trajectory of a tract, it often fails to capture branching within a tract (e.g. corticospinal tract; Figure 1.9) [44]. Another criticism of deterministic algorithms include its sensitivity to anisotropic orientation, resulting in a failure to capture all parts of a tract (i.e. false negatives) due to an inability to capture streamlines that

follow secondary or tertiary diffusion directions or failing due to apparent anisotropy [45].

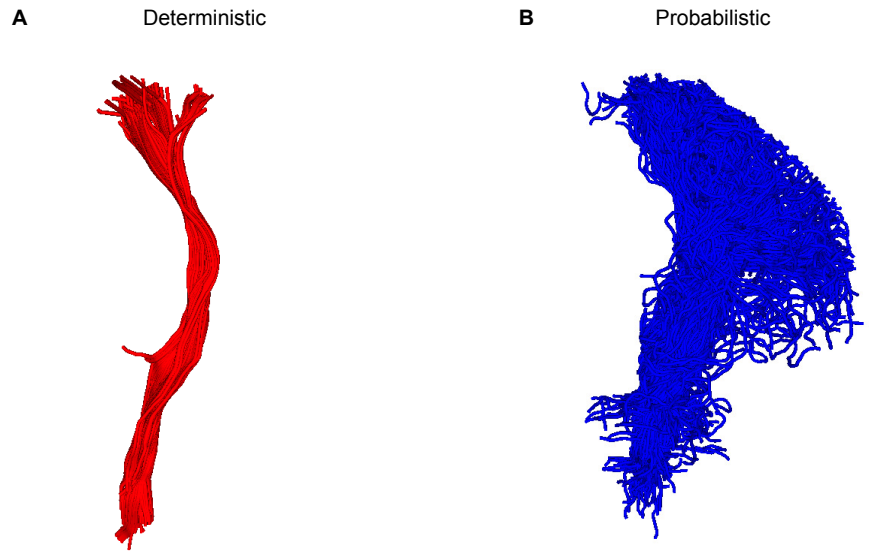

Figure 1.9: The corticospinal tract reconstructed with tractography using (A) deterministic and (b) probabilistic algorithms using identical parameters. The deterministic algorithm is only able to reconstruct the main trunk, while the probabilistic algorithm is able to recapitulate the fanning (seen in the superior portion of the tract).

Similar to deterministic tractography algorithms, probabilistic tractography algorithms also generate streamlines by propagating trajectories in a step-wise manner. However, instead of propagation in a predictable manner, the tracking direction is chosen at random based on a distribution of possible orientations [46, 47]. Since probabilistic algorithms were first introduced, more studies have opted to adopt a probabilistic approach as it is more robust to noise [46] and considered to be better at reconstructing axonal trajectories [41, 47]. Spurious streamlines (i.e. deviation from true trajectory) often stray from the trajectory demonstrated from the main group of streamlines belonging to a tract and are characterized with lower probability [46]. A potential pitfall of probabilistic methods lies in the ability to determine whether a streamline is spurious [47]. Additionally, probabilistic algorithms tend to be more computationally intensive than its deterministic counterpart [47].

1.3.5 Tract identification

Regardless of the choice of algorithm, tractography can generate the connectivity throughout the brain. Identification of tracts joining different brain regions (i.e. determine streamlines belonging to an axonal bundle) poses another challenge. Additional post processing steps, which can be categorized as supervised or unsupervised [48], need to be taken to identify tracts

from generated streamlines. The following subsection will describe the different techniques employed to identify these pathways.

One method of identifying a tract is by employing supervised techniques, which require individuals to manually place inclusion and exclusion regions of interests (ROI) to retain and remove streamlines respectively [48]. The ROIs may be manually drawn [49] or can be derived from an existing atlas [50]. Manual placement of ROIs is a time-consuming process and requires anatomic knowledge to correctly identify and extract a tract of interest [48]. Use of an atlas with predefined ROIs can partially automate this process following a registration between subject data and the atlas [48]. However, this process still requires anatomical knowledge in order to correctly select relevant ROIs to identify a tract of interest, while also necessitating the need for an adequate registration [48]. These supervised techniques can also be thought of as targeted tractography, utilizing *a priori* knowledge to find the tract of interest.

Unsupervised techniques are another method of identifying tracts, relying on the features of the streamlines for identification of a tract. Often, these methods include examining the trajectory of a streamline and clustering algorithms to group together streamlines with similar trajectory [51–53]. While these methods eliminate the need to manually draw ROIs, much like the partially automated supervised techniques, an adequate registration is still required to establish correspondence of tracts between individual subjects [48]. Additionally, unsupervised techniques have the difficulty of dealing with streamlines of different lengths and may rely on incomplete representation of an underlying tract due to premature termination [48]. While tracts are identified in an unsupervised manner, identified tracts may not represent a true underlying pathway and would require verification from an expert with anatomical knowledge.

Reproducibility (the ability to identify the same tract using different methods) and reliability (the ability to identify the same tract using the same methods) are also open challenges facing tractography. In one tractography reproducibility challenge, which explored different diffusion models, tractography algorithms, and identification techniques, the authors found poor overlap of identified tracts in addition to the inability to identify all valid ground truth bundles [54]. Another tractography reproducibility challenge that specifically focused on assessing reproducibility of differing models, algorithms and parameters, identified algorithmic differences lead to disagreements between generated tracts [55]. In both challenges, tractography was assessed against well-known or generated ground-truth tracts. The reproducibility and reliability problem is further complicated when assessing "U"-shaped and deep subcortical WM tractography. Individual differences in cortical gyrification affect the spatial arrangements

of "U"-shaped WM, whose trajectories tend to follow the cortical folds. Previous studies have primarily looked at the "U"-shaped WM common to all of a study dataset [56], but have not explored the significance of bundles which may not be present in all study participants. Deep subcortical WM presents a different reproducibility challenge than short-ranged, "U"-shaped WM. Axonal trajectories connecting subcortical structures are in a densely packed area with multiple fibre orientations, complicating reconstruction of subcortical tracts [57]. As a result, identification of subcortical tracts has been limited and its reproducibility largely unassessed.

Validation of tractography reconstructed pathways (i.e. confirmation of presence and trajectory of a tract) is also a non-trivial task due to the lack of ground truth [58]. As noted in previous sections, some methods of validation include Klingler dissection on post-mortem tissue and NHP studies involving chemical tracers. Klingler dissections are a time-consuming and delicate process, peeling away the layers of tissue to identify axonal trajectories [16]. Invasive tracer studies face challenges that include the lack of a clear site of injection, complicating comparisons between different NHPs, and quantification of connections [59]. Validation of tractography algorithms have been attempted on phantoms by recreating complex geometries encountered using objects such as glass capillaries in order to assess diffusion models and tractography algorithms [60]. With the advancement of 3D printed technology, recent studies have also explored the possibility of validating dMRI properties using 3D printed phantoms with tissue mimicking properties [60]. Despite difficulties of validating trajectories, tractography is routinely used as it is currently the only means of non-invasively probing WM tissue *in vivo* [59].

1.4 Previous work on short-ranged connectivity

Historically, *in vivo* investigations have focused on long-range tracts to gain a better understanding of the connections between distant regions of the brain. While intracortical connections are still largely inaccessible *in vivo*, advances in hardware, software, and methodology have enabled studies to begin probing the short-range connections in recent years. The following subsections briefly describe some recent work involving the short-ranged, "U"-shaped WM and deep subcortical WM.

1.4.1 Short-ranged, "U"-shaped WM

In the past two decades, a number of studies have investigated the short-ranged, "U"-shaped WM using tractography. While the majority of these studies have explored the short-ranged,

"U"-shaped WM throughout the whole-brain, a few chose to focus solely on the "U"-fibres in specific regions (e.g. frontal lobe [61], somatomotor area [62], retinotopic area [63]). Irrespective of the investigated region, short-ranged, "U"-shaped WM studies can be broadly categorized into two groups: (1) identifying "U"-fibres and (2) assessing changes due to pathology. To date, a number of studies have been performed whose primary aim was to identify the short-ranged, "U"-shaped WM (Table 1.1), using different techniques (e.g. clustering, ROIs) in healthy individuals. Notably, there have also been 3 studies who performed comparisons with either post-mortem tissue [8, 62] or compared with another species [64]. These studies provided a methodological framework (e.g. determine shape of tract, limit tract length, apply clustering or ROIs for identification) to investigate the short-ranged, "U"-shaped WM, but lacked consensus (e.g. different bounds on tract length [56, 65, 66]) and standardization (e.g. different types of clustering is performed in different studies [64, 66]). With a number of different techniques available for future investigations, as well as its use in past studies, the reliabilities of the available techniques should be assessed.

Table 1.1: Studies identifying and assessing short-ranged, "U"-shaped WM in healthy human adults (unless otherwise stated) using the various techniques previously described. Majority of the studies performed whole-brain examination, with only a few noted studies focusing on specific regions.

Year	First Author	Dataset	Objective
2008	Oishi [4]	Healthy (n=81)	Map "U"-fibre of gyral blades
2011	Guevara [65]	Healthy (n=12) Children (n=2)	Create clustering tool for identification
2012	Guevara [66]	Healthy (n=12)	Automatic identification Create atlas of "U"-fibres
2012	Catani [8]	Healthy (n=12) Post-mortem(n=1)	Map frontal lobe "U"-fibres Assess lateralization
2013	Pardo [67]	Healthy (n=30)	Examine tract variability
2014	Zhang [64]	Healthy (n=30) Fetal (n=21) NHP (n=35)	Examine across species and modalities
2014	Vergani [62]	Healthy (n=10) Post-mortem (n=6)	Study connectivity around somatomotor area
2016	Rojkova [61]	Healthy (n=57)	Map frontal lobe Assess effects of age and education
2017	Guevara [56]	Healthy (n=79)	Highly reproducible automatic identification Create new atlas
2018	Oyefiade [68]	Healthy (n=104)	Study development of "U"-fibres
2019	Román [69]	Healthy (n=1)	Study effects of streamline count
2020	Movahedian Attar [63]	Healthy (n=17)	Investigate "U"-fibres in retinotopic areas
2021	Pron [70]	Healthy (n=100)	Examine tracts around central sulcus

In addition to the reliability of the applied techniques, the study of short-ranged, "U"-shaped WM itself could elucidate key findings associated with neuropsychiatric disorders and neuro-

logical conditions (Table 1.2). The investigation of "U"-fibres *in vivo* is still in its infancy when compared to studies of the brain's long-range tracts, with only a handful of studies having explored the association of short-ranged, "U"-shaped WM with neuropsychiatric disorders and neurological conditions. A number of these studies made use of previously created WM atlases or GM regions to identify the "U"-fibres to study epilepsy [12, 71], autism spectrum disorder (ASD) [11], Alzheimer's disease (AD) [72,73], mild cognitive impairment (MCI) [73] multiple sclerosis (MS) [74], Parkinson's disease (PD) [75], and psychosis [76]. These studies evaluated either the tract density [12] or investigated changes to diffusion metrics (e.g. FA, MD), relating metric changes to clinical observations (e.g. symptom severity) [11, 72, 74, 76]. With the ability to identify the short-ranged, "U"-shaped WM, additional insights can be gained to improve understanding of the functional role these groups of tracts may have and how they may change due to pathology.

Table 1.2: Tractography studies investigating short-ranged, "U"-shaped WM changes associated with pathology.

Year	First Author	Dataset	Findings
2016	Reginold [72]	Healhy (n=24) AD (n=16)	Increased diffusivity associated with AD
2017	O'Halloran [12]	Healthy (n=8) Epilepsy (n=8)	Decreased tract density in patients
2018	d'Albis [11]	Healthy (n=40) ASD (n=30)	Reduced connectivity with social cognitive deficits
2019	Ostrowski [71]	Healthy (n=14) Epilepsy (n=20)	Increased quantitative metrics in children with epilepsy Associated with seizure onset zone and sensorimotor deficits
2019	Ji [76]	Healthy (n=40) Schizophrenia (n=31) Bipolar disorder (n=32)	Reduced FA in affected regions Increased FA believed to be compensatory
2020	Bigham [73]	Healthy (n=24) AD (n=24) MCI (n=24)	Increased diffusivity in patients Diffusivity differences can differentiate AD and MCI
2022	Buyukturkoglu [74]	Healthy (n=31) MS (n=29)	Increased MD in early stages of MS Metrics correlated with symptom severity
2022	Zhang [75]	Healthy (n=29) PD (n=34)	Correlation with FA and cognitive performance Affected tracts in sensorimotor region

1.4.2 Deep subcortical WM

Studies using tractography to study the connectivity between subcortical structures have been more limited compared to those of the short-ranged, "U"-shaped WM, in part due to the complexity of the diffusion signal in the deep brain. Nonetheless, studies (Table 1.3) have endeavored to study these deep-rooted tracts in both *in vivo* [77–80] and *ex vivo* [17] samples, primarily leveraging the ROIs with tractography. These studies often examined specific subcortical tracts and in some instances the therapeutic effects of stimulating such tracts. In addition to studies of long-range and short-ranged, "U"-shaped tracts, identification of the deep subcortical tracts are also important for both individually examining tracts and for completing the

circuitry involved with function and cognition (e.g. motor circuit). Similar to the short-ranged, "U"-shaped WM, it is also critical to evaluate the reliability of techniques for identifying this group of tracts and investigate associated changes with pathology.

Table 1.3: Studies of subcortico-subcortical connectivity using tractography

Year	First Author	Dataset	Objective
2017	Rozanski [77]	Dystonia (n=10)	Role of pallidothalamic tract in deep brain stimulation
2020	Avecillas-Chasin [78]	Parkinson's Disease (n=55)	Assess pathways associated with symptom improvements from deep brain stimulation
2020	Bertino [79]	Healthy (n=100)	Characterize connectivity of globus pallidus
2020	Oishi [17]	Post-mortem (n=1)	Create MRI atlas Evaluate MRI identified trajectories
2021	Raghu [80]	Dystonia (n=19)	Assess predictive capability of putamen connectivity

1.5 Short-ranged WM in psychosis

As noted in the previous section, there have been few studies performed investigating the short-ranged connections of the human brain, particularly in clinical populations. One such clinical population is psychosis, which has long been hypothesized to arise from disrupted connectivity and consequently abnormal interactions between brain regions [81–83]. Large cohort studies have supported the neurodevelopmental theory associating progression of psychosis, and in particular schizophrenia, with early life events [84]. Furthermore, imaging studies of long-ranged WM tracts have implicated WM changes throughout the brain in patients with schizophrenia [85,86]. Due to the late maturation of short-ranged "U"-shaped WM, these tracts may be vulnerable to developmental abnormalities [10] associated with psychosis. Moreover, the deep subcortical WM have an important role in function and cognition [15] and are also likely to be affected in psychosis. Given the link between short-ranged connections, maturation, importance to neurocircuitry and psychosis, subsequent investigations may look into such connections for biomarker discovery and disease stratification in psychosis.

1.6 Thesis outline

Despite the growth of dMRI and tractography, both in its use and development of tools to study the brain's structural connectivity, there is an absence of consensus stemming from various sources (e.g. lack of anatomical definition, group preferences) [87]. This is often seen by the differences in the steps taken and choices made during processing and analysis in different studies. While complete agreement may be difficult to reach, efforts should be made to evaluate developed tools or techniques in order to establish confidence in its application for future studies. This is particularly important as new frameworks are developed to study the short-ranged, "U"-shaped and deep subcortical WM, two groups of tracts that have largely been disregarded in studies of structural connectivity until recently.

Broadly, the objective of this thesis was to apply dMRI and tractography to study the short-ranged, "U"-shaped and subcortico-subcortical WM associated with pathology. To that end, this thesis first aimed to assess the reliability of techniques to be applied for studying each group of tracts in patient populations. Not only does this provide a level of confidence in the application of the technique, it also establishes a framework to evaluate newly developed techniques. Following assessment of reliability, short-range connectivity was examined in a patient population with psychosis. We hypothesized that a difference would be seen in the scalar measurements in patients relative to healthy individuals and that such a change would be associated with clinical symptoms experienced.

Chapter 2 aimed to quantify the reliability of template-based clustering applied to both whole-brain tractography and to only the short-ranged, "U"-shaped WM. Specially, we sought to evaluate the reliability of spectral clustering and QuickBundles [53], two techniques that have been used previously to identify tracts from whole-brain tractography. Here, we leveraged two publicly available, high quality datasets of (1) different individuals and (2) the same individual scanned over multiple sessions. This assessment of template-based clustering highlighted its validity for identifying short-ranged, "U"-shaped WM, while also identifying the shortcomings of reliability measures.

Chapter 3 investigated the ability to identify the deep subcortical WM, a challenging task due to the complexity of the compact region. To that end, tractography and ROIs were used to aid identification of connections. As was performed in Chapter 2, a reliability assessment was also performed here, again leveraging a publicly available, high quality dataset of individuals

scanned at two different time points. Furthermore, an additional validation of findings was performed on a separate dataset of individuals acquired at a single time point. In addition to evaluating the reliability of the technique, we also visually inspected identified connections making comparisons with those previously described in tract-tracing literature from NHPs. This work demonstrated the capability of tractography to recapitulate known connections in the complex region of the deep brain.

Chapter 4 uses the techniques evaluated in Chapter 2 to identify and investigate the short-ranged, "U"-shaped WM in a patient cohort diagnosed with first episode schizophrenia (FES). This chapter aimed to identify changes of the short-ranged, "U"-shaped WM related to FES, specifically investigating changes to "U"-shaped tracts of the frontal lobe, a region where past studies have identified abnormalities in patients with psychosis. Here, DTI was performed along with tractography, noting differences in scalar metrics from patients with FES and correlating findings with clinical symptoms. We detected a number of tracts exhibiting abnormal scalar measurements in patients with FES, which suggests potential malformation of the myelin.

In Chapter 5 of this thesis, the findings and implications of the previous three chapters are discussed and summarized. These discussions lead to suggestions for future directions.

Chapter 2

Assessing the reliability of template-based clustering for tractography in healthy human adults

This chapter is based on the following manuscript:

- Kai, J. & Khan, A.R. (2022). Assessing the reliability of template-based clustering for tractography in healthy human adults. Frontiers in Neuroinformatics. 16. 777853. https://doi.org/10.3389/fninf.2022.777853

2.1 Introduction

The brain consists of numerous regions connected together by axonal bundles which form the structural pathways (also referred to as tracts) [41, 47] of a highly connected network that enables function and cognition [59, 88–90]. Although the gold standard for investigating structural connectivity are chemical tracers, these techniques are invasive and performed only in animal studies and post-mortem samples [41, 59]. Alternatively, the brain's connectivity can be studied non-invasively, *in vivo* with diffusion magnetic resonance imaging (dMRI). Briefly, dMRI acquires directionally-sensitive information about the diffusion of water molecules [91], which preferentially diffuses in parallel to the axonal trajectory [92]. Using information from dMRI, an estimation of the pathway trajectories can be reconstructed as a streamline with tractography by (1) estimating the diffusion orientation within all image voxels and (2) following along an orientation voxel-to-voxel until a termination criterion is met [41]. Past studies have examined how long-range tracts connecting distant brain regions [93–97] and short-range, "U"-shaped tracts comprising the superficial white matter [48,56,66,98] are affected in neurological or psychiatric disorders. Furthermore, quantitative differences identified in the structural pathways of patient groups have been correlated with clinical symptoms [95]. An understanding of how tracts are affected in patient cohorts could provide key insights for diagnosis and improve treatment.

To identify different tracts from tractography, either manual or automated techniques can be employed. Manual techniques require users to place inclusion and exclusion regions of interest (ROI) to extract tracts for further investigation, a laborious and time-consuming task requiring anatomical knowledge with results that can vary between different users or sessions [48]. An alternative to manual ROIs is to leverage atlas-based ROIs, which require an adequate registration with an individual's data [48,56,66,98] to automate identification of ROIs to extract tracts. However, this still requires anatomical knowledge to select the ROIs needed to isolate each tract of interest. One automated alternative that does not require ROIs is TRACULA, which instead uses information of surrounding anatomical structures to identify tracts [98]. While the described approaches can aid in tract identification with a high degree of anatomical accuracy, they rely on and are limited by *a priori* knowledge [55]. Other automated techniques attempt to

identify tracts with a data-driven approach, employing unsupervised clustering algorithms that commonly rely on the similarity of streamline trajectories [48]. These clustering approaches, which are not dependent on a priori knowledge, may identify previously unnamed or unidentified tracts and have been shown to produce known pathways with high confidence [48, 99]. To identify the same tracts across individuals, a labelled template is first created from clustering together streamlines by similarity. Clusters are arbitrarily labelled for identification with no anatomical reference. The template is then registered to different individuals to identify similar tracts in a template-based clustering approach. While automated clustering techniques may include incomplete or false positive streamlines [48], user biases from manual intervention are avoided [99]. A number of studies have taken a template-based clustering approach to identify tracts of interest, including Tunç *et al.* [48], Guevara *et al.* [66], Guevara *et al.* [56], O'Donnell and Westin [52], Garyfallidis *et al.* [100], Zhang *et al.* [101], and Román *et al.* [102] to name a few. Although both template-based and atlas-based approaches have been used to identify tracts, the primary difference between the two approaches is the use of predefined ROIs from anatomical atlases and a priori anatomical knowledge for atlas-based approaches to identify and name tracts, while template-based approaches uses the similarity of tract features to identify corresponding tracts.

Reliability of template-based clustering approaches, that is, the ability to extract corresponding tracts successfully when applying the same methodology to multiple scans of the same subject or multiple subjects, is critically important and increases confidence applying the same approach to study tracts of interest. In the previously mentioned studies, Tunç *et al.* [48] used a template created from the same individuals studied, while O'Donnell and Westin [52] and Garyfallidis *et al.* [100] highlighted clustering techniques to identify tracts. Zhang *et al.* [103] used the same atlas previously developed by their group to compare the performance of template-based clustering against an ROI-based technique using 3 different test-retest datasets across varying age groups, highlighting the benefits of a template-based approach. Guevara *et al.* [66] proposed a template-based clustering method to extract "U"-shaped tracts and created a superficial white matter atlas. Later, Guevara *et al.* expanded the technique to examine "U"-shaped tract reliability and produce a new superficial white matter atlas containing tracts present in at least 30% of the subjects within the dataset, producing the most common "U"-shaped tracts across those individuals [56]. Despite the use of these techniques in studies of structural connectivity, in-depth comparisons have yet to be performed to evaluate the parallels between different template-based approaches. Further, the effect of individual differences on reliably identifying tracts has not yet been examined. Lastly, an investigation of the use of template-based approaches to reliably identify and examine superficial white matter, where

individual differences can be found due to varying cortical folding, has yet to be extensively studied.

In this work, we evaluate the reliability of template-based clustering of whole-brain tractography applied to both different subjects and within a single subject using two clustering approaches - spectral clustering and QuickBundles. Both clustering approaches are applied to two open source datasets of healthy individuals: (1) Human Connectome Project, and (2) MyConnectome Project, examining all identified tracts. While the goal of tract identification is to enable investigations of tracts and study changes in patient populations, reliable identification is a non-trivial task, even amongst healthy individuals. Pathology can complicate the ability to quantify reliability by introducing heterogenous changes to the structural connectivity in different individuals. First, we assess the reliability of template-based clustering of whole-brain tractography. We follow-up by separately assessing the reliability of clustering short-range, "U"-shaped pathways, where greater intersubject variability is expected than in long-range tracts due to differing cortical folding patterns, different clustering parameters and the use of constraints are required.

2.2 Materials and methods

All processing and analysis was performed within containerized environments on high performance compute clusters hosted by Compute Canada. Environments contained installations of Nipype [104], for creating reproducible pipelines, and MRtrix3 [105] for tractography processing[1] and implementation of spectral clustering[2]. Additionally, QuickBundles [53] clustering, as implemented within the DIPY library [106], was also used as a secondary clustering technique. An overview of the general workflow applied is shown in Figure 2.1. Briefly, a labelled population template was created from minimally preprocessed data and template-based clustering was applied to two separate datasets. Subsequent analysis was performed on the identified tracts, assessing the metrics across identified tracts within each dataset.

2.2.1 Data acquisition and pre-processing

2.2.1.1 Template dataset

Minimally pre-processed dMRI data, as described in Glasser et al. [107], from the HCP1200 release of the Human Connectome Project (HCP) [108] of 100 unrelated subjects (46 male, 54

[1] www.github.com/khanlab/mrtpipelines
[2] www.github.com/khanlab/neurobeer

female; aged 22-35), here-on defined as HCPUR100, was used to first create a clustered tractography template. Structural T1w data of these subjects were also used to create an anatomical

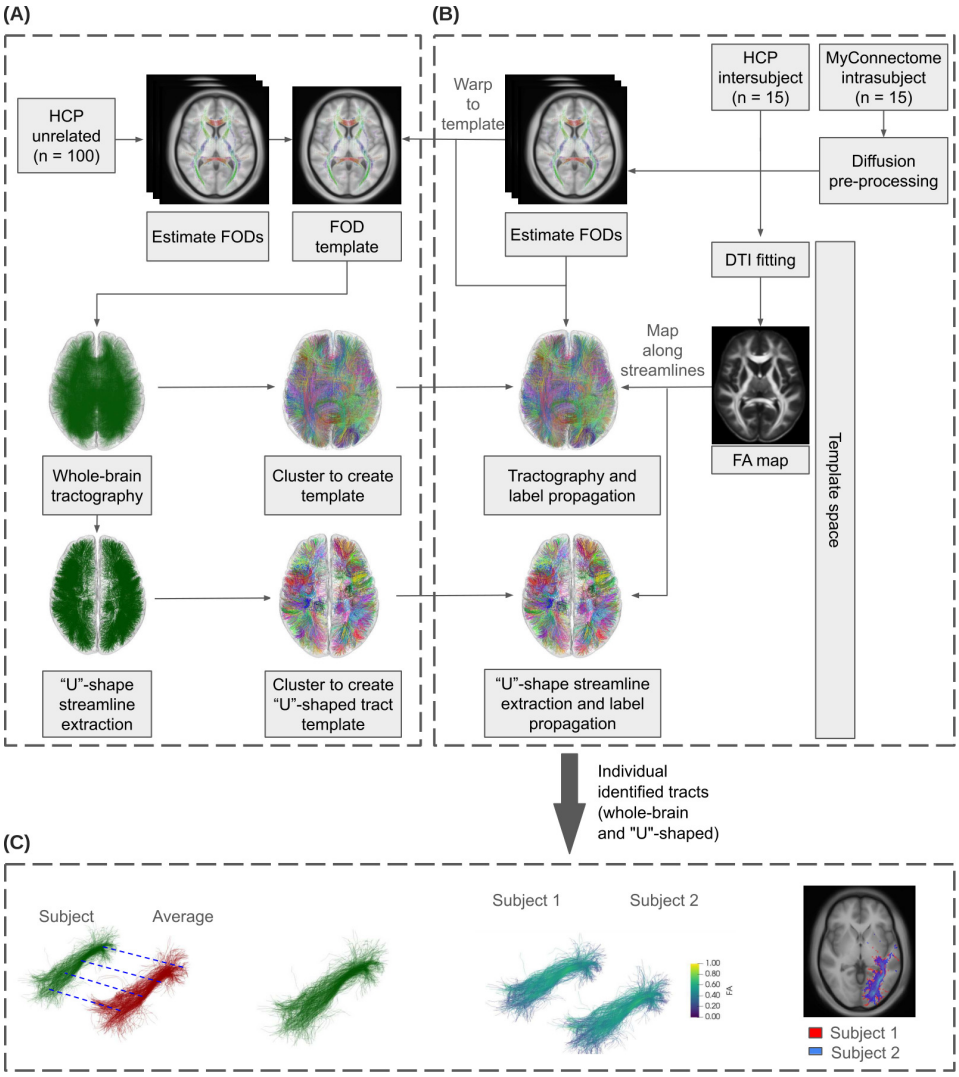

Figure 2.1: General diffusion processing workflow using minimally preprocessed HCP and unprocessed MyConnectome data. (A) HCP unrelated subjects were used to create the population-based FOD template. Whole-brain and "U"-shaped tractography was created from the FOD template and streamlines were assigned labels via clustering, creating labelled tractography templates. A subset of each identified tract is extracted and used to propagate labels to the analysis datasets. (B) MyConnectome data was first preprocessed using in-house pipelines. Together with the minimally preprocessed HCP dataset, individual FODs were computed and warped to the previously created template. Tractography was performed for each subject / session in the template space. Additionally, DTI fitting was performed and mapped along the generated streamlines. Labels from the tractography template were propagated to subject / session's tractography. (C) Analysis was performed on the identified tracts, evaluating Euclidean distances and tract overlaps both within each dataset and against the labelled template. In addition, streamline counts and along-tract agreement of FA were assessed within each dataset.

template for cortical parcellation and for lobular assignment via FreeSurfer [109]. dMRI

data was acquired on a customized Siemens Skyra 3T scanner [110, 111] with the following scanning parameters: repetition time/echo time (TR/TE) = 5520 / 89.50 ms; resolution = $1.25 \times 1.25 \times 1.25$ mm^3; b-values = 1000, 2000, 3000 s/mm^2 (90 directions each) with 18 b-value = 0 s/mm^2 images. Full acquisition details can be found in the HCP1200 subject reference manual[3].

2.2.1.2 Analysis datasets

Two separate datasets from HCP and the MyConnectome Project [112] were used to assess reliability of template-based clustering, here-on referred to as the analysis datasets. From the HCP analysis dataset, an additional 15 subjects (8 male, 7 female; aged 22-35) were randomly selected from the HCP1200 release for analysis, matching the number of available sessions available in the MyConnectome analysis dataset. Acquisition parameters were previously described in the template dataset subsection.

From the MyConnectome Project, a single male subject (aged 45 at onset of data acquisition), scanned on multiple occurrences acquired over a 3 year period as a part of the MyConnectome Project was used for analysis. Data acquisition was performed on a separate Siemens Skyra 3T scanner. Out of 94 production sessions, 15 had dMRI acquisitions available for assessment, excluding a follow-up session acquired on a separate imaging system. Scanning parameters are as follows: repetition time/echo time (TR/TE) = 5000 / 108 ms; resolution = $1.74 \times 1.74 \times 1.7$ mm^3; b-values = 1000, 2000 s/mm^2 (30 directions each) with 4 b-value = 0 s/mm^2 images. Detailed information on data collection can be found in the study protocol[4]. Using an in-house developed pipeline, prepdwi [113], dMRI acquisitions were pre-processed. Briefly, principal component analysis based denoising [114, 115] was performed followed by unringing of the dMRI data to minimize the effects of Gibbs ringing [116]. Afterwards, FSL's topup [117, 118] and eddy ([119] were applied to correct for distortions induced by susceptibility, eddy currents, and subject motion.

2.2.2 Tractography processing

The following sections describe the processing steps performed for generated tractography, including clustering and assignment of labels to streamlines.

[3] https://humanconnectome.org/study/hcp-young-adult/document/1200-subjects-data-release
[4] http://myconnectome.org/wp/53-2

2.2.2.1 Fiber orientation distribution

A fiber orientation distribution (FOD) template was created with the HCPUR100 using the MRtrix3 software suite [105]. Briefly, a tissue-specific (white matter, gray matter, and cerebrospinal fluid) response function was estimated for each HCPUR100 subject using the Dhollander algorithm [120], before averaging the computed response functions. Utilizing the average response function, FODs were estimated for each HCPUR100 subject using a multi-shell, multi-tissue constrained spherical deconvolution (MSMT-CSD) algorithm [121] and normalised with a multi-tissue informed log-domain intensity normalization (Raffelt et al., 2017). Normalised FODs were transformed using a multi-resolution pyramid structure to create an FOD template [122]. Registrations were optimized with 6 iterations of rigid and affine transformations each, and 15 iterations of non-linear transformation. The FOD template was utilized to transform analysis data to a common midway space (defined as the template space).

Similar steps were taken to compute FODs for data from the MyConnectome Project and HCP datasets. For each session / subject, a response function was estimated with the Dhollander algorithm, however as acquisition protocols differed between the two datasets, no average response function was derived. FODs were again estimated with MSMT-CSD, using the individual response functions and followed by FOD normalisation. Normalised FODs were transformed and reoriented to the template space.

2.2.2.2 Streamline tracking and qualification

Whole-brain probabilistic tractography was performed for the template and analysis datasets with MRtrix3, using the iFOD2 probabilistic algorithm [123] with default parameters. Random seeding of tractography was performed throughout the brain until targets of $100,000$ and $10,000,000$ streamlines have been selected for the template and analysis datasets respectively. Tractography was then filtered to fit the amplitudes of the associated FODs using spherical-deconvolution informed filtering of tractograms (SIFT) [124] until streamline counts of $50,000$ and $1,000,000$ remained for template and analysis datasets respectively. The combination of constrained spherical deconvolution (CSD), iFOD2 generated tractography, and SIFTing has previously been shown to improve tracking of streamlines, particularly in regions of multiple fiber orientations, while preserving tract densities reflective of the underlying diffusion signal.

Tensor images were additionally computed on intensity normalised diffusion weighted images (DWI) of the analysis datasets, which had also been transformed to template space. Diffusion tensor images (DTI) were estimated using an iteratively reweighted linear least squares esti-

mation [125]. Fractional anisotropy (FA) measurements were derived from DTI and mapped to corresponding streamlines, enabling further quantitative analysis following clustering.

2.2.2.3 Spectral Clustering (Method 1)

Using spectral clustering [126], bundles of streamlines (tracts) were initially identified on the SIFTed tractography template before propagating cluster labels to tractography from analysis datasets based on similarity of streamline trajectory. First, individual streamline similarity was assessed with comparisons to all other streamlines of the template. 20 equispaced samples, inclusive of endpoints, were taken along the length of each streamline and a minimum average, direct-flip (MDF) distance was used to compute between corresponding samples across streamlines [53, 66, 127, 128] and generate a distance matrix. Streamlines whose distances were greater than two standard deviations from the average whole-brain streamline distance were deemed to be outliers and discarded, similar to O'Donnell *et al*. [129]. An affinity matrix, characterizing similarity between streamlines, was created with the application of a Gaussian kernel with a width of 8 *mm* to the distance matrix.

Spectral clustering, which has been previously employed in tractography clustering [52, 101, 130], utilizes Laplacian matrices as one of the primary tools [126]. Following the implementation described by Ng *et al.* [131], spectral clustering was performed on the template tractography to label and assign streamlines to a cluster. A selection of k = 800 clusters was chosen following qualitative assessment of clusters ranging from k = 400 to k = 1400. The qualitative assessment involved visual inspection of identified tracts for each chosen number of clusters and was performed to assess the ability to discern tracts with noticeably different trajectories. This selection of 800 clusters was also determined to be the optimal number of clusters by O'Donnell and Westin [52], and later employed by Zhang *et al.* [101]. Established clusters were coloured according to the coordinates of the cluster centroids, as described by Brun *et al.* [132].

2.2.2.4 QuickBundles (Method 2)

For comparison, the template tractography was also clustered utilizing QuickBundles [53] before sub-sampling and propagating labels to tractography of analysis datasets as before to establish tract correspondence. Briefly, QuickBundles computes the MDF distance between unassigned streamlines with a centroid streamline from existing clusters, updating the cluster centroid as new streamlines are added. The computed distance is compared against a user-chosen distance threshold and if the distance is within the threshold, it is assigned to the cluster

with the smallest distance, otherwise it is assigned as a new cluster. Per Garyfallidis *et al.*, utilizing lower thresholds result in more detailed representations of underlying trajectories, while higher thresholds result in the merging of bundles which may have similar trajectories [53]. Additionally, the user can choose to set the maximum number of clusters, such that once the maximum number of clusters is reached, new streamlines are only assigned to existing clusters.

As was done for spectral clustering, streamlines were resampled to 20 equispaced samples in order to compute the MDF distance for QuickBundles, selecting a maximum of k = 800 clusters and a distance threshold of 8 *mm* was chosen to match the number of clusters and kernel width respectively from spectral clustering. Following cluster assignment, streamlines were coloured using the cluster centroid as was done for spectral clustering.

2.2.2.5 Labelling analysis datasets

Both spectrally clustered and QuickBundles clustered methods used a labelled sub-sample containing $20,000$ streamlines of the template tractography to assign labels to streamlines identified in the analysis datasets. A sub-sample of the labelled template was required due to computational memory limitations. Streamline similarity between the sub-sampled tractography template and the tractography from analysis datasets was also computed using the MDF method as previously described. Labels from template streamlines were propagated to the tractography from analysis datasets based on maximum similarity, establishing correspondence between the most similar tracts.

2.2.2.6 Short range, "U"-shaped streamlines

Streamlines comprising short-range, "U"-shaped tracts were identified and extracted from whole-brain tractography using adapted parameters [12, 56] to extract from whole-brain tractography. Identification of "U"-shaped streamlines utilized the Euclidean distance between streamline endpoints (D), computed as the Euclidean distance between the terminal ends of a streamline, and streamline length (L), computed as the arc length of the sample points (s_i).

$$L = \sum_{i=1}^{N} |S_i - S_{i-1}| \tag{2.1}$$

$$D = |S_N - S_1| \tag{2.2}$$

To extract streamlines with the expected "U"-shaped curvature, the end point distance was constrained to approximately one-third of the streamline length ($D < L/\pi$), as employed by

O'Halloran *et al.* [12]. Additional streamline length constraints of 20 *mm* (minimum) and 80 *mm* (maximum) were imposed (20 $mm \leq L \leq 80$ *mm*). Streamlines which crossed across brain hemispheres were removed.

2.2.3 Analysis

In the following subsection, we describe the metrics used to assess reliability of template-based tractography clustering. Briefly, we computed the centroid distances between the average dataset centroid and individual subject or session centroid within the respective datasets, compared the voxel-wise spatial overlap of identified tracts, and examined the streamline counts of identified tracts. Analysis was performed on corresponding tracts within each dataset. An unpaired t-test was also performed to determine whether there was a difference in the resulting metrics from the two cluster algorithms.

2.2.3.1 Distance from average centroid

Tract centroids were computed for all tracts identified in both analysis datasets by averaging spatial components of corresponding sample points across streamlines. A dataset average tract centroid (here-on referred to as the average centroid) was also computed by averaging the centroids computed across the subjects and sessions within the respective analysis datasets. An Euclidean distance was computed for corresponding tracts between the average centroid and centroids from the analysis datasets by employing the MDF distance previously described.

2.2.3.2 Voxel-wise spatial overlap of tracts

First, a tract density map for each cluster was created by identifying streamline counts passing through each voxel. Then, the fraction of each tract (a value between 0 and 1) passing through a voxel was determined from the tract density map to assess the weighted Dice similarity coefficient (wDSC) [133]. Briefly, the wDSC is a modified version of the conventional Dice similarity coefficient [134] for assessing overlap of tractography, weighting more heavily the denser regions of a tract instead of penalizing streamlines further from the core as is done by conventional Dice [133]. The wDSC was computed with the following equation (eq. 2.3), where A_v and B_v represent the fraction of streamlines passing through a voxel of two corresponding tracts and v' represents a voxel within the intersection of A and B.

$$wDSC(A, B) = \frac{\sum_{v'} A_{v'} + \sum_{v'} B_{v'}}{\sum_v A_v + \sum vB_v} \tag{2.3}$$

Average wDSC within the analysis datasets were computed across corresponding tracts.

2.2.3.3 Along-tract fractional anisotropy similarity

To assess reliability of quantitative scalar metrics along identified tracts, intraclass correlation (ICC) of along-tract fractional anisotropy (FA) was computed. Here, FA was chosen due to its widespread use and interpretation in a number of diffusion studies. Cousineau, Descoteaux, and Takemura previously highlighted the benefits of examining quantitative metrics along the length of a tract for examining reliability [135]. A two-way, random effects model [136] was employed to evaluate absolute agreement of FA at corresponding samples along the length of a tract. Utilizing this model, the column factor ("raters") were the samples along the tract, and the row factor ("targets") were the individual subjects or sessions of the analysis dataset.

2.2.3.4 Streamline count and variation

Streamline counts comprising each tract were extracted and compared across corresponding tracts and the subjects and sessions within the respective analysis datasets. Streamline counts enabled assessment of reconstruction consistency and importantly, may be used to determine tracts which may not be reliably identified. The extent of streamline count variability of each identified tract was also evaluated by computing the coefficient of variation (CV). Here, the CV was calculated as the standard deviation of the streamline count (σ) over the average streamline count (μ) for corresponding tracts within each analysis dataset ($CV = \sigma/\mu \times 100\%$).

2.2.3.5 Relationship between metrics

To determine whether a relationship existed between the different reliability metrics examined, a Spearman correlation is computed between the described metrics used for reliability analysis. After computing the Spearman correlation between all metrics, false discovery rate correction was performed following the Benjamini-Hochberg procedure [137].

2.3 Results

2.3.1 Distance from average centroid

The mean Euclidean distances were observed to be 2.16 ± 1.10 *mm* and 2.51 ± 0.90 *mm* for the MyConnectome and HCP datasets respectively when compared against the average centroid identified from the spectrally clustered template. From the QuickBundle clustered template, an average Euclidean distance of 1.96 ± 0.73 *mm* and 2.31 ± 0.62 *mm* was observed for the MyConnectome and HCP datasets when compared against the average centroid. Across datasets, the average Euclidean distances of tracts to the corresponding average centroid was around

2 voxels (about 2.5 *mm*). In both datasets, a difference was observed in the computed Euclidean distance for tracts identified using the two clustering algorithms. Figure 2.2A displays a boxplot with individual points indicating the observed Euclidean distances for a given tract for each dataset. Distributions of Euclidean distances were similar across datasets, with the MyConnectome dataset exhibiting a lower Euclidean distance against the average centroid for both clustering methods than the HCP dataset. Supplementary table A.1 details the average Euclidean distances and standard deviations for all tracts identified.

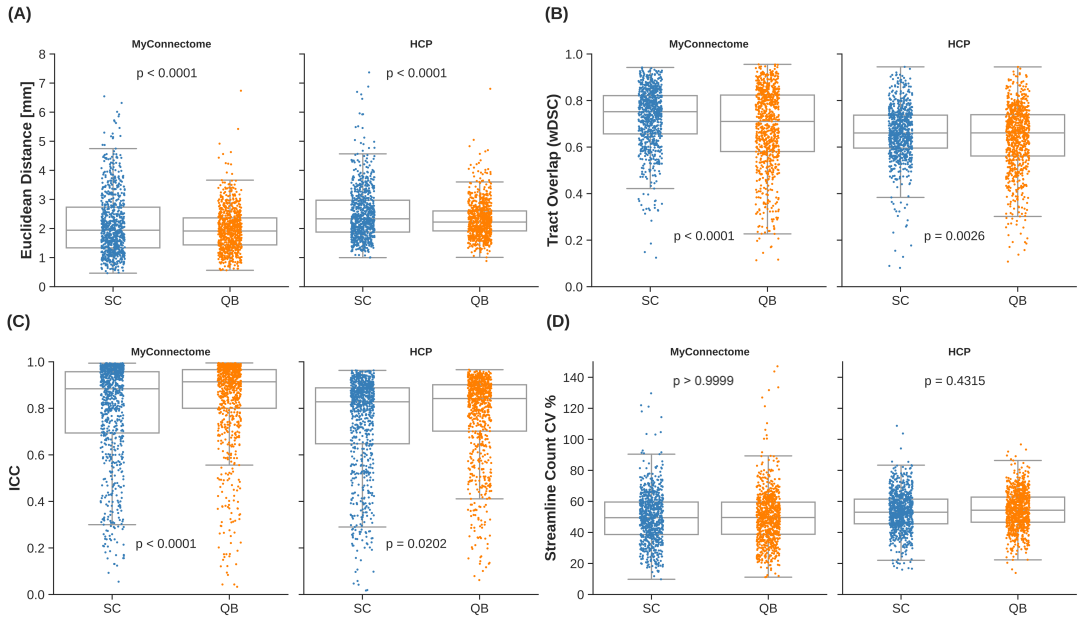

Figure 2.2: Individual observations for a given metric are overlaid on a box plot for each dataset and clustering method employed by the template. (A) Mean Euclidean distance of tracts relative to the corresponding average tract centroid. (B) Average voxel-wise spatial overlap across corresponding tracts. (C) Along-tract absolute agreement of fractional anisotropy across corresponding tracts. (D) Variability of streamline counts across corresponding tracts.

2.3.2 Weighted voxel-wise spatial overlap

Spatial overlap of identified tracts were computed between corresponding tracts identified with both spectrally clustered and QuickBundles clustering algorithms within the analysis datasets. Overlap within analysis datasets demonstrated good overlap in both datasets with wDSC of 0.729 ± 0.129 and 0.661 ± 0.115 for spectral clustering identified tracts in MyConnectome and HCP analysis datasets respectively. As with the computed overlaps computed in tracts identified via spectral clustering, QuickBundle clustered identified tracts also demonstrated good overlap in both datasets with an average wDSC of 0.683 ± 0.174 and 0.639 ± 0.141 for MyConnectome and HCP analysis datasets respectively. A difference in resulting tract-

overlaps observed for both datasets when using the two different clustering algorithms. Figure 2.2B displays for each dataset, a box plot with individual points indicating the observed average overlap for a given tract. Full details of computed wDSCs for identified tracts within analysis datasets are provided in supplementary table A.1.

2.3.3 Along-tract fractional anisotropy agreement

Intraclass correlation (ICC) was computed for each analysis dataset by comparing the along-tract FA at corresponding samples across subjects and sessions. For tracts identified from the spectral clustered template, good absolute agreement was observed with computed average ICCs of 0.792 ± 0.218 and 0.742 ± 0.207 for the MyConnectome and HCP analysis datasets respectively. The QuickBundle clustered template also demonstrated high agreement of along-tract FA, with average ICCs of 0.841 ± 0.190 and 0.769 ± 0.190 in the MyConnectome and HCP datasets respectively. For both datasets, ICCs demonstrated a difference when using the two different clustering algorithms. However, with both clustering algorithms, the MyConnectome dataset demonstrated better along-tract agreement. Figure 2.2C displays for each dataset, a box plot with individual points indicating the observed along-tract FA agreement for a given tract. Supplementary table A.1 provides full details of computed ICC for all tracts, including 95% confidence intervals.

2.3.4 Streamline count and variation

Within the analysis datasets, streamline counts were determined for each subject or session and averaged across corresponding tracts. Tracts lacking streamlines for at least one subject or session of the analysis datasets were identified. 13 of 800 (spectral clustering) and 5 of 800 (QuickBundles) tracts of the MyConnectome dataset contained no streamlines across the available sessions, while all tracts of the HCP dataset contained at least a single streamline for the analysed subjects. No difference in streamline count variability was observed between the two algorithms for either dataset. Figure 2.2D displays for each dataset, a box plot with individual points indicating the observed streamline count variance of a given tract. Full details regarding streamline counts for each tract and associated dataset information can be found in Supplementary table A.1.

Furthermore, the extent of the variability for each of the identified tracts were examined. The tracts identified via spectral clustering in the MyConnectome dataset exhibited lower average variability (50%) compared against the HCP dataset (53%). However, the range of the variability exhibited was smaller in the HCP dataset (16 – 109%) than in the MyConnectome dataset

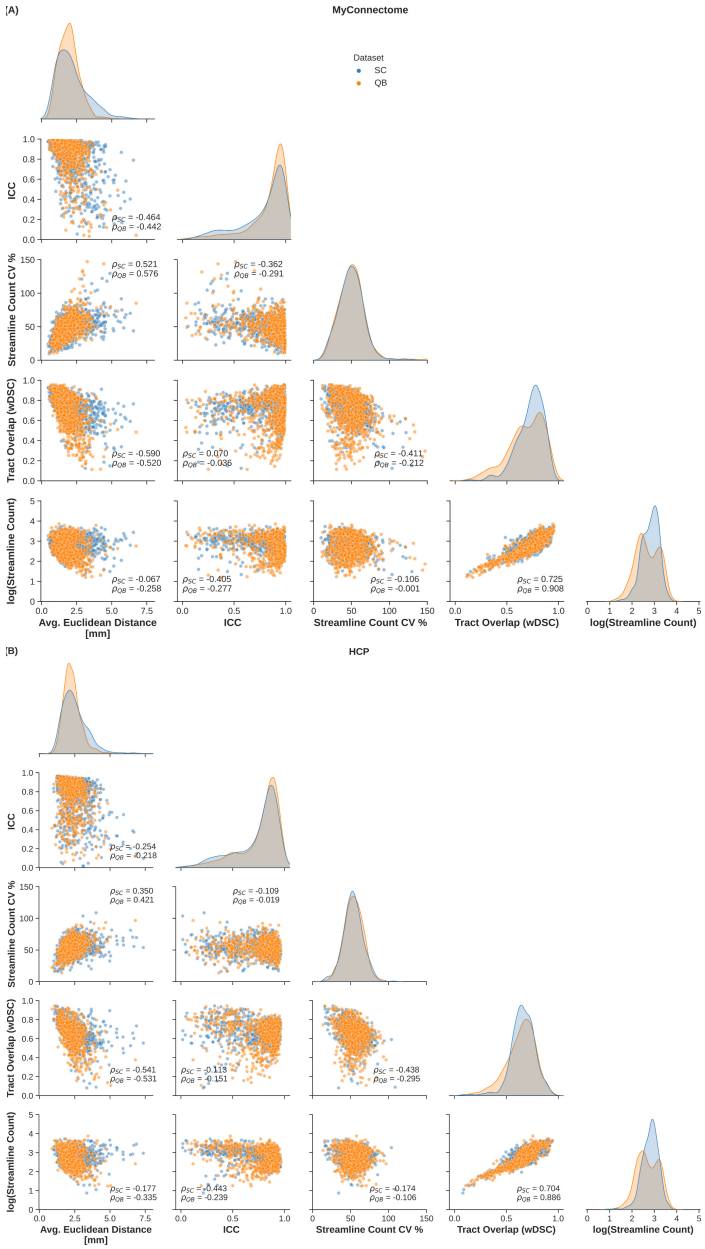

Figure 2.3: Spearman correlations are computed to explore relationships of metrics employed to assess reliability of spectral clustered (blue circles) and QuickBundle clustered (orange circles) identified tracts via whole-brain tractography. Relationships between different metrics used for assessment are shown in pairplots for (A) MyConnectome and (B) HCP datasets. Relationships between various metrics and average Euclidean distance from an average tract centroid (left-most), relationships with along-tract absolute agreement (ICC; middle-left column), relationships with streamline count variability (middle-column), and with voxel-wise spatial overlap (middle-right column) are displayed. Distribution of observed points for a given metric (matching the x-axis) are plotted along the diagonal.

(10 – 203%). Similarly, tracts identified via QuickBundles demonstrated lower variability (50%) in MyConnectome than in HCP (54%), but again showed a smaller range of variability in HCP (14 – 97%) than in MyConnectome (11 – 156%). A full summary of average streamline counts and CV can be found in Supplementary table A.1.

2.3.5 Relationships between reliability metrics

Relationships between employed metrics were explored to examine common features in reliable tracts. First, a significant negative correlation was observed between the average Euclidean distance from the average centroid and tract overlap, streamline count variability, while a significant positive relationship was observed between Euclidean distance and streamline count variability (Figure 2.3, left column). Further, a significant negative correlation was identified between the along-tract agreement of fractional anisotropy and both streamline count variability (only for the MyConnectome dataset) and the average log-transformed streamline count (Figure 2.3, middle-left column). Finally a significant negative relationship was observed between the tract spatial overlap and streamline count variability (Figure 2.3, middle column), while a positive relationship was observed between tract overlap and the average log-transformed streamline count (Figure 2.3, middle-right column). No significant relationship was identified between the tract spatial overlap and the along-tract agreement or between the log-transformed streamline count and average Euclidean distance. Additionally, no significant relationship was identified between streamline count variability and tract overlap in the HCP dataset. Relationships were similar for both tracts identified via spectral clustering and the QuickBundles algorithm. For the majority of identified relationships, the correlation was stronger in the single-subject MyConnectome dataset than in HCP datasets for both algorithms.

2.3.6 "U"-shaped tract reliability

Assessment of short-range, "U"-shaped tracts was performed with the same metrics used to examine reliability of whole-brain tractography. The average Euclidean distance from the average centroid for identified "U"-shaped tracts via the spectrally clustered template was similar as previously observed, with distances of 2.53 ± 0.75 *mm* and 2.99 ± 0.67 *mm* in MyConnectome and HCP datasets respectively. From the QuickBundle clustered template, a slightly greater distance is observed - 2.66 ± 0.92 *mm* and 3.05 ± 0.82 *mm* for MyConnectome and HCP datasets respectively. Figure 2.4A and 2.4B display the identified tracts from spectral clustering and QuickBundles respectively (see supplementary video A.6 and A.7 for individually identified tracts for the respective algorithms), while Figure 2.4C displays a box plot with individual Euclidean distance observations against the average tract centroid for each dataset.

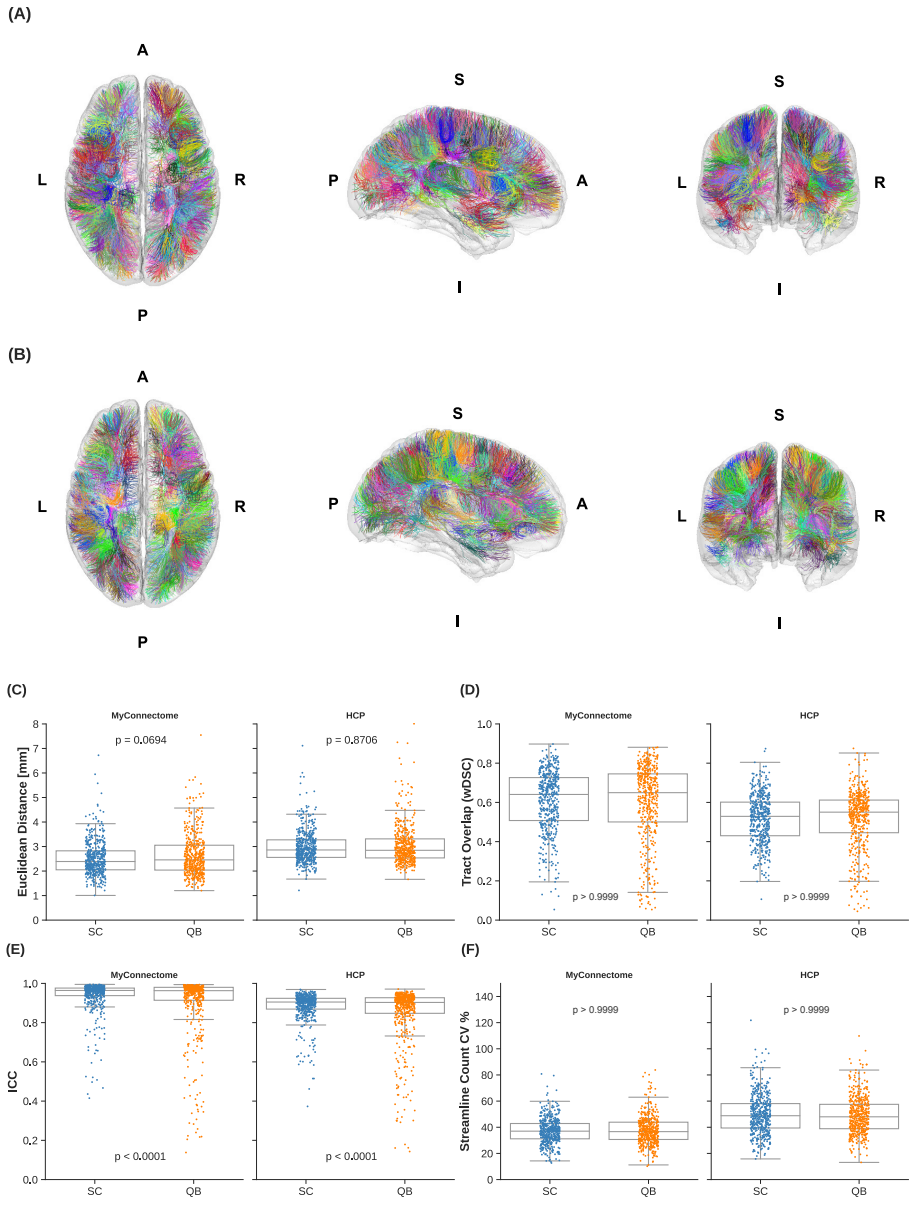

Figure 2.4: "U"-shaped tracts identified in the HCPUR100 template viewed from axial superior (left), sagittal right (middle), and coronal anterior (right) via (A) spectral clustering and (B) QuickBundle clustering. Colours of identified tracts do not correspond across clustering methods. Individual observations in "U"-shaped tracts for a given metric are overlaid on a box plot for each dataset and clustering method employed by the template. (C) Mean Euclidean distance of tracts relative to the corresponding average tract centroid. (D) Average voxel-wise spatial overlap across corresponding tracts. (E) Along-tract absolute agreement of fractional anisotropy across corresponding tracts. (F) Variability of streamline counts across corresponding tracts.

Spatial overlap of identified "U"-shaped tracts from spectral clustering and QuickBundles were also computed. Overlap within analysis datasets demonstrated moderate overlap in both datasets with wDSC of 0.606 ± 0.155 and 0.517 ± 0.123 for spectral clustering identified

tracts in MyConnectome and HCP analysis datasets respectively. With QuickBundle clustered identified tracts, similar overlaps were observed with an average wDSC of 0.598 ± 0.199 and 0.515 ± 0.152 for MyConnectome and HCP analysis datasets respectively. Full details of computed wDSCs for identified "U"-shaped tracts compared for the analysis datasets are provided in Supplementary table A.2.

As with whole-brain tractography reliability, the absolute agreement of along-tract FA was also computed for "U"-shaped tracts identified in the analysis datasets, comparing the metrics mapped at corresponding samples across subjects and sessions. For tracts identified from the spectral clustered template, good absolute agreement was observed with computed average ICCs of 0.938 ± 0.081 and 0.883 ± 0.076 for the MyConnectome and HCP analysis datasets respectively. The QuickBundle clustered template also demonstrated high agreement of along-tract FA, with average ICCs of 0.900 ± 0.162 and 0.847 ± 0.147 in the MyConnectome and HCP datasets respectively. Similar to whole-brain clustering, a difference was observed between the two clustering algorithms applied to both datasets. As before, the MyConnectome dataset demonstrated better along-tract agreement irrespective of the clustering method applied to the template. Supplementary table A.2 provides full details of computed ICC for all "U"-shaped tracts, with 95% confidence intervals.

Similarly, as previously observed, not all analysis datasets contained streamlines for all template identified tracts. 6 tracts in both the MyConnectome and HCP datasets contained no streamlines when tracts were identified with the spectrally clustered template, while 32 and 24 tracts respectively was found to contain no streamlines when identified with the QuickBundle clustered template. Variability of tract streamline counts was also comparable, ranging from 13 − 81% and 16 − 122% (averaging 37% and 50%) for MyConnectome and HCP datasets respectively identified via the spectrally clustered template. Similarly, variability of identified tract streamline counts from the QuickBundle clustered template ranged from 11 − 84% and 14 − 110% (averaging 38% and 49%) for MyConnectome and HCP datasets. Figure 2.4 displays for each dataset, a box plot with individual points indicating the observed values of a given tract for each described metric. A full summary of evaluated metrics of short-range, "U"-shaped tracts, inclusive of streamline counts can be found in Supplementary table A.2

The relationships between different reliability metrics were also similar to the relationships observed for whole-brain tractography clustering. Negative correlations were observed with the Euclidean distance for all metrics except for streamline count variability, which exhibited a positive relationship (Figure 2.5, left-most column). As with whole-brain

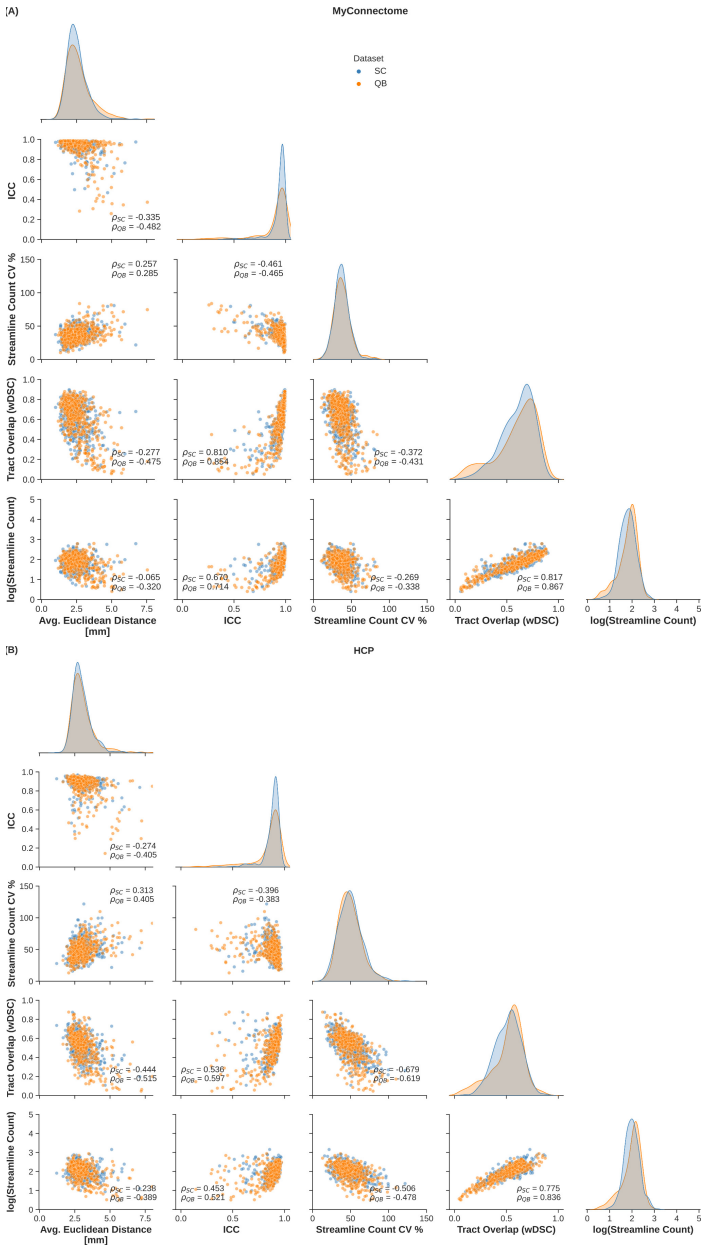

Figure 2.5: Spearman correlations are computed to explore relationships of metrics employed to assess reliability of spectral clustered (blue circles) and QuickBundle clustered (orange circles) identified tracts in short-ranged, "U"-shaped tracts. Relationships between different metrics used for assessment are shown in pairplots for (A) MyConnectome and (B) HCP datasets. Relationships between various metrics and average Euclidean distance from an average tract centroid (left-most), relationships with along-tract absolute agreement (ICC; middle-left column), relationships with streamline count variability (middle-column) and with voxel-wise spatial overlap (middle-right column) are displayed. Distribution of observed points for a given metric (matching the x-axis) are plotted along the diagonal.

tractography, negative correlations were identified between along-tract agreement of fractional anisotropy and both streamline count variability and the average log-transformed streamline count (Figure 5, middle-left column). Lastly, a significant positive relationship was once

again identified between the log-transformed streamline count (Figure 2.5, middle column) and voxel-wise spatial overlap (Figure 2.5, middle-right column). As before, the relationships were similar for "U"-shaped tracts identified via spectral clustering and the QuickBundles algorithm.

Lobular connectivity of "U"-shaped tracts was identified and summarized. The majority of tracts identified in both hemispheres were found within the frontal lobes, followed by the parietal lobes. A number of tracts were also identified to connect between the frontal and parietal lobes. A full summary of the lobular connectivity of "U"-shaped tracts can be found in Supplementary table A.3.

2.4 Discussion

2.4.1 Clustering reliability

Reliable identification of white matter pathways is crucial for increasing confidence in the subsequent analysis. In this work, we investigated the reliability of template-based clustering by identifying and evaluating metrics of reliability in identified tracts. On average, we observed identified tracts to exhibit a Euclidean distance around 2.5 *mm* (or 2 voxels) from the average centroid. A deviation from the average tract trajectory could result in an increasing Euclidean distance. Other factors, such as dispersion of streamlines (e.g. fanning in the corticospinal tract), could also contribute to an increased Euclidean distance.

Another reliability metric evaluated was the voxel-wise spatial overlap of corresponding tracts. Previous studies have used a Dice similarity coefficient to compute tract overlap [55, 138], but wDSC was chosen as it better reflects the overlap of streamlines by minimizing the penalization of those far from the core [133]. In healthy individuals, corresponding tracts are generally found in similar regions of the brain with comparable trajectories (more variability is expected in the superficial white matter). The wDSC reflects this similarity by comparing and identifying the voxels traversed by the two tracts being compared. If two tracts have similar trajectories, presumably also traversing similar voxels, this is reflected by a higher degree of spatial overlap when brought into the same space (e.g. template space). In the study by Zhang et al. [103], clustering demonstrated greater reliability than ROI-based techniques in a study of test-retest datasets, exhibiting a minimum tract overlap of 0.593 from a clustering approach compared to 0.362 with a ROI-based approach. Here, we provide further support for template-based clustering approaches, demonstrating an average wDSC across the two techniques and datasets evaluated that is greater than reported by Zhang et al., indicating a high degree of

overlap.

Along-tract quantitative measurements can also be a good indicator of tract reliability, as noted by Cousineau, Descoteaux, and Takemura [135]. Corresponding tracts are expected to have similar along-tract profiles and deviation from this profile could indicate an incorrect tract was identified. In this study, the absolute agreement of along-tract fractional anisotropy was assessed between corresponding samples of tracts across subjects and sessions. The majority of identified tracts within a given dataset and technique exhibited good agreement between their tract profiles.

Tract streamline counts and the variability across subjects and sessions were also evaluated. While the method of tractography seeding can influence the resulting streamlines, methods such as SIFT, were developed to filter and retain streamlines such that streamline counts are reflective of the underlying diffusion profile. Further, different individuals may also contribute to this variability due to underlying anatomy. However, within a single healthy adult individual with developed brain, tract streamline counts should be similar (i.e. on the same order of magnitude). In this study, a slightly smaller variability was observed in the MyConnectome dataset relative to the HCP dataset, but a high variability was still demonstrated in the majority of identified tracts. The observed variability could suggest streamline counts and the associated variability may not be a dependable indicator of reliability. Nonetheless, if streamline counts are to be assessed, careful processing should be performed to ensure they are comparable, such as applying post processing techniques to correspond to the underlying diffusion signals, such as with SIFT [124].

2.4.2 Reliability metric relationships

While the chosen metrics evaluated can all be used individually to characterize the reliability of tract identification, certain relationships were observed between different metrics of reliability. We have shown that the spatial overlap of identified tracts demonstrated good reliability across other metrics, such as low streamline count variability demonstrating the need for filters like SIFT that attempt to match the streamline counts to underlying diffusion signals. Similarly, a low Euclidean distance was also observed with low streamline count variability, as well as high tract overlap. However, along-tract agreement (ICC), did not demonstrate such a relationship with other reliability metrics. Instead both high and low reliability across other metrics were observed when ICC suggested good reliability. Lastly, similar relationships were observed for both whole-brain tractography and “U”-shaped tractography, suggesting that template-based

clustering may be appropriate for both.

2.4.3 "U"-shaped tract clustering

Clusters identified from whole-brain tractography can contain multiple "U"-shaped tracts clustered together and affecting the evaluated metrics described previously. One such example was in clusters with a large number of streamlines (> 1000). The close proximity of these streamlines could contribute to a smaller Euclidean distance and a high degree of overlap observed. As such, it is important to separate evaluation of "U"-shaped tracts from whole-brain tractography, which is possible by lowering the Gaussian kernel width for spectral clustering and the distance threshold for QuickBundles.

We separately assessed the clustered "U"-shaped tracts with the same metrics used to study whole-brain tractography. Much of the same observations noted previously in whole-brain tractography were also seen in these "U"-shaped tracts. The use of a template may alleviate some of these issues, capturing tracts that have similar trajectories across individuals. Conversely, "U"-shaped tracts specific to an individual may be missed. Notably, a slight increase in the computed Euclidean distance was observed for QuickBundle identified tracts. Further, a decrease in spatial overlap was observed in "U"-shaped tracts irrespective of the algorithm chosen. Additionally, the QuickBundles clustered template resulted in the lack of streamlines in more tracts of both datasets, which could be due to clusters of outlier streamlines in the template. It has been previously noted that the QuickBundles method may capture outlier streamlines in small clusters [128] as it uses a distance threshold for cluster assignment without discarding any streamlines. While discrepancies observed between clustering algorithms may be attributed to implementation differences of evaluated algorithms or the choice of parameters, an overall decrease in reliability (as seen from tract overlap), indicates that improvements still need to be made to improve the reliability of identifying "U"-shaped tracts.

2.4.4 Inter- vs intrasubject

In this work, we utilized two unique datasets: an intersubject dataset acquired to investigate the human brain in the Human Connectome Project and an intrasubject dataset acquired over a 3-year period to similarly investigate the human brain using similar acquisitions. In assessing template-based clustering reliability, similar observations were made across both datasets. While minimal change would be expected in the developed brain of a single subject, some variation is expected across different individuals [133], which may contribute to the differences observed between the two datasets. When examining "U"-shaped tracts, this expectation

appeared to be reflected in the evaluated metrics, with tracts identified in the single subject dataset demonstrating slightly less variability as previously noted.

2.4.5 Template-based clustering

In addition to the use of two unique datasets, the processing was also performed with two different clustering tools using similar parameters: spectral clustering and QuickBundles [53]. Analysis was performed on both for comparison of reliability in two different template-based clustering tools. Differences between the two clustering algorithms were observed, particularly when performing whole-brain clustering. These differences may be attributed to disparities in the implementation of the two algorithms, including the handling of outlier streamlines as previously mentioned. Further, while the clusters may not correspond across these two different techniques, and the relationships observed from the results of both techniques were similar, suggesting the robustness of a template-based approach in reliably identifying tracts. A previous study had explored the challenges of tractography, assessing the pathways identified by various different methods [54]. Here, we explored the reliability of template-based clustering algorithms. As tools and techniques are developed and refined to automate tract identification, the importance of assessing the reliability of these methods should be emphasized.

2.4.6 Limitations

Clustering of tractography, both with spectral clustering and using QuickBundles, required streamlines to be resampled to N equispaced samples. Subsequent analysis was also performed on these samples along a given tract. However, streamlines comprising a tract may be of different lengths, with some streamlines terminating earlier than others due to meeting cutoff criteria. Despite differing lengths, correspondence is assumed between two samples. One method of resolving this is to set terminal ROIs at the ends of a tract such that all streamlines are guaranteed to terminate or be cutoff at the ROIs. As previously noted when discussing manual placement of ROIs, this requires some anatomical knowledge [48]. Alternatively, Chandio et al. [139] mapped samples from streamlines to a corresponding segment of a representative centroid. This eliminates the need for ROIs, but still requires an adequate registration. Further evaluation of this method is also required to determine its accuracy in mapping superficial white matter.

Clustering performed in this study also used a template to identify corresponding tracts in the analysis datasets. While clustering does not explicitly require registration, the template-based techniques examined here require an adequate registration between the template and the sub-

ject of interest [11,48,66,98] to identify corresponding tracts across subjects and sessions. Additionally, template-based techniques can only identify tracts with similar trajectories to those already defined by the template. ROI-based techniques can be used to identify tracts of interest, but as mentioned in the introduction, these methods can be laborious and require anatomical knowledge. A combination of the data-driven approaches taken here complemented by the use of ROIs for refinement to ensure proper termination of pathways may be better suited to aid discovery of new tracts *in vivo*.

As previously mentioned, the clustering performed utilized two different techniques and comparison of tracts across these two methods was not possible due to lack of correspondence of identified tracts. Differences include how streamlines were clustered, where spectral clustering performs k-means clustering in a spectral space to identify tracts, QuickBundles identifies similar streamlines by directly employing the MDF distance and adding the streamline to a cluster if the distance threshold is satisfied. Differences in the algorithm are likely the cause behind the differences observed. Nonetheless, the metrics used to evaluate the identified tracts and the comparison of the metrics can be applied generally to assess reliability regardless of the tract identification technique chosen.

Despite the influence of the HCP acquisition protocol on the MyConnectome acquisition protocol, there are notable differences between the two datasets. HCP dMRI was acquired with 3-shells and 270 total directions (90 directions/shell), while MyConnectome dMRI was acquired with 2-shells and 60 total directions (30 directions/shell). Additionally, preprocessing of data may slightly differ, with the HCP data preprocessed with the HCP minimal preprocessing pipeline [107] and the MyConnectome data preprocessed using an in-house pipeline to apply standard preprocessing steps. Preprocessed HCP dMRI data was also corrected for gradient field inhomogeneities, whereas the correction for gradient field inhomogeneities was not possible for the MyConnectome dataset due to the lack of a proprietary scanner-specific file required. Data harmonization - an active area of research - is one possible method to improve comparability between different datasets, as such, future work should also explore the reliability of harmonized datasets.

To match the number of diffusion acquisitions available in the MyConnectome dataset, n=15 subjects were selected from the HCP dataset to keep analysis as similar as possible between the two datasets. As previously mentioned, variability within a single, healthy adult individual is expected to be minimal, there may be more variability in the larger population. In particular, more variability may be expected in the superficial white matter due to differing cortical

folding patterns across individuals. In this study, we have shown the ability of template-based clustering to identify corresponding tracts across individuals in the limited sample size. Future studies should explore and quantify the amount of variability, in particular to the superficial white matter, across a larger population.

With regards to clinical applications, such as in neurological and psychiatric disorders, which have been recognized as disorders of the network (e.g. epilepsy as a network disorder [140], abnormal networks in schizophrenia [141], and more), the capability to identify connectivity throughout the brain, including previously unnamed and unidentified tracts in a reliable manner has important clinical implications. The techniques applied in this study may be able to provide biomarkers indicative pathological changes if tracts can be identified in the presence of disease. However, one of the current limitations of the template-based approach is the requirement of adequate registration, which may be non-trivial with the occurrence of substantial morphological change (e.g. due to tumors). The current study suggests that while template-based approaches are reliable for identifying connectivity and may be a critical approach in expanding current knowledge of the human connectome with potential future clinical impact, improvements are required to tackle the challenges of identifying connectivity in the presence of disease.

2.5 Conclusion

In this work, we performed whole-brain tractography on two unique datasets, assessing the reliability of template-based clustering approaches and identifying relationships between reliability metrics. Similar relationships were observed irrespective of the clustering algorithm chosen suggestive of the robustness of template-based approaches. Furthermore, streamline count on its own may not be a good indicator of reliability, though the evaluation of the metric relationships suggest that certain metrics may be in agreement with other measures, providing a better indicator of reliability. We further identified the superficial white matter ("U"-shaped) tracts using the same clustering algorithms to assess reliability of a template-based approach, observing similar relationships as in whole-brain tractography. Data-driven, template-based approaches can reliably identify and investigate pathways, including those previously unnamed or unidentified such as the superficial white matter.

Future work should look to examine reliably identified "U"-shaped tracts to improve understanding of its biophysical properties, the relationship with cortical measurements (e.g. gyrification), and how the short-range pathways are affected in patient populations.

Chapter 3

Mapping the subcortical connectome using in vivo diffusion MRI: feasability and reliability

This chapter is based on the following manuscript:

- Kai, J., Khan, A.R., Haast, R.A.M., Lau, J.C. (2022). Mapping the subcortical connectome using in vivo diffusion MRI: feasibility and reliability. Terra incognita: diving into the human subcortex, special issue of NeuroImage.
  https://doi.org/10.1016/j.neuroimage.2022.119553

3.1 Introduction

A brain network is comprised of bundles of axons, which form the structural pathways (also referred to as tracts or connections), that allow transfer of information between the different regions [41] and facilitate the performance of complex functions [88, 89]. Axons can be computationally reconstructed (represented as a streamline) using diffusion magnetic resonance imaging (dMRI), a non-invasive technique sensitive to the direction of water motion [91, 92]. As axons are bundled together, water molecules will preferentially diffuse parallel to the axonal trajectory, which can then be detected using dMRI to enable an *in vivo* estimation of tract trajectories. This process, known as tractography, first estimates the diffusion orientations within all imaging voxels before traversing from a starting seed location until termination criteria are met (e.g. quantitative value drops below defined thresholds) [41]. Additionally, regions of interest (ROI) can be used to define inclusion and exclusion criteria to constrain tract trajectories and facilitate identification of connections between terminal regions.

Mapping the human connectome is an important, non-trivial task that contributes to disentangling the network organization of the brain and increased understanding of changes in healthy aging or due to disease [142, 143]. To date, much of the work studying structural connectivity using dMRI has focused on the cortico-cortical (between regions of the cortex) and cortico-subcortical (between cortex and subcortex) tracts, resulting in the development of a number of structural connectivity atlases. Such connectivity can be described as the cortical connectome. Examples of such atlases include the Johns Hopkins University white matter atlas, which identified a number of cortico-cortical white matter tracts [50, 144, 145] and the Oxford thalamic connectivity atlas, which aimed to identify cortico-subcortical connectivity between regions of the thalamus and the cortex [46, 146]. These atlases have been extensively used to attain an understanding of changes associated with aging as well as disease (e.g. thalamic changes in Alzheimer's disease; [147]). Validation of some of these connections have also been performed previously in studies of non-human primates (NHPs; [148–150]).

Just as there are cortical connections, there is also connectivity between subcortical structures

(e.g. the thalamus and basal ganglia), forming the subcortical connections, which can also be referred to as subcortico-subcortical connections. These subcortical structures are important to motor control [13, 14] as well as cognition and emotion [15]. Accordingly, connections between the subcortical structures are integral and have been studied extensively in non-human primate (NHP) studies of the motor network [5, 13, 151], as well as associative and limbic networks [5, 152–154]. Previous studies have examined subcortical connections with the use of anatomical tracers, which involve injection of either anterograde or retrograde tracers at a structure of interest to map its connections. One such example involved the injection of an anatomical tracer at the ventral pallidum, which determined projections to the subthalamic nucleus (STN), as well as the hypothalamus and brainstem [155].

Studies that attempt to more comprehensively identify the subcortical connections non-invasively via tractography, that is to map the subcortical connectome, have been limited. The scarcity of subcortical connectome studies is in part due to the difficulty of tracking the connections in a compact region where the underlying diffusion signal is complicated by multiple diffusion orientations arising from numerous intersecting connections and structures with low anisotropy. One previous study demonstrated the ability to map connections between the basal ganglia and thalamus *in vivo* using manual segmentations before leveraging connectivity strength to parcellate the basal ganglia and thalamus into subregions [156]. Recently, *in vivo* studies have primarily focused on individual connections that comprise specific subcortical connections and have been identified as putative targets for surgical neuromodulation [77, 78]. In one study, the pallidothalamic tract was delineated in order to study its role in the treatment of dystonia with deep brain stimulation (DBS) [77], while another study examined the importance of pallidoputaminal connectivity to predict DBS outcomes also for dystonia [80]. With the aid of a number of atlas-based inclusion and exclusion ROIs, as well as extensive manual refinement, tractography has been used to identify the nigrofugal and pallidofugal subcortical connections [78]. Recently, an attempt was made to map subthalamic tracts using *ex vivo* data, using ROIs to guide and identify specific subcortical connections [17]. All of these studies employed tractography to identify the trajectory of the connections using non-invasive techniques, highlighting a potential for tractography-guided treatment. Reliable and accurate identification of these connections has the potential to improve diagnosis and treatment options.

With reliability studies having been previously performed in tractography studies of cortical connectivity (including, but not limited to [56, 133, 157, 158]), an evaluation of the reliability of the subcortical connectome is also warranted. Despite examination of individual subcortical connections, to our knowledge, there has yet to be a study assessing the reliability of the

subcortical connectome. Briefly, reliability is defined as the agreement of the results (e.g. similar connectivity) when applying the same methodology to different acquisitions of the same subject or to data acquired from different subjects. Not to be confused with reproducibility, another term that often gets used interchangeably, which is defined as the ability to produce similar results when using an entirely different methodology. Both are important and can provide valuable insight regarding a method or result. Reliability studies can evaluate and increase the confidence of methodological approaches used to study structural connectivity, while reproducibility studies can validate findings by comparing results produced with other techniques. In this work, we recapitulate pathways of the subcortical connectome in the Human Connectome Project (HCP) test-retest dataset. We aimed to assess the feasibility and reliability of mapping the subcortical connectome, with a specific goal of recapitulating known connections, through application of subcortical structure segmentations and probabilistic tractography. Furthermore, we sought to develop a framework that enabled evaluation of reliability for the subcortical connectome moving forward. Additional validation was performed using the unrelated subjects dataset of the HCP.

3.2 Materials and methods

Processing of the data was performed in containerized computing environments on a high performance compute cluster. An overview of the general workflow is shown in Figure 3.1. Briefly, publicly available minimally pre-processed test-retest data from the Human Connectome Project was used to assess reliability of connections (identified via tractography) between subcortical structures and feasibility of identifying connections of known subcortical circuits. Analysis included evaluating tract overlap, changes in tract density, and examining identified connections with trajectories previously described in the literature. Furthermore, processing and analysis was replicated on an unrelated subset from the Human Connectome Project.

3.2.1 Dataset

Minimally pre-processed subjects as part of the test-retest dataset (n=36; 11M/25F, aged 22-35) of the Human Connectome Project (HCP) [107, 108] were used to assess the reliability of subcortical connections identified via tractography. Briefly, T1-weighted (T1w) MRI scans were acquired with a 3D MPRAGE sequence [159]: resolution = 0.7 mm isotropic voxels; repetition time/echo time (TR/TE) = 2400 / 2.14 ms, while dMRI scans were acquired in opposite anterior-posterior phase-encoding directions with a pulsed gradient spin-echo sequence [30]: resolution = 1.25 mm isotropic voxels; TR/TE = 5520 / 89.50 ms; b-values = 1000, 2000, 3000

s/mm^2 (90 directions per shell) with 18 b-value = 0 s/mm^2 images. All data was acquired on customized Siemens Skyra 3T MRI systems [110, 111]. Full acquisition details are described

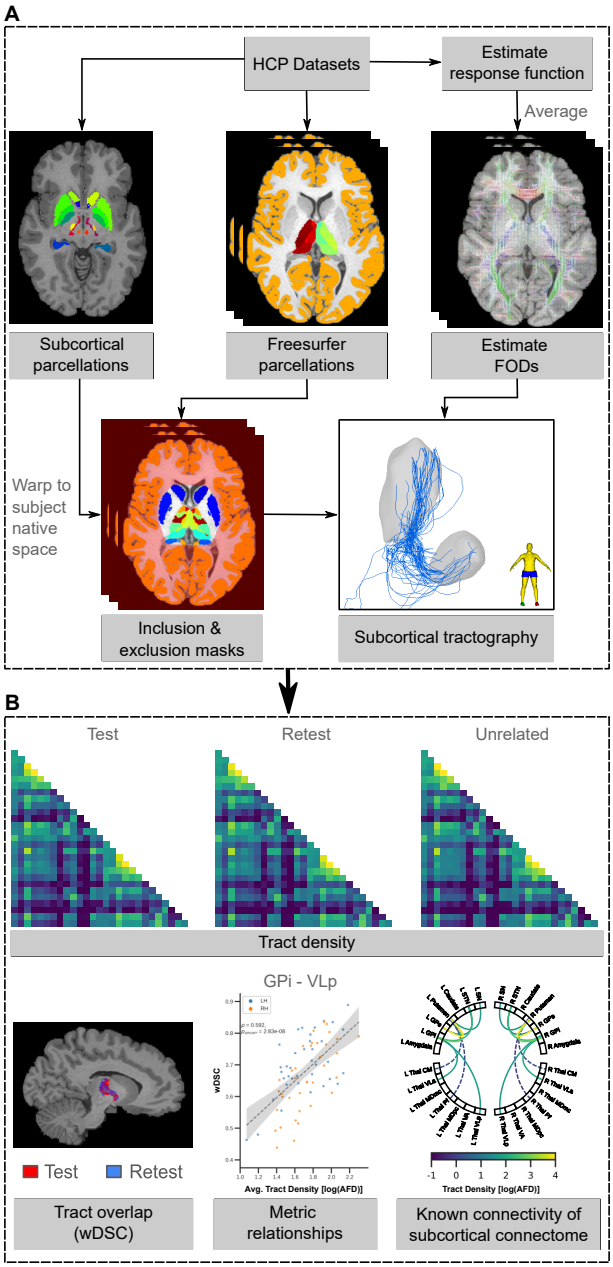

Figure 3.1: General subcortical tractography processing workflow using the minimally preprocessed HCP datasets. (A) An average response function was created from individual response functions from each acquisition (per dataset) and to estimate the FODs in each MRI session. Additionally, FreeSurfer was employed to parcellate the thalamus and obtain a cortical ribbon. Inclusion and exclusion masks were created, combining subcortical parcellations (transformed to the subject's native space) with FreeSurfer parcellations to perform tractography on the subcortical connectome. (B) Examples of assessments performed, comparing test vs retest sessions, as well as the use of an additional unrelated dataset for further comparison.

in the HCP1200 reference manual[1]. As part of the minimal pre-processing pipeline data release, all subjects underwent FreeSurfer processing (v5.3.0-HCP; [109]), where the cortical ribbons were retained for further processing.

Further, subjects part of the HCP unrelated dataset that did not overlap with test-retest dataset were selected (n=85; 35M/50F; aged 22-35) for validation. Acquisition and minimal pre-processing steps from the HCP release of the unrelated dataset were identical to the test-retest dataset.

3.2.2 Regions of interest

To evaluate connections of interest, structural segmentations were used as ROIs to assist tractography generation. As previously mentioned, cortical reconstruction from FreeSurfer [109] was first performed, retaining the cortical ribbon as an exclusion mask. In addition, subcortical structures where connections terminated were identified. Subnuclei of the thalamus were segmented using FreeSurfer (v7.1.0; [160]), while other subcortical structures (excluding the hippocampus, which is considered part of the archicortex; [161, 162]) were identified from the BigBrain subcortical atlas [163] first registered to the MNI2009bAsym template [164]. Volumes of all subcortical structures were computed for each subject. A second exclusion mask was created from an inverted convex hull surrounding the subcortical structures to discard streamlines outside of the convex hull. FreeSurfer processing was performed in the subject's native space, while the atlas was transformed to subject's native space using the Advanced Normalization Tools (ANTS v2.1.0; [165]). Briefly, the atlas was transformed to the subject's native space in a 3-step process: (1) linear affine transformation (2) non-linear symmetric normalization (SyN), and (3) HCP provided subject-specific transformations. The first two steps transform the labels from MNI2009bAsym space to MNI152NLin6Asym space, while the final step transforms the labels to the subject's native space. Transformations between the two spaces can be found in the available repository (see data availability).

3.2.3 Tractography

All tractography processing was performed using the MRtrix3 software suite (v3.0_RC3; [105]). First, individual tissue-specific response functions were estimated for each subject in both test and retest sessions using an unsupervised approach [120]. From here, an averaged group response function was computed from the individual response functions. Fiber orientation distribution (FOD) maps were estimated for each subject with a multi-shell, multi-tissue constrained

[1] https://humanconnectome.org/study/hcp-young-adult/document/1200-subjects-data-release

spherical deconvolution (MSMT-CSD) algorithm [121], with group average response functions independently computed for the test-retest and unrelated datasets. The use of a group average response function minimizes biases in FOD maps [166], improving the comparability of tractography within datasets with observed differences attributed to the underlying diffusion data of an individual. Prior to performing tractography, multi-tissue informed log-domain transformed normalization was performed [167] on the FOD maps.

As the primary diffusion orientation is also reflected in FODs, major white matter connections (e.g. the corticospinal tract (CST)) passing through the subcortical region will hinder the ability to identify subcortical trajectories. To traverse trajectories along non-primary diffusion orientations, the iFOD2 probabilistic algorithm [123] with a step-size of 0.35 mm and maximum angle of 45° between successive steps was used. Random seeding was performed throughout the brain until 20 million streamlines, constrained to the subcortical region with the previously created exclusion mask, were selected. The chosen parameters are comparable to what is typically used in iFOD2 algorithms to perform whole-brain tractography with a noted decrease in step-size (from 0.5 $\times$ voxel size to 0.25 $\times$ voxel size) to sample more frequently along a streamline's trajectory.

Following tractogram creation, each streamline was assigned a weighting to reflect its contribution to the underlying diffusion signal using the updated spherical deconvolution informed filtering of tractograms (SIFT2) technique enabling the assessment of tract densities [168]. Using MRtrix3, structural connectivity was established by identifying the nearest subcortical label within a 1.5 mm radius at each terminal end of a given streamline. Due to the low anisotropy within gray matter, streamlines whose trajectories intersect other subcortical labels prior to reaching the terminal structures were discarded (see section 3.4). Furthermore, the CST, which represents a dominant tract passing in proximity to many subcortical connections, was separately identified in order to visually assess its influence on derived tracts. Identification of the CST was performed using the brainstem and segmentations of both pre- and post-central gyri identified by FreeSurfer as inclusion regions of interest. Generation of the CST was performed until 500 streamlines were identified in each hemisphere. Similar to the connectivity of the subcortical connectome, streamlines had to terminate within a 1.5 mm radius of these segmentations to be considered a part of the CST.

3.2.4 Assessment of reliability and accuracy

An investigation into known subcortical connections of the motor, limbic, and associative networks was performed, quantitatively assessing reliability of tract densities and spatial overlaps of identified connectivity. Connectivity between structures associated with the networks were identified and extracted [5, 13, 151], with both ipsilateral self-connections (i.e. tracts that start and end in the same ROI) and inter-hemispheric connections excluded from analysis. Further, subcortical connections that connect to thalamic nuclei on both terminal ends were also excluded. Visual inspection of known connections of the subcortical connectome was also performed to evaluate accuracy of tractography-produced trajectories with previously described literature.

3.2.5 Anatomical assessment

Using the method employed to identify connectivity between subcortical structures, a large number of potential connections were found. Since our goal was to recapitulate known subcortical connections with *in vivo* tractography, we focused on those that have been well described in the literature depicting motor, associative, and limbic subcortical circuitry [5, 13, 151]. Connectivity between subcortical structures of the basal ganglia and thalamus were both visually and quantitatively examined, evaluating tract trajectories, densities, and overlap.

3.2.6 Tract density

Streamlines weighted by their contribution to the underlying diffusion signal were summed to calculate the tract density (also referred to as apparent fibre density (AFD); [166]) of the connection between two subcortical structures. A connectivity matrix for each subject was created with the AFD representing the edge strength between two ROIs (nodes). Further, the percent change in AFDs were calculated between test and retest sessions using equation 3.1:

$$AFD_{Diff} = \frac{AFD_{Test} - AFD_{Retest}}{AFD_{Test}} \times 100\% \tag{3.1}$$

Additionally, intraclass correlation (ICC) was computed for the tract densities between the two datasets as a metric of consistency using a two-way, mixed effects model [136]. Prior to computing an ICC, an analysis of covariance (ANCOVA) was first performed to identify and account for covariates (age, subject motion, brain volume) with a significant effect on the tract density via linear regression. In this model, the "raters" (column factor) were the corrected tract densities and the "targets" (row factor) were the test and retest session connectivity. A paired t-test was also conducted between average AFDs of the test and retest sessions. To

compare average connectivity of the basal ganglia with average connectivity between the basal ganglia and thalamus, an one-way ANOVA was performed. The impact of ROI volume on AFD was assessed using ordinary least squares multiple regression, treating the average ROI volume across subjects as an independent variable and average AFD as the dependent variable. Further, Spearman's correlation was performed between average AFD and the absolute percent change between test and retest sessions.

3.2.7 Voxel-wise spatial overlap

A AFD map was first created for each tract identified in the test and retest sessions by identifying streamlines passing through each voxel. The sum of streamline weights were assigned to corresponding voxels. Following assignment of streamline weights, the fraction of the tract (a value between 0 and 1) passing through a voxel is determined from the AFD map and used to compute the overlap between tracts from the weighted Dice similarity coefficient (wDSC; [133]). Briefly, the wDSC is a modified Dice similarity coefficient for assessing tractography overlap, minimizing the penalization applied to streamlines further from the core of the tract [133]. The wDSC is computed from equation 3.2:

$$wDSC(A, B) = \frac{\sum_{v'} A_{v'} + \sum_{v'} B_{v'}}{\sum_{v} A_{v} + \sum vB_{v}} \tag{3.2}$$

where A and B represent the fraction of streamlines (between 0 and 1) passing through a voxel and v' represents a corresponding non-zero voxel in A and B. The numerator of equation 2 computes the sum of overlapping non-zero voxels between A and B, while the denominator calculates the total sum of non-zero voxels in A and B respectively. Computed overlaps from wDSC follow similar indicators of agreement as the conventional Dice similarity coefficient: poor (< 0.2), fair (0.2–0.4), moderate (0.4–0.6), good (0.6–0.8) and excellent (> 0.8; [169]).

In addition to comparing the tract overlap, a Spearman's correlation was also computed between the average AFD across the two datasets. Similar to AFD, a one-way ANOVA was performed to compare the wDSC for connectivity of the basal ganglia with connectivity between the basal ganglia and thalamus.

3.2.8 Identifying a connectivity threshold

A threshold was defined, such that connections which meet the threshold could be considered reliable. This threshold was then applied to determine the reliability of the known connections as defined by previous literature and identified with tractography. As noted in previous studies,

defining a threshold is a non-trivial task [170, 171]. If the chosen threshold is too low, tracts that are not reliably identified may remain, including those that do not exist in reality, but if it is too high, legitimate connections may be discarded. Common approaches include choosing an arbitrary threshold such that the majority of the subjects to be analyzed retain the same connections [172] or by sweeping through a range of thresholds [173]. More recently, a test-retest metric was proposed, wherein reliability was evaluated across a range of thresholds and a final threshold was selected where the change was at a minimum [171]. Here, we selected our threshold by following a similar test-retest reliability procedure, using the tract overlap (wDSC) as the reliability measure. We first stepped through a range of AFD values to threshold the connectivity matrix before calculating the wDSC for each thresholded matrix. Additionally, we computed the change in average wDSC between each step across the range of AFD values. The wDSC threshold is selected at the first occurrence where the change between steps is 0 and identified the corresponding average AFD threshold. Supplementary Fig. B.1 demonstrates examples of the connectivity matrix at different thresholds of tract overlap.

3.2.9 Validation with unrelated dataset

Processing and analysis of the HCP unrelated dataset followed the same workflow as before with the test-retest dataset. As before, known connectivity of the subcortical connectome was both visually and quantitatively assessed. AFD matrices were computed for each subject as before, and further separated by hemispheric connectivity to compare with previous findings. With only a single acquisition session in the unrelated dataset, an average AFD matrix was computed across subjects, and a Pearson's correlation was performed against the average AFD matrices of the test and retest sessions to evaluate the similarity of the subcortical connectome. As with the test-retest dataset, the relationship between AFD and the size of the subcortical structures was also evaluated.

3.3 Results

3.3.1 Networks of the subcortical connectome

We investigated the ability of *in vivo* tractography to both identify and reliably reproduce the connectivity between different acquisitions of the same human subject, focusing on known subcortical connections of the motor, associative, and limbic circuits [5, 13, 151].

3.3.1.1 Identification of known subcortical connections

Motor network connectivity using the described tractography methods could successfully recapitulate known connections as previously described in the literature (Figure 3.2). Similarly, known connections of both the associative and limbic network connectivity were also successfully captured (Supplementary Figure B.2A and Supplementary Figure B.2B respectively). A

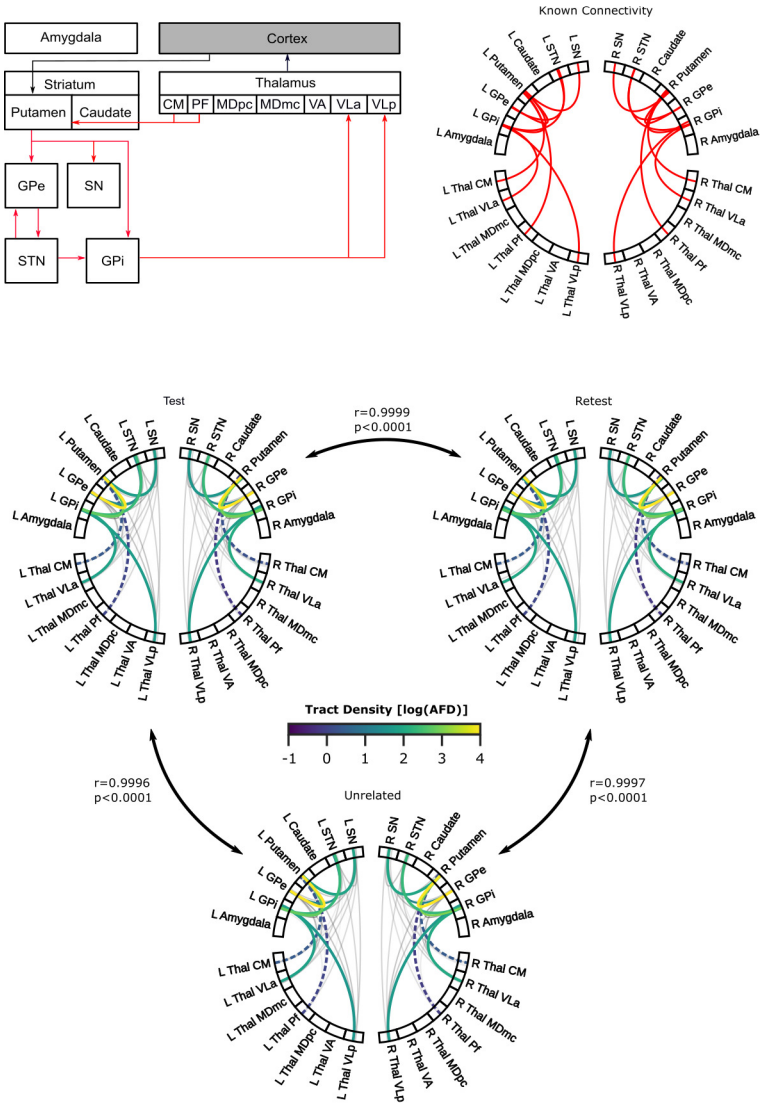

Figure 3.2: Diagram of known anatomical subcortico-subcortical connections (in red) of the motor network. (A) Connections identified from literature are depicted in a diagram (left) and chord plot (right). (B) Chord plots exhibiting average log-transformed tract densities from tractography derived connections are displayed for test-retest (top-left, top-right) and unrelated (bottom) datasets from the Human Connectome Project. Coloured lines represent known connections, with dashed coloured lines specifically indicating known connections that did not meet the selected tract density threshold. Grey lines denote connections identified from tractography, but not identified in tract-tracing literature. Pearson correlations between datasets are shown next to the comparison indicators.

wDSC of 0.58 was selected as the final overlap threshold, which corresponded to a AFD threshold of 6.5 AFD. Of the known connectivity comprising the motor network, 78% (14 out of 18) of the identified connections met the threshold. In the associative and limbic networks, 100% and 79% (11 out of 14) of the observed connectivity met the AFD threshold respectively. Connectivity failing to meet this threshold was commonly found between a thalamic nucleus (which was often small) and another subcortical structure (see Supplementary Table B.5 for full details), for example, between the putamen and the centromedian and parafascicular nuclei of the thalamus in both test and retest sessions. Connectivity between the globus pallidus internus (GPi) and either division of the mediodorsal nucleus of the thalamus failed to meet the AFD threshold in both test and retest sessions (both hemispheres for the magnocellular division and left hemisphere for the parvocellular division).

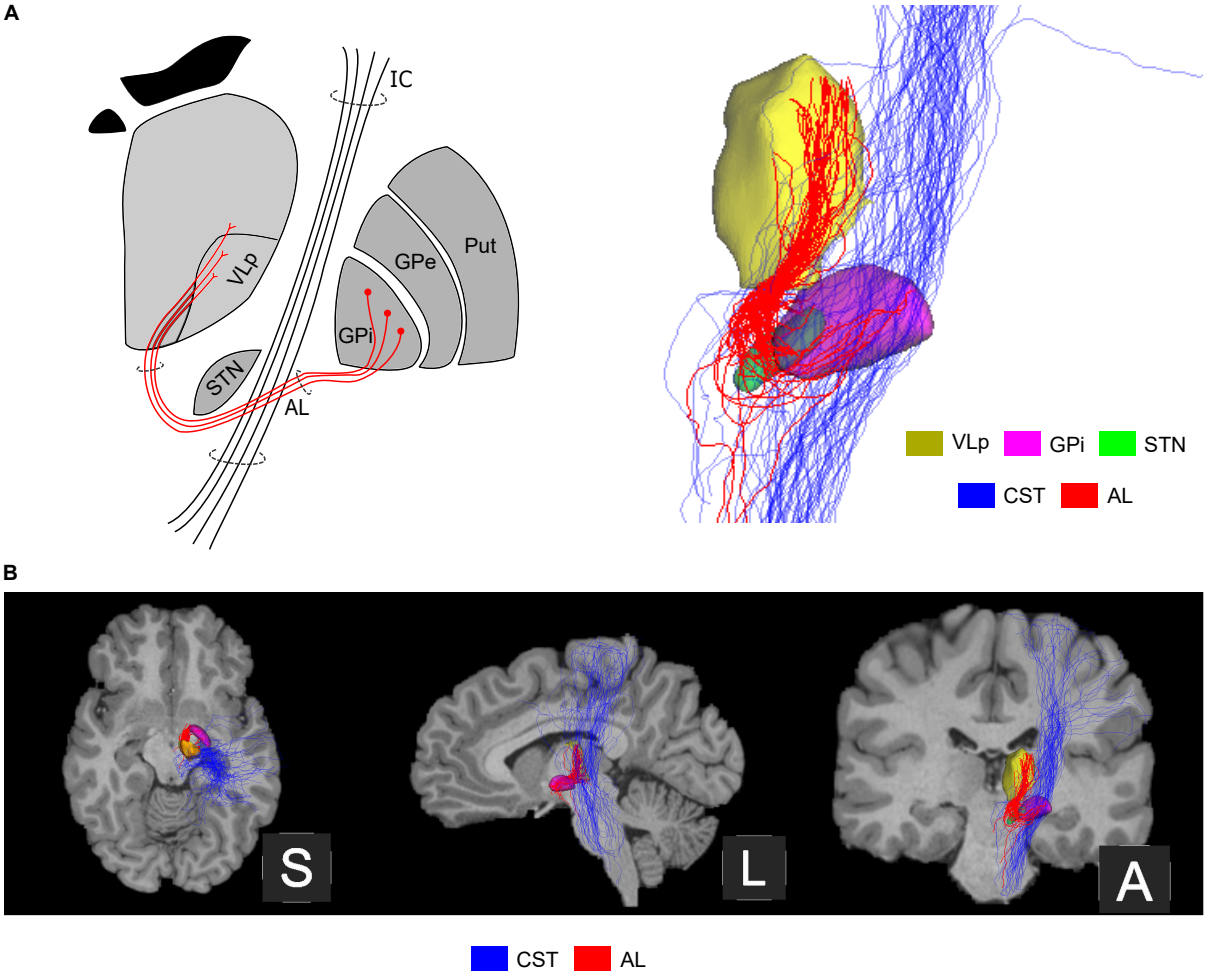

Figure 3.3: A single subject example of a connection found between the internal segment of the globus pallidus (GPi) and ventrolateral posterior nucleus of the thalamus (VLp). Manual refinement of tractography and construction of full corticospinal tract trajectory was performed for visualization purposes. (A) Depiction of ansa lenticularis (AL) from the tract tracing literature (left), compared with tractography identified trajectory (right) viewed from coronal anterior. The CST is also displayed to demonstrate the major WM tract passing through. (B) Three views (from left to right): superior, sagittal left, and coronal anterior exhibiting the trajectories of AL and corticospinal tract (CST) overlaid on a T1-weighted anatomical image.

Identified connections were also visually inspected, examining the connected structures and their trajectories. In observations of tract density, it was previously noted that basal ganglia connections (e.g. non-thalamic ROI to non-thalamic ROI) were denser, while connections between the basal ganglia and thalamus (e.g. non-thalamic ROI to thalamic ROI) were sparser. Visual inspection of the known trajectories, reflected the previous observation of denser connectivity between basal ganglia structures, which are also shorter and more direct. Conversely,

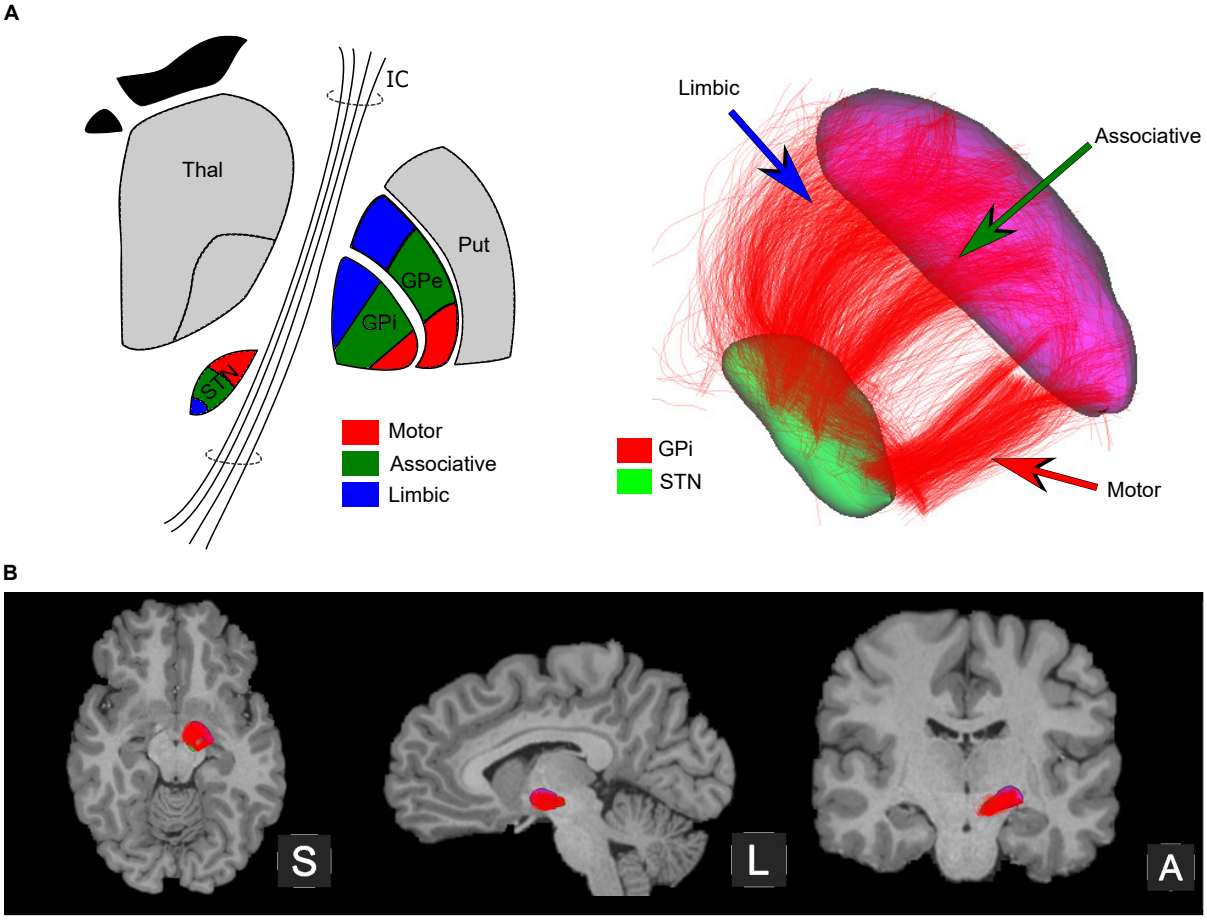

Figure 3.4: A single subject example of a connection found between the globus pallidus internal segment (GPi) and subthalamic nucleus (STN). For visualization purposes, refinement of tractography was performed and opacity was reduced to 20% to highlight the different segments observed. (A) Depiction of the approximate regions associated with different networks (e.g. motor, associative, limbic), identified from the literature (left) is shown for the STN and both internal and external segments of the globus pallidus: motor (red), associative (green), limbic (blue). Tractography identified trajectories (right) between the STN and GPi are shown from an inferior-to-superior (ventral) view, highlighting the different components associated with each network. (B) Three views (from left to right): superior, sagittal left, and coronal anterior exhibiting the connectivity between GPi and STN overlaid on a T1-weighted anatomical image.

connections between the basal ganglia and thalamus were sparser with longer and more curved trajectories. These longer trajectories increased the potential for intersecting GM structures between the basal ganglia and thalamus as was the case for connections between the ventrolateral anterior nucleus of the thalamus (VLa) and GPi (Figure 3.3), as well as between STN and globus pallidus externa (GPe) / GPi (Figure 3.4). It was observed that certain thalamic nuclei were more difficult to reach, as trajectories would have to pass through other surrounding thalamic nuclei. Some spurious streamlines were also noted (e.g. streamlines that looped in the brainstem). Full descriptions of known subcortical connections can be found in Supplementary

Table B.5.

3.3.1.2 Reliability of known subcortical connections

The reliability of identified connections was evaluated via tract overlap within motor, associative, and limbic networks. Connections between basal ganglia structures exhibited good overlap (average wDSC = 0.751 and 0.722 for left and right hemispheres respectively), while connections between the basal ganglia and thalamus demonstrated moderate to good overlap with the VLa (average wDSC = 0.543 and 0.560 for left and right hemispheres), ventrolateral posterior nucleus of the thalamus (VLp; average wDSC = 0.527 and 0.451 for left and right hemispheres), and the ventroanterior nuclei of the thalamus (VA; average wDSC = 0.576 and 0.629 for left and right hemispheres), which all had boundaries in the easier to reach lateral region of the thalamus. Some of the connections to the thalamus in each network exhibited poor overlap (average wDSC = 0.176 and 0.167 for left and right hemispheres), coinciding with the same ones that demonstrated a low AFD. For connections between basal ganglia structures, a poor to moderate overlap was only found between the caudate and amygdala (average wDSC = 0.354 and 0.152 for left and right hemispheres), where the tract was sparse and trajectories would have had to pass through other GM structures (e.g. putamen, GPe, GPi). Additionally, lower overlap was observed in the connections between the basal ganglia and thalamus, in particular connections to the mediodorsal nuclei of the thalamus (MD), which was more difficult to reach and in which trajectories also had to potentially traverse other nuclei of the thalamus. Despite the overlap observed in a few connections, good overall reliability was demonstrated for connectivity of each network, with similar measurements for each hemisphere.

3.3.2 Evaluation of subcortical connectivity matrices

Connectivity matrices were created for both test and retest sessions between subcortical structures for all subjects. Visual assessments were first performed, followed by quantitative evaluation of all intra-hemispheric subcortical connections. Reliability of the subcortical connectome was also evaluated and noted to be similar to what was previously assessed for known connections.

3.3.2.1 Tract density of all intra-hemispheric connections

Connectivity matrices for test and retest sessions were created from the computed AFD between subcortical structures for all subjects. A visual assessment of the computed matrices was first performed, followed by a quantitative evaluation of the computed AFDs. Matrices were observed to be similar across subjects and test-retest sessions (Supplementary Figure

B.3). Connections between basal ganglia structures were often denser (AFD = 2.33 log(AFD) and 2.24 log(AFD)) in left and right hemispheres respectively, averaged across test and retest sessions) than connections between the basal ganglia and thalamus (AFD = 1.34 log(AFD) and 1.26 log(AFD)) in left and right hemispheres respectively, averaged across test and retest sessions). The difference between the two groups was also corroborated with a one-way ANOVA for both the left ($F = 19.19$, $p < 0.05$) and right ($F = 3.75$, $p < 0.05$) hemispheres. Figure 3.5A demonstrates the average tract densities across the test-retest session.

The influence that the volume of terminal subcortical structures had on AFD was also assessed. By plotting the average AFD against the volume of the two terminal subcortical structures (Figure 3.5B), the average tract density was observed to increase as the volume of one of the two

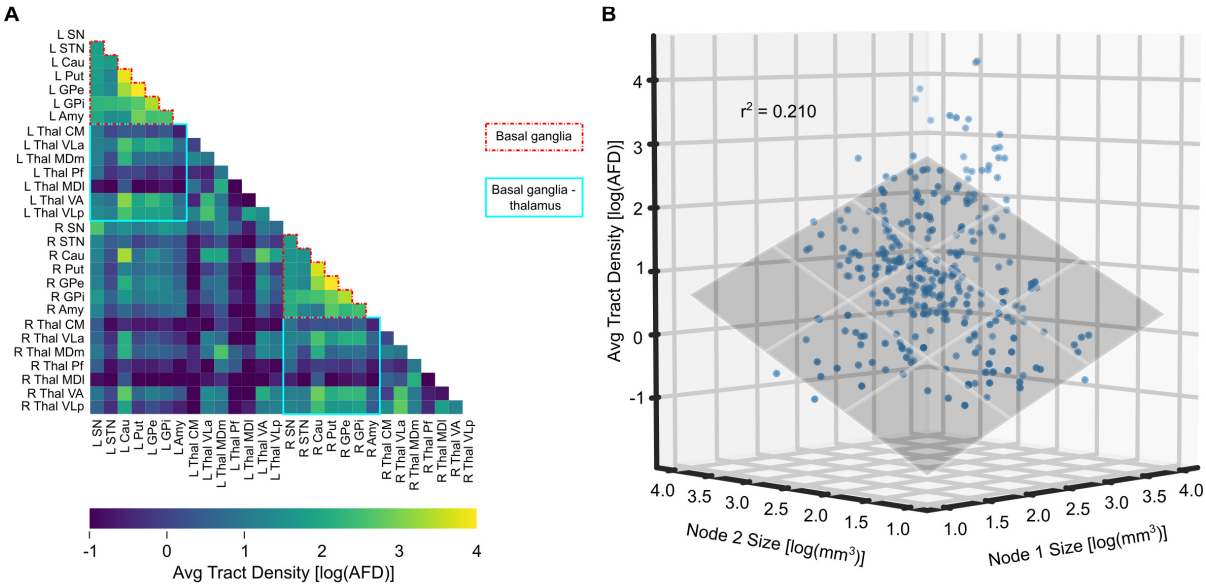

Figure 3.5: Averaged log-transformed tract densities across the test-retest dataset. (A) Connectivity matrix highlighting the two groups of connections observed: basal ganglia (red) and basal ganglia - thalamus (blue). (B) The relationship between the average tract density of connections and the volume of the terminal nodes is shown in a scatterplot. Tract density was noted to increase with an increase in volume of at least one terminal structure.

structures increased. Performing an ordinary least squares regression, we identified a positive linear relationship between the AFD and the size of the two subcortical structures ($r^2 = 0.210$, $p < 0.05$).

3.3.2.2 Reliability of all intra-hemispheric connections

Using the previously computed connectivity matrices, an average AFD matrix across subjects was created for the test and retest sessions independently (Figure 3.6A). Individual subject matrices, as well as average session matrices were visually inspected, and minimal differences were observed between test and retest sessions. A linear relationship was identified between the AFDs of the test and retest sessions (Supplementary Fig. 3A; $\rho = 0.997$, $p < 0.05$), with greater variability observed between sessions when the AFD was low. Connectivity was further divided by hemisphere (i.e. intra-hemispheric left vs right) and a box plot was created to visually compare test and retest tract densities (Fig. 3.6B). No differences in hemispheric connectivity were observed between test and retest sessions, which was further corroborated after performing a paired t-test between average test and retest AFDs ($t = 1.52$, $\rho = 0.264$ and $t = 1.06$, $\rho = 0.293$ for left and right hemispheres respectively).

To quantify the consistency of AFD between test and retest sessions, we computed the percent change of corresponding subcortical connections between sessions finding on average a percent change of 36% and 32% for the left and right intra-hemispheric AFD respectively (Figure 3.6C). As previously noted, in test-retest pairs where AFD was low, greater variability was observed. Correspondingly, a greater absolute percent change was more likely to be associated with a sparser connection. A Spearman's correlation between the absolute percent change of AFD and the average density across test-retest sessions demonstrated a negative correlation (Supplementary Figure B.3B; $\rho = -0.240$, $p < 0.05$), indicating decreasing percent change as tract density increased. Further, an average intraclass correlation (ICC) of 0.50 and 0.48 was computed for left and right hemispheric connectivity respectively between test and retest AFDs after performing a linear regression to account for brain volume, a covariate identified to demonstrate a significant effect ($F = 7.068$, $p < 0.05$) after performing an ANCOVA (Figure 3.6D). As observed in the tract density, ICC was noted to be greater in connections between basal ganglia structures (ICC = 0.58 and 0.49 for left and right hemispheres respectively) than between the basal ganglia and thalamus (ICC = 0.46 and 0.47 for left and right hemispheres respectively).

Voxel-wise spatial overlap of tracts (calculated via wDSC), was also computed between test-retest pairs as another measure of reliability. We observed an average wDSC of 0.46 and 0.45 for the left and right intra-hemispheric connectivity respectively. We also plotted and performed a Spearman's correlation between wDSC and average AFD across both sessions where wDSC is expected to increase with AFD before plateauing. As expected, we identified a sigmoid relationship (Supplementary Figure B.3C; $\rho = 0.950$, $p < 0.05$) between the two (Figure.

3.6E), with good overlap achieved at a AFD around 2.0 log(AFD) and reaching

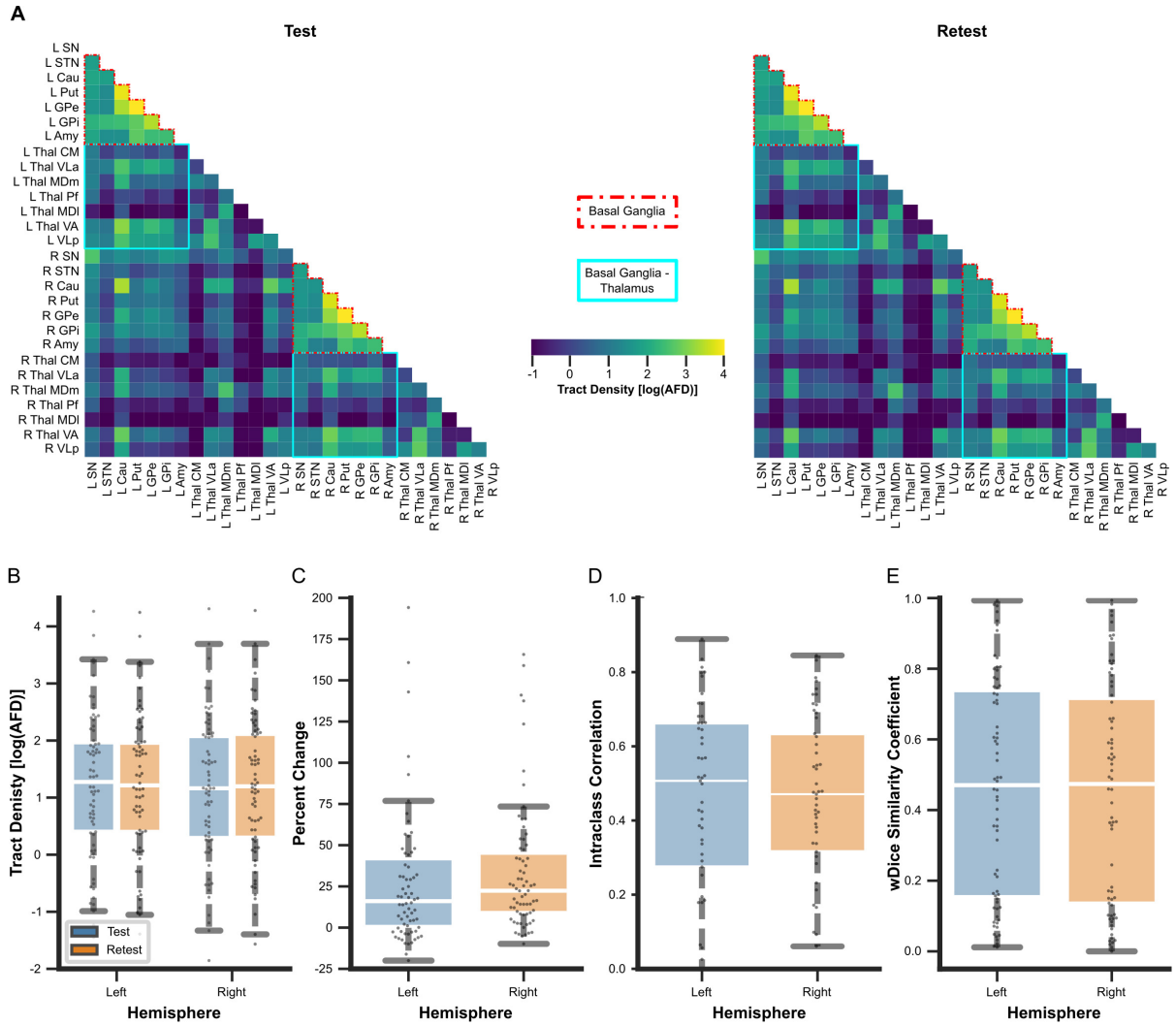

Figure 3.6: (A) Test (left) and retest (right) connectivity matrices are shown, visualizing the log-transformed tract densities between subcortical structures. (B) Log-transformed tract densities of the basal ganglia and between basal ganglia and thalamic connectivity are plotted, separated by hemisphere and session. (C) Percent change of tract densities between test and retest sessions, separated by hemisphere. (D) Intraclass correlations, measuring consistency between sessions, are shown, separated again by hemisphere. (D) wDSC, assessing spatial overlap between sessions, plotted by hemispheric connectivity. For all boxplots, the middle line marks the median metric, while whiskers define the maximum and minimum values of each metric, excluding outliers.

maximum overlap at approximately around 2.5 log(AFD). The overlap remained low while the AFD was less than 0 log(AFD) before slowly increasing until the overlap began to peak at a log-transformed AFD of around 2 log(AFD). As wDSC was highly correlated with AFD, we further separated and evaluated the wDSC to the two previously identified groups. As with observations from known subcortico-subcortical connections, we noted better overlap in

basal ganglia connectivity (average wDSCs = 0.75 and 0.72 for left and right hemispheres respectively) than in connectivity between the basal ganglia and thalamus (average wDSCs = 0.46 and 0.44 in left and right hemispheres respectively). The difference observed between the two groups was also supported with a one-way ANOVA for both the left ($F = 33.53$, $p < 0.05$) and right ($F = 41.64$, $p < 0.05$) hemispheres.

3.3.3 Observations in HCP unrelated dataset

An identical analysis was performed on a subset of the HCP unrelated dataset, where similar observations were noted. An average connectivity matrix was computed and compared against the test-retest dataset, where notably a Pearson's correlation coefficient of 0.99 was demonstrated against both the test ($p < 0.05$) and retest ($p < 0.05$) sessions, indicative of highly similar AFDs with the unrelated dataset. Full details of the results from this validation can be found in the Supplementary Material B.6.

3.4 Discussion

In this study, we evaluated both the feasibility and reliability of identifying the subcortical connectome using *in vivo* tractography data, specifically evaluating the possibility of recapitulating known connections from classic studies of the subcortex. We demonstrated the ability to identify most of the subcortico-subcortical connections (39 out of 46, 85%) described in the literature. Furthermore, we were able to demonstrate test-retest reliability and replicate this analysis on a separate HCP subset, observing near identical results (see Supplementary Data) and again recapitulating most known connections (38 out of 46, 83%). In the following subsections, we compared our observations with the existing literature. Importantly, we also recount the challenges that were faced in studying the subcortical connectome *in vivo* and suggest possible solutions.

3.4.1 Identification of known subcortical connections

Tract-tracing studies have been performed in NHPs to identify and study networks of the subcortical connectome [5,13,151,155,174–176]. A few of these tracts that comprise the networks have also been identified as potentially important neuromodulatory targets [77,78,80,177,178] and may also be critical biomarkers in aging or disease progression [179]. In the present study, we identified and investigated connections of the motor, associative, and limbic networks observing that most known subcortical connections could be recapitulated with a data-driven probabilistic tractography approach. The identified connections were visually inspected to

evaluate the trajectories and their plausibility, comparing our observations with the literature. The ease of identifying trajectories between structures varied, with proximity between terminal structures and density playing a factor. Some notable observed trajectories included connections between the GPi and both the VLa and VLp nuclei of the thalamus, as well as between the STN and both GPe and GPi (Figure 3.3 and Figure 3.4), which have both been well studied. Full details regarding our observations are found in Supplementary Table B.5.

First, focusing on the connection between GPi and VLa/VLp, one plausible trajectory observed was the ansa lenticularis (Figure 3.3). Similar origins of the ansa lenticularis observed in this study from tractography reconstruction have been previously described from tract-tracing studies in NHPs, with similar projections from the GPi to the VLa and VLp [13]. The connection has also been described by [174], noting a trajectory that *"forms a well-defined bundle on the ventral surface of the pallidum..."* curving around the posterior limb of the internal capsule before continuing posteriorly. Along this trajectory, the ansa lenticularis is known to converge with the lenticular fasciculus in the fields of Forel to form the thalamic fasciculus, which continues to VLa and VLp. While we were able to note the termination in the VLa and VLp in our observations, we were unable to delineate the transition from ansa lenticularis to thalamic fasciculus. Further, sparse connections were observed to cross the region of the internal capsule to connect the GPi with VLa and VLp, which may be part of the lenticular fasciculus.

Another notable connection observed was between the STN and globus pallidus, including both the internus (GPi) and externus (GPe) segments (Figure 3.4). Direct trajectories were seen, with noticeable separation differentiating trajectories between the motor, associative, and limbic regions of each structure. Similar separations were also observed in a connectivity-based segmentation by [79], who noted an anteroposterior axis arrangement of the limbic, associative, and sensorimotor regions to the GPi and GPe. We observed sparse connections to the associative region of the GPe, attributed to a combination of the presence of the GPi and the constraints imposed on tracts going through wayward GM structures. Nonetheless, similar termination was not only observed in the previously mentioned study [79], but also in tract-tracing studies, with limbic areas of the STN forming connections with the limbic region of the pallidum and likewise for associative and sensorimotor connections [180]. Other tract-tracing studies have noted similar connections [174–176], suggesting projections from STN to GPe, such as those observed from tractography.

Constraints were imposed to minimize the presence of false positive connections including the use of a convex hull and exclusion of wayward GM structures. While these constraints did not

completely eliminate false positive connections, only a small number were observed relative to the total AFD between subcortical structures (see section 3.3.1 and Supplementary Table B.5). In the context of evaluating trajectories, false positives were identified as streamlines with implausible trajectories (e.g. crossing the mid-sagittal plane or coursing into the CSF) or those part of major white matter connections (e.g. CST). We noted spurious tracts of the CST, the dominant wayward tract traversing the subcortex [181], which was falsely included as streamlines in a number of connections between subcortical structures. The presence of the CST is a result of the dominant diffusion signal, complicating the ability to accurately identify subcortical connections. Consequently, some streamlines predominantly follow the orientation of the dominant diffusion signal until reaching the boundary of the convex hull, where they continue by following its boundary due to the imposed exclusion criteria. Spurious streamlines were also observed to form a loop projecting back towards the cortex after entering the brainstem, where connectivity is expected to traverse from subcortical structures [155]. This is likely caused by a combination of the convex hull exclusion mask and the lack of meeting a termination criteria as the streamline traverses down towards the brainstem. Careful inclusion of additional constraints, such as segmentations from a priori anatomical knowledge, may be useful to aid in the removal of these spurious streamlines. Truncation of a streamline once it reaches the boundary is one possible solution instead of waiting for a termination criteria to be met.

3.4.2 Reliability of the subcortical connectome

Upon visual inspection, the connectivity matrices demonstrated subjectively similar tract densities (AFDs), that is the sum of weighted streamlines that comprise a connection, across subjects and datasets. For a given subject in the test-retest dataset, the tract density was expected and observed to be similar across sessions. This was reinforced quantitatively, where no significant difference was identified between test-retest subjects and an average ICC of 0.49 and 0.48 was observed for left and right hemispheric connectivity respectively, with a noted higher reliability in connections between basal ganglia structures (see section 3.3.1.2). While AFDs were not perfectly identical between sessions, changes in AFD were likely due to differences in the acquired data between sessions. Furthermore, tractography seeding was performed randomly within the brain mask until the desired number of streamlines were met. The SIFT technique employed in the present study helped to minimize the differences between observations by weighting each streamline to best match the underlying diffusion signal [168]. Comparison of AFD reliability with other studies was difficult as different metrics of density are often employed (e.g. raw streamline count) and further compounded by the limited number of sub-

cortical connectome studies [156]. In a comparison with a study of the cortical connectome, AFDs weighted by length were employed to examine the consistency of connections of interest [157]. In their assessment, a similar average ICC of 0.62 was demonstrated, suggesting our findings within the subcortical connectome are comparable.

To validate our findings, we also replicated the analysis on the HCP unrelated dataset, observing similarities between the two datasets from visual inspection and quantitative comparison. We demonstrated high similarity of connectivity matrices across datasets, with a Pearson's correlation coefficient of 0.99 between the averaged connectivity matrix of the unrelated dataset as well as test and retest connectivity matrices. Due to a lack of subcortical connectome reliability studies, direct comparison of our findings was challenging as often different connectomes were investigated, typically focused on cortico-cortical or cortico-subcortical connections. However, in an investigation of cortical connectome reliability across different different resolutions, Pearson's correlation coefficients between 0.724 (high resolution) to 0.958 (low resolution) were computed between connectivity matrices of different subjects [182]. While we acknowledge there were differences in the acquisition and protocol, our observations suggest that the subcortical connectome can be reliably reconstructed to a similar degree as the cortical connectome.

In addition to being able to reliably reconstruct similarly dense connections, it is also important to be able to capture the trajectory of the connections in a reliable manner. To that end, we computed the wDSC to measure the voxel-wise overlap of identified connectivity between test and retest sessions, minimizing the penalty on streamlines further from the tract core. Connections with similar trajectories would traverse the same voxel space and consequently demonstrate higher wDSCs. To our knowledge, while no previous work has evaluated tract overlap of the subcortical connectome, wDSC has been used to demonstrate the reproducibility in the cortical connectome [133, 183]. Our observed wDSC in connectivity between basal ganglia structures was within the reported range (wDSC = 0.71 to 0.82) of four examined cortico-cortical tracts identified using similar techniques [183]. Similarly, wDSC has been employed to examine test-retest reliability of cortico-cortical tractography in the Parkinson's Progression Markers Initiative dataset, where a wDSC of 0.72 was identified as a threshold for good overlap in their study [133]. The same study also examined reliability of cortico-subcortical connections using an ROI defining a general cortical region (e.g. sensorimotor cortex, associative cortex, limbic cortex) to an ROI defining a subcortical structure (e.g. caudate, putamen, thalamus), where poor reliability of cortico-subcortical connectivity was noted. The poor reliability was attributed to a combination of the quality of atlas used to define ROIs, partial volume effects, motion and the low resolution of the data, as well as the difficulty of performing tractography

to the subcortical brain regions where structures are generally smaller [133].

Overall, we demonstrated that the methods employed in the present study can produce subcortical connectomes with comparable reliability to those that have been used to study cortico-cortical and cortico-subcortical connectomes. Although we observed worse reliability in connectivity between the basal ganglia and thalamus, we believe this is primarily attributed to the sparse connections resulting from imposed GM constraints. Further some nuclei of the thalamus were more difficult to reach, with other nuclei present along the expected trajectory, while others were smaller in size. Some changes to the tractography algorithm (e.g. angle, maximum streamline length, etc.) or further optimization of constraints may be required to improve the overall connectivity with the thalamus. In subsequent work, the described framework can be leveraged to evaluate the impact of modifications to the original algorithm and their impact on the resultant tractography.

3.4.3 Clinical significance

The ability to reliably identify subcortical connections has important clinical implications for diagnosis and treatment planning, potentially improving targeting of specific subcortical structures. Previous studies have examined neuromodulation of specific subcortical connections [77, 78]. Accurate and robust identification of the subcortical connectome can facilitate and enhance the ability to study pathologic changes due to disease. Furthermore, the ability to reliably identify subcortical connections also increases the likelihood of avoiding collateral connections, which can result in undesirable side effects. One consideration for clinical translation is the acquisition protocol and scan time. While clinical data is typically collected at lower angular and spatial resolutions than that of the data in this study, recent advancements in parallel imaging will help to make higher quality diffusion MRI feasible in a clinically-feasible time frame.

3.4.4 Implementation choices for the tractography algorithm

Tractography involves choices that need to be made at each step of the workflow that affect downstream steps and analysis. One such decision was the choice of segmentations used to identify connectivity of the subcortical connectome. As we were interested in the connectivity between specific subcortical structures, we pooled together existing atlas-based segmentations [160, 163, 184] to serve as terminal ROIs and to minimize variability that may be introduced by manual segmentation. Choice of atlas-based segmentation was influenced by convenience and familiarity, with a focus on tools that are openly available. The thalamus la-

bels used are readily available through a commonly used neuroimaging software package (i.e. FreeSurfer; [160]). Openly available segmentations of other subcortical structures were propagated from a single high-resolution template [163]. Different approaches to identifying ROIs can lead to varying shapes and boundaries, which would have some downstream effects on identified connectivity. For example, in histology-based segmentations, ROIs may be defined by the underlying nuclei, whereas in structural connectivity-based segmentations, ROIs may be related to regional connectivity. Furthermore, certain structures, including the caudate or putamen can also be subdivided into different components [185–187], similar to the thalamus. With many segmentation schemes readily available and multiple considerations to contemplate, it is important to note that choice of segmentation is often dependent on the aims of the specific study [188].

Segmentation accuracy is also important for capturing the true underlying subcortical structure, with size influencing the reconstructed connectivity as has been previously noted [41] and also observed in this study. An ROI larger than the structure, especially in the small subcortical region, may overlap with other structures or extend into the WM or CSF. On the other hand, an ROI smaller than the structure may exclude connectivity that does not reach the boundaries, although some of this is alleviated by using the radial search strategy employed. Due to the relationship between ROI size and tract density (see Figure 3.5B), the ability to identify connections in small structures is challenging and some expected connections may remain unidentified. Nonetheless, the segmentations present incorporated data from histology and largely reflect the underlying anatomy.

We chose to include a GM exclusion criteria in our tractography algorithm, removing connectivity passing through other subcortical structures along its trajectory. This choice was made in part to limit the number of false positives passing through GM structures where multiple diffusion orientations and low anisotropy are often observed that result in a significant increase in spurious streamlines. However, it is known that subcortical connections can pass through other structures [175, 176]. As a result of this constraint, we noticed sparse connectivity between regions where another GM structure is along the expected trajectory. One possible solution is to make use of anatomical priors to allow for the traversal of GM structures in cases where connections are known to pass through (e.g. allowing connections to pass through GPi when connecting GPe and STN). Such a solution has been previously implemented for cortico-cortical connectivity in the White Matter Query Language, where predefined regions (inclusion and exclusion) and endpoint ROIs are used to identify connections of interest [189]. To implement this for the subcortical connectome would require detailed curation of anatom-

ical knowledge to identify the necessary inclusion and exclusion wayward ROIs required in addition to the terminal regions. Unfortunately, even without explicit exclusion of wayward GM ROIs, the ability for tracts to pass through GM will be challenging due to the reduced anisotropy in GM (e.g. in the pallidum).

In a similar manner, the inclusion of WM priors as wayward ROIs may improve anatomical accuracy. With a data-driven approach to identifying the subcortical connectome, we had observed the presence of major tracts (e.g. CST), spurious streamlines, and in some instances, multiple trajectories between two subcortical structures. By using a WM prior, trajectories from major tracts and spurious streamlines could be filtered, while individual trajectories can be isolated. In a previous study of tractography reproducibility, a suggestion was made to include the use of anatomical priors as guidance to improve identification of connectivity [54]. One such possibility is to leverage the segmentations of subcortical connections surrounding the zona incerta that have been previously identified with high resolution, *in vivo* anatomical MRI [184] to help differentiate observed connections from a data-driven approach. Additionally, drawing anatomical knowledge from NHP and post-mortem studies can help to establish priors that can improve anatomical accuracy by minimizing the number of false positive connections and help to discern trajectories. However, optimizing the use of anatomical priors remains an open challenge even for well understood tracts like the CST [138, 158]. Ultimately, moving forward, our described framework would allow for the evaluation of different implementation choices and their impact on both identification and reliability of mapping the subcortical connectome.

3.4.5 Application of connectivity thresholds

As previously described, defining a threshold is a non-trivial task (see section 3.2.8). While there are different methods for defining a threshold, including selection of an arbitrary value or by sweeping through a range of values, the present study uses a test-retest technique to determine an appropriate threshold value. Such an approach is limited to test-retest datasets. However, the threshold can be applied to other datasets processed with the same techniques, as was performed on the HCP unrelated dataset. To apply the threshold to other datasets, an analysis should first be performed to assess whether the defined threshold is appropriate.

3.4.6 Limitations

Several limitations are worth noting beyond those related to choices made in the implementation of the trajectory algorithm (see previous section). Validation of tractography identi-

fied connections *in vivo* is a known challenge, given the limited ability to compare to ground truth trajectories, which have been conventionally identified using tract-tracing in experimental animals. While the most accurate comparisons would be performed between tract-tracing and tractography on the same brain, this is not feasible in humans. Fortunately, connections between regions are highly similar across different primates [190]. In the current study, we limited our investigation to known connections between ROIs of the basal ganglia and the thalamus in order to compare our observations with previously described trajectories. As a result, we did not explore the complete network circuitry to other regions of the brain (e.g. brainstem, cerebellum, cortex, etc). Some of these unexplored regions contain important nodes, such as connectivity with the hypothalamus [155] and pedunculopontine nucleus of the brainstem [151]. Other connections of interest, including between the sensory thalamus (e.g. medial and lateral geniculate nuclei) and the striatum, have been previously examined in experimental animals [191]. Future work should explore the network circuitry more comprehensively, which should be increasingly feasible with increasing availability of brain atlases.

3.5 Conclusion

In this study, we demonstrated that identifying the subcortical connectome using a data-driven probabilistic approach with *in vivo* tractography was both feasible and reliable, with a particular focus on the assessment of known connections that have been previously described. Quantitative evaluation of the subcortical connections demonstrated similar tract densities and overlap comparable to what has been shown in existing studies focussed on cortico-cortical and cortico-subcortical networks. Performing this assessment also highlighted areas requiring improvement to address the challenges of tractography in the subcortex. The methods used in this study can serve as a framework for evaluating the impact of modifications to the tractography workflow, with the goal of increasingly accurate and reliable mapping of the subcortical connectome.

Chapter 4

Aberrant frontal lobe "U"-shaped association fibres in first-episode schizophrenia: A 7-Tesla diffusion imaging study

This chapter is based on the following manuscript:

- Kai, J., MacKinley, M., Khan, A.R., Palaniyappan, L. (Submitted). Aberrant frontal lobe "U"-shaped association fibres in first-episode schizophrenia: A 7-Tesla diffusion imaging study.

4.1 Introduction

Schizophrenia is a neuropsychiatric disorder with a diverse range of symptoms which can present differently amongst individuals [82]. Characterization of symptoms can be largely defined into three groups: (1) positive / psychotic (altered perception; eg. delusions), (2) negative / deficit (reduced or lack of normal function; eg. loss of motivation), or (3) cognitive (eg. impaired attention or memory) [84, 141]. First proposed by Wernicke, it has been suggested that psychosis, commonly experienced by those diagnosed with schizophrenia, may arise from abnormal interactions resulting from disrupted brain connectivity [81–83], specifically between the prefrontal cortex and other brain regions [192]. While many regions of the brain may be associated with schizophrenia, the frontal lobe is one of the most studied cortical regions with findings including physiological, morphological, and metabolic changes [193].

Diffusion tensor imaging (DTI), a model commonly derived from diffusion magnetic resonance imaging (dMRI), can be used to evaluate quantitative changes in white matter and is sensitive to changes to the microstructural environment [32]. In previous studies of psychosis, DTI has been mostly applied to study major white matter tracts connecting distant brain regions. The Schizophrenia Working Group of the Enhancing Neuroimaging Genetics through Meta-Analysis consortium (ENIGMA-Schizophrenia) studied DTI-derived measures in major white matter tracts, comparing differences between healthy controls and participants with schizophrenia [85]. In this study comparing over 4000 individuals, WM changes in patients with schizophrenia were found throughout the brain [85]. Regional abnormalities in white matter has also been reported from one meta-analysis of DTI studies in schizophrenia [194], while a recent meta-analysis noted more widespread abnormalities of white matter, along with significant associations with age, duration of illness, and gender [86].

Recently, studies have also used dMRI to investigate short-ranged association tracts, also referred to as "U"-shaped tracts (or "U"-fibres), which reside just below the cortical surface and comprises part of the superficial white matter together with intracortical axons [11, 195, 196] in neurological and psychiatric disorders. Functionally, the "U"-fibres have been proposed to play an important role in cognitive function [8]. Structurally, these tracts follow a "U"-shaped

trajectory, coursing underneath the sulcus and connecting nearby gyri. Developmentally, "U"-fibres are some of the last to reach full maturation, often developing late into adulthood, with a thinner myelin sheath relative to the brain's deep white matter [10]. Consequently, these tracts offer less protection and may be vulnerable to aberrations during development [10]. In particular, if a disorder involves generalized reduction in myelin content, then "U"-fibres may be one of the earliest to be affected, given their sparse myelination with one oligodendrocyte wrapping many "U"-fibres axon segments [197, 198]. One of the challenges of examining the "U"-fibre tracts arise from the morphological differences between individuals [199]. As the tracts follow closely with the gyrification of an individual, morphological differences across individuals can introduce varying spatial arrangements of the "U"-fibres, complicating the ability to identify corresponding tracts across individuals. Previous studies have used clustering methods to first create a template of the most common "U"-fibres (e.g. those that are present in the majority of the study sample) from a sample of healthy individuals [56, 66, 101]. The created template can then be applied to identify the same "U"-fibres in other individuals, enabling the evaluation of similar short-ranged tracts.

While there has been an extensive number of studies investigating schizophrenia and associated changes using DTI, in particular the major white matter pathways, assessment of the "U"-fibres is still in its early days. In this work, we utilized a template of "U"-shaped tracts we previously created [200] to identify and examine tracts present in the majority of patients with first-episode schizophrenia (FES) with a focus on those localized to the brain's frontal lobe. We assessed differences in tract density, changes both along the length and in the entirety of the identified U-fibre tract, evaluated relationships with clinical symptoms, and identified associated networks with aberrant "U"-fibres. Due to the vulnerability of "U"-fibres from the late maturation, we hypothesized that untreated patients with FES would exhibit compromised frontal "U"-fibres in the form of reduced integrity that are associated with symptom severity at the time of first presentation. Such aberrations may be more sensitive to localized changes, providing key insights into how the "U"-fibres are affected along its trajectory in FES. We also expected the affected "U"-fibres to be restricted to key functional networks relevant for cognitive control function (see [201]) at such an early stage of psychosis, rather than affecting all of the frontal lobe. Finally, given the mounting evidence supporting a role for oligodendrocyte dysfunction in schizophrenia (see [202]), we expected the "U"-fibre aberration to demonstrate changes to diffusivity measures related to tissue microstructure which is affected due to myelin related abnormalities.

4.2 Materials and methods

All participants provided written, informed consent according to the guidelines provided by the Human Research Ethics Board for Health Sciences at Western University, London, Ontario.

4.2.1 Participants

Untreated patients with FES (n=53; 44M/9F, ages 16-39) were recruited from referrals received by the Prevention and Early Intervention Psychosis Program (PEPP) at the London Health Sciences Center (LHSC) with an inclusion criteria of lifetime antipsychotic exposure of less than 14 days. Participants with suspected drug-induced psychosis were excluded from the study. FES participants were diagnosed with schizophrenia according to the DSM-5 criteria, using the consensus procedure described by Leckman and the Structured Clinical Interview for DSM-5 to confirm diagnosis 6 months after the first presentation [203]. We used a consecutive referral strategy for patient recruitment whereby all patients referred to the only first episode clinic in the catchment area between April 2017 and June 2019 were approached, if deemed to have the capacity to consent for the study by the clinicians. Healthy controls (n=31; 19M/12F, ages 16-29) were recruited through posters and word-of-mouth advertising, with no personal or family history of mental illness or psychotic disorders, and no current use of medications, as well as the same criteria as patients (e.g. no known neurological disorders). The healthy controls were matched for age and parental socio-economic status with the patient group. All participants were screened to exclude significant head injuries, major medical illness, or MRI contraindications. Table 4.1 describes the demographics and clinical characteristics for study participants. Participants for this study underwent a clinical assessment and imaging on the same day. Part of this sample has been reported in our prior studies [203–205].

4.2.2 Clinical measures

A clinical assessment was performed by a research psychiatrist (for patients) or trained rater (for healthy controls) using the clinical battery that assessed for patient symptom severity, substance use and to confirm healthy controls had no history of psychotic illness or neurological disorder. Symptoms of psychosis were assessed using the Positive and Negative Syndrome Scale - 8 Items (PANSS-8; [206]). The abbreviated version of the assessment has been shown to be highly consistent and correlated with the full PANSS assessment consisting of 30 items [206]. Items within the PANSS-8 are scored from 1 (absent) to 7 (extreme) to evaluate both positive (P1 - delusions, P2 - conceptual disorganization, P3 - hallucinations) and negative (N1 - blunted affect, N4 - passive social withdrawal, N6 - lack of spontaneity and flow of

Table 4.1: Demographic and clinical characteristics of healthy controls and patients with first-episode schizophrenia.

Variable	Controls (n=31)	Patients (n=53)	Controls vs Patients
	Demographic		
Sex (M/F)	19/12	44/10	$\chi^2 = 2.47$, $p = 0.17$
Age [Mean (SD)]	21.55 (3.50)	23.06 (4.76)	$t = -1.80$, $p = 0.077$
	Clinical		
DUP [Mean (SD)]	N/A	8.20 (14.70)	
Antipsychotic Defined Daily Dose (cumulative*)	N/A	1.99 (3.10)	
SOFAS [Mean (SD)]	83.11 (4.20)	39.22 (12.19)	$t = 16.4$, $p < 0.001$
PANSS-8 Total [Mean (SD)]	8.0 (0.0)	26.39 (7.12)	$t = -13.0$, $p < 0.001$
PANSS-8 Positive [Mean (SD)]	3.0 (0.0)	11.81 (4.10)	$t = -14.1$, $p < 0.001$
PANSS-8 Negative [Mean (SD)]	3.0 (0.0)	7.36 (4.78)	$t = -5.50$, $p < 0.001$
CGI-S [Mean (SD)]	1.0 (0.0)	5.22 (1.01)	$t = -20.6$, $p < 0.001$
	Cognitive		
Trail Making Time (s) [Mean (SD)]	52.43 (15.23)	77.73 (34.82)	$t = -2.69$, $p = 0.013$
Trail Making Errors [Mean (SD)]	0.48 (0.85)	0.61 (1.1)	$t = -0.47$, $p = 0.65$
Category Fluency	23.74 (7.65)	17.46 (4.33)	$t = 3.48$, $p = 0.0017$

p-values for differences between groups were calculated using chi-square for categorical variables and independent t tests for continuous variables.

SD: standard deviation; DUP: Duration of Untreated Psychosis (in months); SOFAS: Social and Occupational Functioning Assessment Scale; PANSS-8: Positive and Negative Syndrome Scale - 8 Item Scale; PANSS-8 Positive: PANSS-8 total score for positive symptoms; PANSS-8 Negative: PANSS-8 total score for negative symptoms; CGI-S: Clinical Global Impressions Scale - Severity; *total lifetime dose exposure, calculated as Daily Defined Dose x days of exposure

conversation) symptoms. Additionally, the severity of the illness was assessed using a subscale of the Clinical Global Impression Scale (CGI-S) [207]. The subscale is scored between 1 (normal, not ill) to 7 (most severely ill). Furthermore, the Social and Occupational Functioning Assessment Scale (SOFAS) was conducted at the time of first presentation [208] independent of symptom severity. SOFAS is a single-item scale scored between 1 (persistent inability to maintain minimum functioning without external support) to 100 (superior functioning in a wide range of activities). Lastly, the duration of untreated psychosis (DUP) and approximate age of onset was recorded.

4.2.3 Cognitive measures

Cognitive tests were also performed to assess different cognitive abilities for each study participant. Trail Making Test (TMT-B) was conducted, testing for the participants ability for planning, self-control, and attention. In this task, participants are asked to draw a line following a number-to-letter pattern (e.g. 1 to A, 2 to B, etc.), recording the time to completion and number of errors made during the uninterrupted task. In addition, a category fluency test was performed, testing for semantic knowledge, retrieval ability, and executive function. For this test, study participants were asked to list as many items as they could think of within a category (animals) in 60 seconds. The number of items listed were recorded and corrected for any repeat or non-categorical items.

4.2.4 Imaging

Imaging was performed for all study participants on a 7-Tesla (7T) Siemens Magnetom head-only MRI system at Robarts Research Institute in London, Canada. Anatomical data was collected using a MP2RAGE sequence [209] with the following scanning parameters: repetition time/echo time (TR/TE) = 6000 / 2.83 ms; inversion time 1 (TI_1) = 800ms; inversion time 2 (TI_2) = 2700ms; 0.75 mm isotropic resolution; field of view (FOV) = $156mm \times 240mm \times 240mm$. Diffusion data was acquired twice with opposite phase encoding directions using the following scanning parameters: TR/TE = 5100 / 50.2 ms; 2.00 mm isotropic resolution; FOV = $208mm \times 208mm \times 144mm$; b-value = 1000 s/mm^2 (64 directions) with 2 b-value = 0 s/mm^2 (non-diffusion weighted) acquisitions; multiband acceleration factor of 2.

4.2.5 Processing

Image data processing was performed in containerized computing environments on high performance compute clusters. The following subsections detail the processing steps performed. An overview of the general workflow performed is shown in Figure 4.1. Briefly, data collected using an MRI was used to identify and assess "U"-fibres of the frontal lobe using tractography. Analysis included assessment of both tract density and along-tract differences from DTI derived measures, as well as evaluation of the relationship of clinical measures and DTI derived measures. Furthermore, affected tracts were mapped to the associated anatomical regions and functional networks.

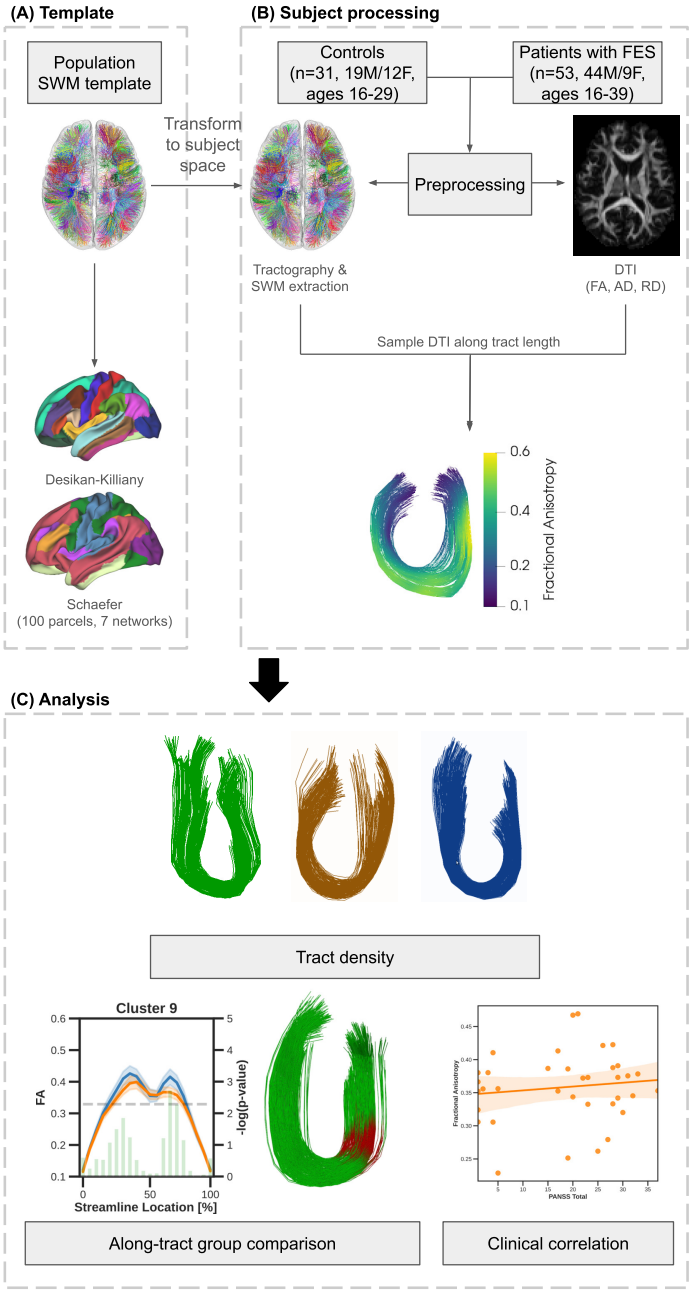

Figure 4.1: Overview of processing and analysis workflow. (A) A population SWM template was registered to each subject's native space to aid identification of corresponding tracts across subjects. "U"-shaped tracts constrained to the frontal lobe was mapped to anatomical (Desikan-Killiany) and functional (Schaefer - 100 parcels, 7 networks) parcellations. (B) Data collected from healthy controls and patients with FES were preprocessed before performing tractography to identify frontal lobe SWM and deriving quantitative maps from DTI. Derived metrics were mapped along the length of the identified frontal lobe SWM. (C) Analysis was performed on clusters that were present in 70% of each group, evaluating for tract density and quantitative differences. Correlations between clinical measures and derived metrics was performed to identify relationships in patients.

4.2.5.1 Anatomical T1-weighted

Data was preprocessed by first applying a correction to unwarp distorted anatomical volumes due to gradient field inhomogeneities (gradient non-linearity correction). Data was preprocessed by first applying a correction to unwarp distorted anatomical volumes due to gradient field inhomogeneities (gradient non-linearity correction). This was performed using a modified version of publicly available code[1] to work with proprietary scanner-specific file. Following gradient non-linearity correction, fMRIprep (v1.5.4) was applied to each subject's anatomical data [210, 211] for further preprocessing. The preprocessing includes the correction for intensity non-uniformity, and skull stripping. As part of the fMRIprep pipeline, cortical segmentations were derived with FreeSurfer [212].

4.2.5.2 Diffusion MRI (dMRI)

First, distortion correction due to gradient field inhomogeneities was performed using a modified version of publicly available code with a proprietary scanner-specific file, similar to the anatomical preprocessing step. Then, dMRI data was preprocessed with prepdwi [113],
a pipeline developed in-house consisting of principal component analysis based denoising [114, 115] and minimization of Gibbs ringing effects [116] followed by correcting for distortions induced by susceptibility, eddy currents, and subject motion through application of FSL's topup [117, 118] and eddy [119]. The preprocessed dMRI data was rigidly registered with the subject's anatomical data using Niftyreg[2] as part of the in-house preprocessing pipeline. Using Mrtrix3, diffusion tensors were estimated from the preprocessed dMRI data and fractional anisotropy (FA), radial diffusivity (RD), axial diffusivity (AxD), and mean diffusivity (MD) maps were derived using an iteratively reweighted linear least squares estimator [125].

4.2.5.3 Tractography

Following dMRI preprocessing, Mrtrix3 [105] was used to further process the data for tractography. First, individual subject response functions were estimated using the Dhollander algorithm [120] and group average response functions were estimated from healthy controls. Individual subject fibre orientation distribution (FOD) maps were computed from the average response functions using the multi-shell, multi-tissue algorithm [121] while excluding the GM response function for single-shell data, enabling comparison of corresponding tracts between individuals [166]. By excluding the GM response function, the multi-shell, mutli-tissue algorithm could still be used for single-shell data in order to suppress signal from the cerebrospinal

[1] https://www.github.com/kaitj/gradunwarp
[2] http://cmictig.cs.ucl.ac.uk/wiki/index.php/NiftyReg

fluid. A population template previously created from unrelated subjects, including FOD maps and labeled "U"-fibre tractography [200] was used to aid identification of "U"-shaped tracts. To do so, individual subject FOD maps were first registered to the population FOD template using a multi-resolution pyramid structure to determine transformations between the template and subject spaces. Using the transformation from the template to the subject's native space, the population template was transformed to identify and establish correspondence of tracts between subjects.

Whole-brain probabilistic tractography was performed for each subject using a tensor-based algorithm [44] identifying streamlines of all tracts, including "U"-fibres and other major tracts, again using the Mrtrix3 software suite [105]). Seeding of the tractography was performed at random within the brain until a target of 10,000,000 streamlines had been selected. Following creation of the tractogram from the tensor-based algorithm, streamlines were filtered via spherical-deconvolution informed filtering (SIFT) to match WM FOD amplitudes until a target of 1,000,000 streamlines remained for each subject [124].

Short-ranged, U-shaped streamlines were identified from whole-brain tractography using established parameters for determining a "U"-shaped trajectory (streamline length between 20*mm* and 80*mm* and the distance between streamline endpoints was approximately $1/3$ of the streamline length) [12]. Streamlines with "U"-shaped trajectories were clustered into tracts through label propagation from the previously labeled template with streamlines assigned to the cluster of the most similar template tract. Additionally, streamlines were mapped to the nearest Freesurfer-based lobar parcellation within a 4mm radius of the terminal ends. For tracts with streamlines connecting more than two nodes, tracts were assigned to the two nodes where the majority of the streamlines terminated. From here, "U"-fibres residing in the frontal lobe were identified for further analysis. Moreover, quantitative values derived from DTI were mapped to 20 equidistant samples on each streamline of frontal lobe "U"-shaped tracts and averaged to create a mean along-tract measurement for tractometry analysis. Furthermore, a single mean quantitative measurement was also computed for each identified tract by averaging the sampled measurements in associated streamlines to evaluate overall tract changes.

4.2.5.4 Surface and parcellation mapping

Each template "U"-shaped tract was mapped to a standard symmetric brain surface with approximately 32k vertices (fs_LR32k). First, the centroid of each terminal end was identified and the Euclidean distance to the surface vertices was computed. A labeled surface map was created by assigning the label of the nearest tract to each vertex. To identify associated brain

regions, anatomical and functional atlases were used. Specifically, the Desikan-Killiany [213] and the Schaefer atlases ([214]; 100 parcellations, 7 networks) were used to determine the associated anatomical parcels and functional networks respectively for each identified "U"-shaped tract.

4.2.6 Analysis

For analysis, identified frontal lobe tracts were discarded if fewer than 5 streamlines were present. Furthermore, individual variability may reduce the capability of identifying corresponding "U"-fibres across study participants from the previously created template. As such, tracts were only considered for analysis if they were determined to be present in at least 70% of the healthy control and patient groups respectively.

4.2.6.1 Tract Density

Individual streamlines were extracted and summed to determine the tract density of identified tracts meeting analysis criteria. A Bartlett test was first performed to determine whether the variance of the two groups were equal, followed by a two-sided, Welch's t-test [215] to test for differences in density of individual tracts between groups (due to unequal variance between healthy controls and patients). False discovery rate correction was performed with the Benjamini-Hochberg procedure for multiple comparisons [137]. Furthermore, a Welch's t-test was performed to compare the total density comprising frontal lobe "U"-fibres.

4.2.6.2 Microstructural changes

Measures of FA, RD, AxD, and MD sampled equidistantly along the length of tract were regressed to control for age and sex covariates prior to analysis and a Welch's t-test was performed to compare measured samples between groups. To account for the numerous comparisons carried out between samples, as well as across tracts, a permutation-based multiple comparison correction approach with 10,000 repetitions was applied to adjust the significance threshold [216], similar to [217] and [218]. Using this procedure, an adjusted threshold of $p < 0.005$ was determined to be significant for along-tract measures in this study.

4.2.6.3 Relationships with clinical and cognitive measures

An average quantitative measure (i.e., mean FA, RD, AxD, MD) was computed from the segments identified with differences along the length of the tract between the two groups and the relationships with included clinical measures of PANSS-8, SOFAS, DUP, CGI-S, and age of

onset were evaluated using Pearson's correlation in the patient cohort. Additionally, relationships with cognitive measures of TMT-B completion time, error rate, and category fluency score were also evaluated using Pearson's correlations in the patient cohort. As with tract density, false discovery rate correction was performed using the Benjamini-Hochberg procedure to correct for multiple comparisons.

4.3 Results

Comparing demographic and clinical measures between healthy controls and patients with FES, no statistically significant differences were observed for sex or age. However, within the patient group, males were over-represented (χ^2=15.364, $p < 0.001$). Patients were also observed to demonstrate a statistically significant difference in SOFAS scores (t=16.4, $p < 0.001$), PANSS-8 Total (t=-13.0, $p < 0.001$), PANSS-8 Positive (t=-14.1, $p < 0.001$), PANSS-8 Negative (t=5.50, $p < 0.001$), and CGI-S (t=-20.6, $p < 0.001$) scores. Differences were also observed for cognitive measures of trail making completion time (t=-2.69, $p < 0.05$) and category fluency (t=3.48, $p < 0.05$).

4.3.1 Tract density of frontal lobe "U"-fibres

After applying the previously mentioned constraints ("U"-shaped trajectory residing within the frontal lobe; see section 4.2.5.3), 63 out of 122 frontal lobe "U"-shaped tracts across both left and right hemispheres were retained. Average streamline counts from these tracts throughout the frontal lobe were assessed between controls and patients with FES. Performing a Welch's t-test yielded no significant differences between the two groups following correction for multiple comparisons, indicating that in schizophrenia, the density (in this case the overall volume inferred from diffusion-based streamline count) was unaffected in frontal "U"-fibres. Fig. 4.2 exhibits the assessed tract densities described (log-transformed for visualization).

4.3.2 Affected "U"-fibres and associated structural and functional parcellations

From the frontal lobe "U"-fibres that met the defined analysis criteria, tractometry analysis identified 3 tracts (2 in the left hemisphere, 1 in the right hemisphere) with significant along-tract DTI derived differences after performing a permutation-based multiple comparisons correction. All 3 tracts (Fig. 4.3) demonstrated a significant decrease in FA ($p < 0.005$), together

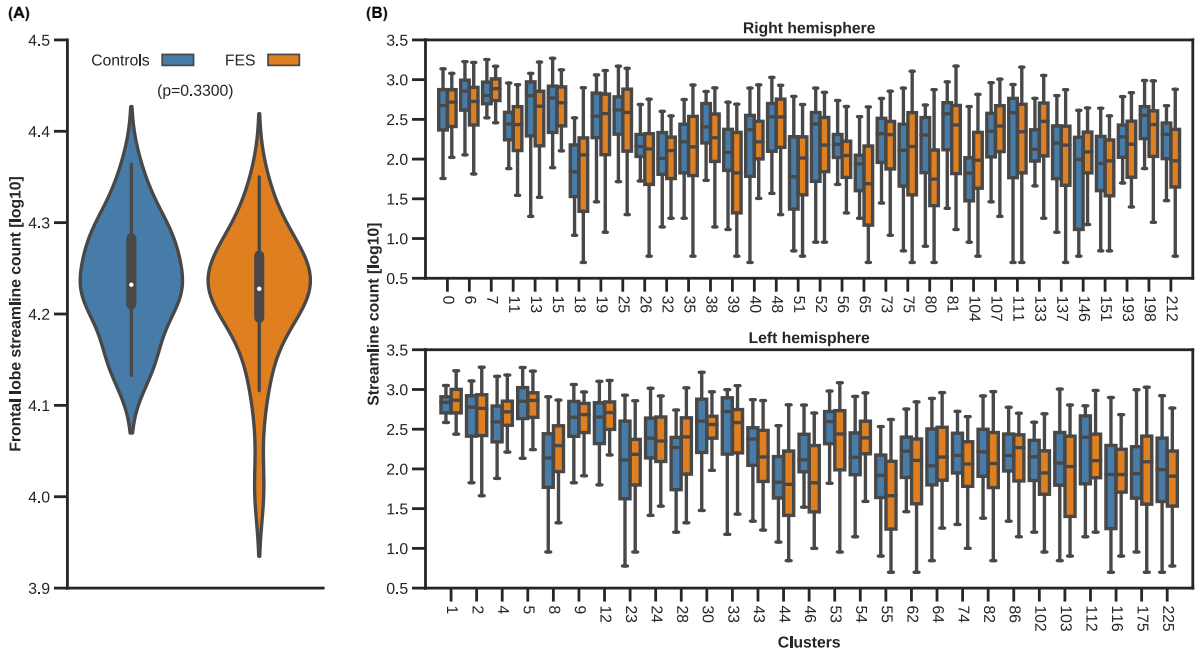

Figure 4.2: (A) Log-transformed distribution of frontal lobe SWM streamline counts from tracts present in 70% of healthy controls and patients with FES. No differences were observed. (B) Log-transformed distributions of individual frontal lobe "U"-shaped tracts in the right (top) and left (bottom) hemispheres for controls and patients. Following correction for false discovery (via Benjamini-Hochberg), no differences were observed.

with a significant increase in RD along similar segments ($p < 0.005$) in patients with FES, indicating localized deficits in regards to tissue microstructure. More details related to these affected segments can be found in Supplementary Figure C.1. and Supplementary Table C.1. The affected segments were detected adjacent to the midpoint of the tract, nearest to the sulci. A slight increase in MD was also observed along similar segments in patients with FES, however these observations were not determined to be statistically significant. No significant differences in AxD were identified for any analyzed tracts.

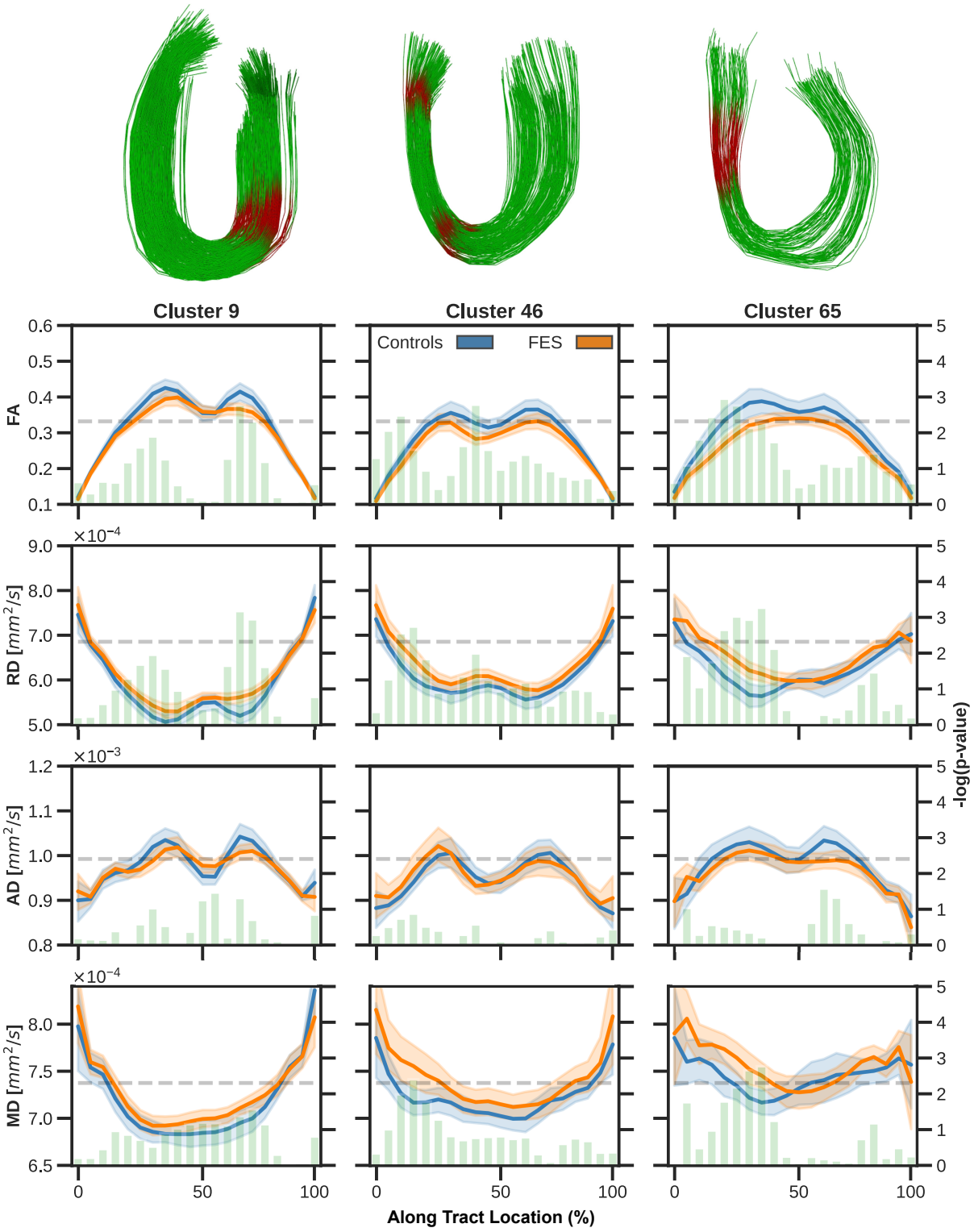

Figure 4.3: DTI-derived measures (top: FA, middle-top: RD, middle-bottom: AxD, bottom: MD) mapped along frontal lobe tracts of controls (blue) and patients (orange). Segments with observed differences between groups are highlighted (in red). 3 tracts were identified (2 in left hemisphere, 1 in right hemisphere) with increased FA and decreased RD.

Each affected tract was also mapped (Fig. 4.4) to both anatomical parcellations (from the

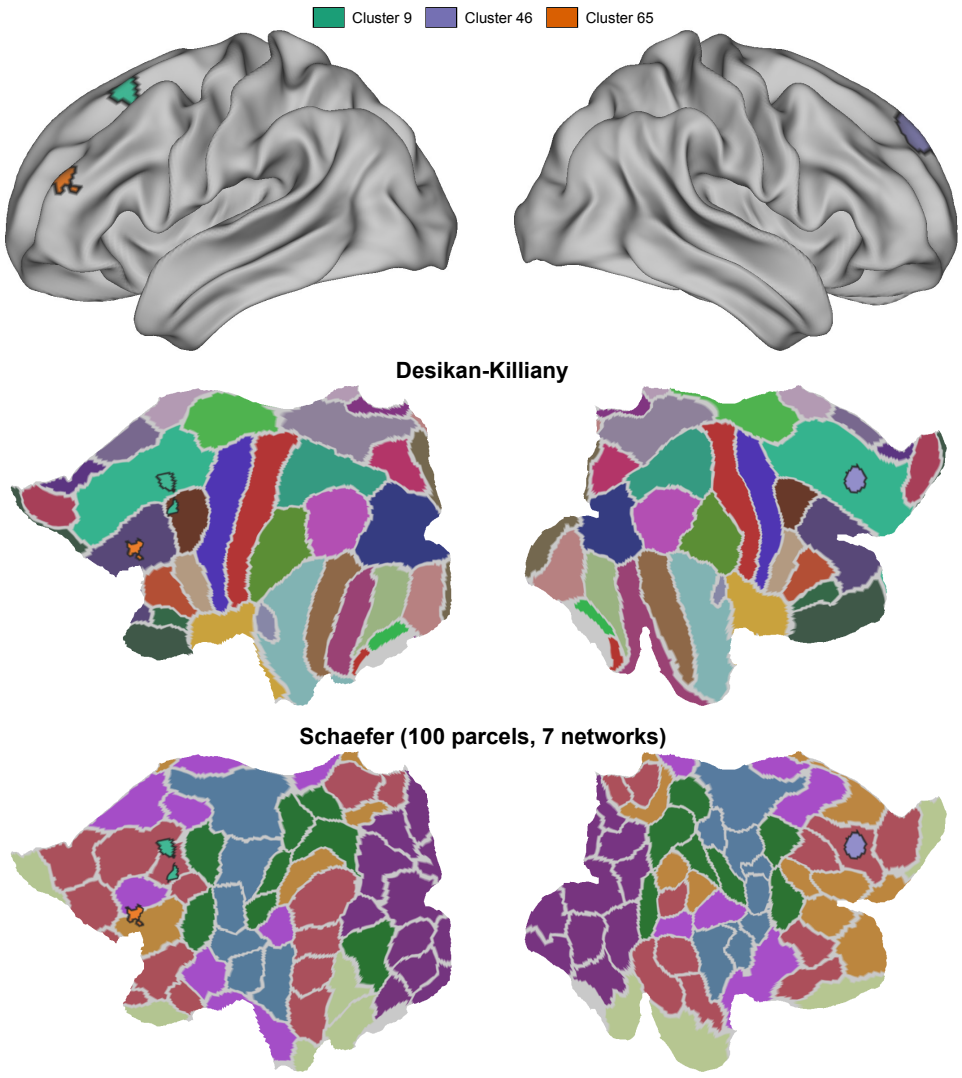

Figure 4.4: Frontal lobe SWM mapped to the fs_LR32k white matter surface (top). Identified frontal lobes with decreased FA and increased RD are outlined in black on flat maps of anatomical (middle; Desikan-Killiany) and functional (bottom; Schaeffer) parcellations. The "U"-shaped tracts were associated with default mode, frontoparietal, and ventral attention functional networks

Desikan-Killiany atlas) and functional network parcellations (from the Schaefer atlas containing 7 networks, 100 parcels). Tract 9, one of the identified affected frontal lobe tracts in the left hemisphere, was found to connect the superior frontal and caudal middle frontal brain parcels and associated with the default mode (DMN) functional network. The other identified frontal lobe connection of the left hemisphere, Tract 46, resided entirely within the caudal middle frontal brain parcel, interconnecting with the frontoparietal (FPN) and ventral attention (VAN) functional networks. Lastly, Tract 65 was identified to reside within the superior frontal parcel of the right hemisphere, and also associated with the DMN.

4.3.3 Correlations between DTI and clinical measures

Segments along the tract where differences were observed for each tract were averaged to obtain a single measure and correlated with clinical measures (e.g. PANSS-8, CGI-S, SOFAS, DUP, approximate age of onset). Table 4.2 outlines the correlations of measures from affected tract segments and the clinical measures. No significant correlations were identified between DTI measures (FA, RD, MD) and clinical measures. Correlations were not performed against MD for tract 9 or AxD as there were no significant segments identified.

4.3.4 Correlations between DTI and cognitive measures

Similar to 4.3.3, correlations were performed between an average of the aberrant segments and cognitive measures (e.g. trail making completion time, trail making errors, category fluency). Correlations between measures from affected tract segments and cognitive measures can be found in Supplementary Table C.2. A significant correlation was identified between the number of errors made during the trail making task and FA from tract 46 prior to multiple comparisons correction. No other significant correlations were identified both prior to and after multiple comparisons correction.

Table 4.2: Correlations between DTI-derived measures (from aberrant segments along-tract) and clinical charactierstics in patients with FES. MD of tract 9 and AxD not included (no identified aberrant segments)

Variable	Tract 9 FA			RD			MD		
	r	$p_{uncorrected}$	$p_{corrected}$	r	$p_{uncorrected}$	$p_{corrected}$	r	$p_{uncorrected}$	$p_{corrected}$
Age	0.234	0.307	0.911	-0.327	0.148	0.911			
CGI-S	-0.141	0.543	0.911	0.237	0.302	0.949			
DUP	0.185	0.422	0.911	-0.190	0.409	0.911			
SOFAS	0.304	0.180	0.844	-0.316	0.163	0.845			
PANSS-8 Total	-0.376	0.093	0.911	0.318	0.160	0.911			
PANSS-8 Positive	-0.316	0.163	0.911	0.332	0.142	0.869			
PANSS-8 Negative	-0.173	0.453	0.911	0.082	0.723	0.911			
	Tract 46								
Age	0.151	0.562	0.845	0.187	0.473	0.911	0.466	0.0595	0.845
CGI-S	-0.302	0.239	0.845	0.353	0.164	0.845	0.210	0.420	0.845
DUP	-0.258	0.317	0.911	-0.087	0.739	0.845	-0.081	0.901	0.911
SOFAS	0.056	0.831	0.949	-0.298	0.245	0.845	-0.252	0.328	0.845
PANSS-8 Total	-0.113	0.911	0.933	-0.008	0.973	0.911	-0.172	0.509	0.911
PANSS-8 Positive	-0.247	0.339	0.845	0.228	0.379	0.911	-0.046	0.861	0.911
PANSS-8 Negative	0.226	0.302	0.911	-0.371	0.142	0.845	-0.238	0.358	0.845
	Tract 65								
Age	-0.203	0.419	0.911	-0.103	0.683	0.962	-0.163	0.518	0.911
CGI-S	0.421	0.0820	0.690	-0.426	0.0781	0.690	-0.275	0.269	0.690
DUP	0.081	0.749	0.949	0.001	0.996	0.962	0.032	0.901	0.949
SOFAS	-0.276	0.268	0.690	-0.053	0.835	0.690	-0.273	0.274	0.845
PANSS-8 Total	0.005	0.984	0.962	4.25×10^{-6}	0.999	0.922	0.105	0.679	0.911
PANSS-8 Positive	0.119	0.664	0.921	-0.032	0.899	0.962	0.107	0.674	0.911
PANSS-8 Negative	-0.157	0.534	0.911	0.051	0.840	0.962	0.018	0.945	0.911

r: Pearson's correlation coefficient; CGI-S: Clinical Global Impressions Scale - Severity; DUP: Duration of Untreated Psychosis (in months); SOFAS: Social and Occupational Functioning Assessment Scale; PANSS-8: Positive and Negative Syndrome Scale - 8 Item Scale; PANSS-8 Positive: PANSS-8 total score for positive symptoms; PANSS-8 Negative: PANSS-8 total score for negative symptoms;

4.4 Discussion

4.4.1 Frontal lobe "U"-fibre DTI abnormalities

As part of our study focused on frontal lobe "U"-fibres, we examined changes of DTI derived metrics along the tract trajectory in patients with FES, which enabled detection of a reduction to FA and increased RD (Fig. 4.3). In 3 other studies of "U"-fibres using DTI, a similar reduction, but for tract-averaged FA was observed in patients with schizophrenia [76, 219, 220]. While there are differences between the current study and the studies mentioned (e.g. examination localized to the frontal lobe along tract trajectories, assessment of patients with FES), our findings are in agreement with these previous studies. Tract density differences were also evaluated, but no differences between patients and healthy controls were identified. The combination of reduced FA (indicative of less restricted diffusion), and increased RD (implying more diffusion in secondary and tertiary directions to axons), but preserved apparent density (streamline count) may relate to affected tissue microstructure in the frontal lobe "U"-fibres of patients with FES. Localized aberrations in myelin content may be a potential explanation, but this inference is tentative given the lack of direct correspondence between DTI measures and myelin [221]. While our analysis is unable to specifically identify or determine the timing of the phenomena that is occurring with respect to the onset of psychosis in the three affected "U"-shaped tracts in the frontal lobe, given the nature of our sample, we can conclude this effect precedes prolonged exposure to antipsychotics and other secondary physical and social effects of chronic illness.

The development of the short-ranged connections have also been observed to lag behind typical maturation in patients with schizophrenia relative to healthy individuals [222]. Furthermore, a lack of association with attention, working memory, and processing speed has been noted in "U"-fibres, which are thought to be associated with higher-order cognitive functions [222,223], with schizophrenia when compared against healthy controls [219]. In the present study, a modest association was found between FA of a frontal lobe "U"-fibre and the number of errors made during the TMT-B (which tests for planning, self-control and attention), but this did not withstand multiple comparisons correction. The degree of noted abnormalities (increased FA, reduced RD) observed in the present study, examined only in frontal "U"-fibres, may be insufficient to influence higher-order cognitive functions or be an invariant, albeit modest change irrespective of cognitive deficits in patients with schizophrenia. Our observations, in addition to previous studies of "U"-fibres in schizophrenia, may provide support for the hypothesis of developmental abnormalities due to the late maturation of "U"-fibres [10].

4.4.2 Localized aberrations in frontal lobe "U"-fibres

Irregularities observed along the affected tracts may be a contributing factor to abnormal interactions between brain regions, one of the hypotheses underpinning symptoms of psychosis [81–83]. Studies of functional networks, associated with brain activity and identified by statistical correlation of neurophysiological time series data, have corroborated abnormal interactions between brain regions identifying differences in networks of patients with schizophrenia when compared against healthy controls (e.g. [224–226]). Widespread regional DTI abnormalities have also been previously observed in studies of psychosis [85, 86]. As part of the current study, we mapped the identified frontal lobe "U"-fibres to both the nearest anatomic parcels (Desikan-Killiany atlas) and functional networks (Schaefer atlas - 100 parcels, 7 networks).

In this study, 3 frontal lobe "U"-shaped tracts were identified with localized abnormalities related to tissue microstructure, with 2 tracts residing in the left hemisphere: (1) Tract 9 - associated with the superior frontal and caudal middle frontal parcels and functionally associated with DMN and (2) Tract 46 - associated with the caudal middle frontal parcel and functionally associated with both the FPN and VAN. In the opposite hemisphere, (3) Tract 65 was observed to be associated with the superior frontal parcel and functionally associated with DMN. Moreover, the associated functional networks of the affected tracts have been previously shown to have altered activity in schizophrenia [220, 227, 228].

Previous post-mortem studies have demonstrated a significant reduction of oligodendrocytes, responsible for the formation of myelin, in patients with schizophrenia [229–232]. Specifically, a decrease in the number of oligodendrocytes, as well as altered spatial arrangement was observed in the superior frontal gyrus in patients with schizophrenia [230]. Oligodendrocyte abnormalities and ultimately the myelin anomalies may be related to oxidative stress, which have a downstream effect on oligodendrocyte precursor cells [233]. Increased oxidative stress can lead to the inability to produce myelin due to apoptosis of oligodendrocyte precursor cells that are transitioning to oligodendrocytes and has been suggested to be a likely cause of lack of myelination in schizophrenia [233]. The late maturing "U"-fibres is likely affected by the consequences of increased oxidative stress during its development and may be related to the observed anomalies in affected frontal lobe "U"-fibres.

Another circumstance of the observed DTI characteristics may be due to cell swelling, which has been observed in the prefrontal brain region of patients with schizophrenia [234]. Such phenomena has been associated with increased radial diffusivity [235], which was suggested in the observed DTI anomalies that were identified along the tract length (see section 4.3.2).

Other possibilities include a change in membrane permeability or due to a change in axon diameter. Aberrations, such as those observed in the present study, may be linked with abnormal interactions between the different brain regions and lead to a deficit of higher order cognitive functions.

4.4.3 Imaging and non-imaging confounds

The present study recruited participants age and socio-economically matched with no history of psychotic disorders or known neurological disorders and no current use of medications. However, other confounding factors may have contributed to noted observations such as use of recreational drugs (e.g. cannabis), smoking, and drinking. Moreover, environmental risk factors (e.g. birthing complications, parental age) and genetic factors that have been associated with schizophrenia were not considered in the present study and may have had an influence on observations. Previous studies have provided evidence of substance use inducing psychosis, as well as association of schizophrenia with other risk factors [236, 237].

In addition to non-imaging confounds, models such as DTI, which is commonly applied to investigate changes of the microstructural environment also suffer from limitations. Measures derived from DTI can be confounded by multiple tract orientations within a voxel (e.g. cause a reduction in FA), as well as be influenced by partial volume effects (e.g. more than a single tissue type within a voxel). The latter may affect "U"-fibre studies and associated along-tract measures as these tracts are found near the cortical surface with trajectories that follow gyral patterns. Future studies of "U"-fibres in FES may benefit from using stronger diffusion gradients and multiple diffusion shells to perform higher order modeling (e.g. neurite orientation dispersion and density imaging [40]), potentially allowing for probing of different tissue compartments to gain further insight on changes to "U"-fibres.

4.4.4 Limitations

This study of frontal lobe "U"-fibres in patients with FES is not without limitations. One challenge was the identification of corresponding "U"-shaped tracts while accounting for variations for morphological differences across individuals. To address this, we used a population-based template, examining frontal lobe tracts with similar trajectories as those from the template. An arbitrary threshold of 70% was used to identify frontal lobe "U"-shaped tracts as possible in the majority of both healthy control and patient groups. Consequently, this resulted in evaluation of just over half of all identified frontal lobe tracts, leaving out other potentially important "U"-fibres both in the frontal lobe and in other regions of the brain. In previous psychosis

studies of "U"-fibres, similar approaches have been used, examining tracts present in either all or the majority of the study participants [56, 76]. As knowledge of "U"-fibres is gained, future work may be able to identify corresponding "U"-fibres across individuals irrespective of morphological differences, relying on functional characterization of the "U"-shaped tracts. One such promising method was recently presented, using surface-based tractography techniques to identify the "U"-shaped tracts [238]

It has been noted that schizophrenia, which typically develops in early adulthood, tends to have a higher clinical prevalence in men than in women [84]. While there was no significant imbalance in sex distribution when comparing healthy controls and FES patients ($\chi^2 = 2.47$, $p = 0.116$), males were over-represented within the sample of patients ($\chi^2 = 15.36$, $p < 0.001$) in the present study. Consequently, observed differences may be biased towards male patients. Future studies should explore potential differences in "U"-fibres between males and females in FES.

In the present study, we performed a correlation of derived DTI measures from the affected segments of the frontal lobe "U"-fibres with clinical measures, where we did not observe any significant correlations following multiple comparisons correction. In contrast, a previous study of "U"-fibres in patients with schizophrenia determined a single "U"-shaped tract connecting the postcentral and supramarginal gyri to be correlated with negative symptoms [76]. Furthermore, meta-analyses have identified widespread DTI anomalies in patients with schizophrenia [85, 86]. Our observation of a lack of symptom correlations of frontal lobe "U"-fibres with clinical measures may be attributed to integrity of "U"-fibres being an invariant feature irrespective of symptom severity in patients with FES. Another possibility is the lack of sufficient power to identify a relationship between the DTI and clinical features due to the sample size of the present study.

4.5 Conclusion

We demonstrated quantitative changes that occur irrespective of symptom severity to the frontal lobe "U"-fibres in schizophrenia. The simultaneous decrease in FA and increase in RD suggest abnormalities in regards to the tissue microstructure of frontal lobe "U"-fibres, disrupting normal brain connectivity in patients with FES. Factors such as decreased oligodendrocytes (responsible for myelin formation) may contribute to the observed changes in patients with FES. Our observations from early stages of illness support the primary role for prefrontal disconnection and highlight the potential of tracking the progression of measures related to the

tissue microstructure in the short-ranged "U"-shaped fibres in patients with schizophrenia to establish their utility in marking the course of illness. Future work should explore the phenomena underlying the differences in DTI measures, identify affected "U"-fibres in other brain regions, assess longitudinal changes to the "U"-fibres, and further investigate the function of "U"-fibres and its relationship to cognition.

Chapter 5

Conclusions and future directions

5.1 Summary

Diffusion MRI (dMRI) has enabled the ability to probe the brain through the modelling of water movement, providing a method of approximating axonal trajectories and enabling examination of changes during healthy aging or as a consequence of pathology. Although there are a number of different diffusion models (as alluded to in section 1.3.3), as well as tractography techniques that can be broadly classified into two groups (section 1.3.4), the information gained has potential value in characterizing the human brain and clinical applications, such as treatment of patient populations with neuropsychiatric disorders. Furthermore, tractography techniques have the unique capacity to identify tracts of interest (e.g. corticospinal tract). There are many different groups of myelinated axons throughout the brain (section 1.2), with long-ranged tracts having been the most commonly examined. More recently, tractography of short-ranged connections, both "U"-shaped and residing in the deep-brain have garnered increased attention in an effort to gain a better understanding of the complex network of the structural connectivity. The work in the thesis examined the reliability of applying tractography techniques for studying these short-ranged connections and evaluated changes of such connections in a patient population with first episode schizophrenia (FES).

In chapter 2, we assessed the reliability of a template-based clustering approach in order to identify similar tracts across different individuals. This study additionally evaluated the same technique for identifying only the short-ranged, "U"-shaped tracts of the human brain, which required different parameters to identify the shorter and more compact tracts. Clustering techniques are used to identify tracts without requiring *a priori* knowledge and have been used in studies to identify tracts of interest (e.g. [101]). Applying two different clustering methods to a tractography template before using the clustered template, we evaluated the reliability of

template-based clustering approaches in identifying similar tracts in two unique datasets - (1) across different individuals, and (2) across the same individual. We demonstrated that template-based clustering approaches were able to reliably identify tracts throughout the brain and for the short-ranged, "U"-shaped tracts irrespective of the techniques chosen. Furthermore, we determined the use of a single evaluation metric (e.g. streamline count) on its own may not be a good indicator of reliability and should be used in conjunction with other metrics (e.g. spatial overlap, intraclass correlation) to corroborate reliability. Such indicators would improve overall confidence of such methods in identifying tracts of interest for further evaluation and clinical applications.

In chapter 3, we evaluated the reliability of identifying the short-range connections between structures of the deep brain, employing a targeted tractography approach that relies on ROIs (i.e. *a priori* knowledge) in the complex and compact region. With multiple tracts, including long-ranged tracts, traversing the region and contributing to the diffusion signal, performing tractography is difficult in deep brain. However, many of the tracts residing in the deep brain are also a part of important neural circuits responsible for function and cognition [13–15]. Most of the work studying the subcortical connectome have been in experimental animal studies using invasive means (e.g. anatomical tracers), with few tractography studies which focused on identifying and examining individual tracts. This work sought to identify the tracts of the subcortical connectome, comparing trajectories with those previously described in the literature. Focusing on well-described subcortical circuitry (e.g. motor, associative, and limbic), connections between subcortical structures of interest were identified relying on inclusion and exclusion regions of interests determined through histology-influenced atlases and probabilistic tractography. Through comparison with described trajectories in literature, we demonstrated the use of targeted tractography was able to reliably identify connections of interest in the subcortical connectome. In particular, connections between structures of the basal ganglia, as well as between the basal ganglia and peripheral thalamic nuclei demonstrated good reliability.

Chapter 4 combines the tractography techniques from chapter 2 and DTI to study changes of "U"-shaped tracts in patients with FES. One long-standing hypothesis underlying the symptoms of psychosis (and consequently schizophrenia) is the abnormal interaction of brain regions stemming from disrupted brain connectivity [81–83]. Previous studies have examined major white matter (WM) tracts, reporting abnormalities throughout the brain with DTI-derived measures [85,86]. With limited studies of short-ranged "U"-shaped connections in FES, we focused on those connections residing in the frontal lobe, one of the most studied cortical regions in schizophrenia [193]. Applying DTI-derived measures together with a template-based clus-

tering approach to identify frontal-lobe "U"-fibres, we identified three aberrant tracts where anomalies were detected along their lengths. All three tracts exhibited a decrease in fractional anisotropy and an increase in radial diffusivity. While unable to determine the exact cause of such observations, previous studies have identified decreased oligodendrocytes in similar brain regions, which are responsible for myelin formation [230].

5.2 Limitations of tractography

5.2.1 Resolving trajectories

The process of tractography requires a number of steps, including the selection of a model for estimating the underlying diffusion orientations within an imaging voxel (see section 1.3.3), as well as the choice of algorithm by joining together a discrete set of directions. Consequently, tractography is inherently limited by the shortcomings of the diffusion model chosen (e.g. DTI's ability to resolve crossing fibres), which can be partially attributed to the limitations of spatial and angular resolution. To combat this, the use of models such as constrained spherical deconvolution (CSD), which relies on improved angular resolution (e.g. information from more diffusion directions) has aided improvement of resolving different orientations. Despite the improvement to resolve multiple orientations with CSD, the model used primarily throughout this thesis, the ability to resolve multiple orientations has been limited to a crossing angle of approximately 30° [38]. With advances to hardware, improvements to acquire higher spatial and angular resolution can be gained and progress the ability to resolve the complex fibre orientations.

5.2.2 Validation

One of the shortcomings of tractography is the validity of the estimated trajectory, in particular when applied *in vivo*. Different techniques have been applied to confirm the presence and trajectory of major pathways (see section 1.3.5). However, such studies rely on invasive techniques and are performed in animal studies (e.g. non-human primates) or post-mortem tissue. Due to the sheer volume of "U"-shaped tracts (comprising the majority of the brain's WM axons), as well as morphological differences between individuals, validation of exact "U"-shaped tract trajectory would be difficult. Nonetheless, Klingler dissections have confirmed the presence of such connections. With respect to the subcortical connectome, tracer studies have confirmed the presence and trajectory of such connections in NHPs. With tracer examinations limited to animal models, combining information from tractography and tracers in NHPs may

provide the information necessary for inferring results of tractography applied to the human brain [190]. More recently, studies have started to examine the commonalities between the two techniques [190].

5.3 Future directions

5.3.1 Reproducibility and generalizability

In chapter 1, we defined reliability as the ability to produce the same results using the same techniques. In the subsequent chapters (2 and 3), we evaluated the reliability of tractography for two different techniques. With various methods used for identifyng tractography, each likely employed to meet the needs of a study, consensus of a single, optimal pipeline is unlikely to be reached. As such, there is an importance in assessing the reliability of each introduced technique. However, reliability is only one aspect that should evaluated for general adoption of a technique. Other important aspects to be emphasized include reproducibility of tractography (or the ability to produce similar results using different techniques on the same dataset), as well as generalizability (or ability to produce similar results using the same techniques on different datasets). Positive evaluations in all three aspects would greatly contribute to the adoption of tractography techniques and increase confidence of its use in other studies.

5.3.2 Applications of tractography

Tractography, as was used in chapter 4, can be used to identify and examine tracts of interest, assessing for changes in the WM (e.g. reduced FA, increased RD in FES). By examining quantitative measures along the length of a tract improves spatial precision in the detection of WM changes. The combination of quantitative measures and tractography can aid identification of important biomarkers related to aging or progression of disease. Such observations can lead to enhanced understanding of how the brain changes and can lead to improvement in treatment for patient populations. Moreover, the ability to identify notable tracts, as was done in Chapter 3, can benefit applications such as presurgical planning. Future studies can apply tractography techniques to study both the long-ranged and short-ranged connections of the human brain in order to gain further insights.

5.4 Conclusions

This work primarily assessed the reliability of identifying and examining short-ranged connections (e.g. "U"-shaped fibres and subcortico-subcortical) of the human brain, applying the technique to assess for changes in patients with FES. We demonstrated tractography techniques are not only reliable in identifying long-ranged tracts, but also for detecting short-ranged connections and associated anomalies. The ability to examine all the different types of tracts in the human brain will benefit the understanding of the complex WM network that enables interactions between brain regions and how it can change due to aging or pathology. Advancements in hardware (see section 5.2.1) will only serve to improve the ability to delineate tracts of interest at finer resolutions. Furthermore, evaluations of reliability, reproducibility, and generalizability (see section 5.3.1) will strengthen the confidence in tractography and increase adoption of such techniques for future studies.

Bibliography

[1] A. Schüz and V. Braitenberg, *The Human Cortical White Matter: Quantitative Aspects of Cortico-Cortical Long-Range Connectivity*, p. 377–385. Taylor & Francis Inc., 2002.

[2] H.-J. Park and K. Friston, "Structural and functional brain networks: from connections to cognition," *Science*, vol. 342, no. 6158, 2013.

[3] M. Guevara, P. Guevara, C. Román, and J.-F. Mangin, "Superficial white matter: A review on the dmri analysis methods and applications," *NeuroImage*, vol. 212, p. 116673, May 2020.

[4] K. Oishi, K. Zilles, K. Amunts, A. Faria, H. Jiang, X. Li, K. Akhter, K. Hua, R. Woods, A. W. Toga, *et al.*, "Human brain white matter atlas: identification and assignment of common anatomical structures in superficial white matter," *Neuroimage*, vol. 43, pp. 447–457, Nov. 2008.

[5] P. Krack, M. I. Hariz, C. Baunez, J. Guridi, and J. A. Obeso, "Deep brain stimulation: from neurology to psychiatry?," *Trends in Neurosciences*, vol. 33, pp. 474–484, Oct. 2010.

[6] H. Gray, *Anatomy of the Human Body*, vol. 8. Lea & Febiger, 1878.

[7] T. Meynert, *Psychiatry: A clinical treatise on diseases of the fore-brain based upon a study of its structure, functions, and nutrition*. GP Putnam's Sons, 1890.

[8] M. Catani, F. Dell'Acqua, F. Vergani, F. Malik, H. Hodge, P. Roy, R. Valabregue, and M. Thiebaut de Schotten, "Short frontal lobe connections of the human brain," *Cortex*, vol. 48, pp. 273–291, Feb. 2012.

[9] J. Rosett, *Intercortical Systems of the Human Cerebrum: Mapped by Means of New Anatomic Methods*. Columbia University Press, 1933.

[10] O. R. Phillips, S. H. Joshi, F. Squitieri, C. Sanchez-Castaneda, K. Narr, D. W. Shattuck, C. Caltagirone, U. Sabatini, and M. Di Paola, "Major superficial white matter abnormalities in huntington's disease," *Frontiers in Neuroscience*, vol. 10, p. 197, 2016.

[11] M.-A. d'Albis, P. Guevara, M. Guevara, C. Laidi, J. Boisgontier, S. Sarrazin, D. Duclap, R. Delorme, F. Bolognani, C. Czech, C. Bouquet, M. Ly-Le Moal, S. Holiga, A. Amestoy, I. Scheid, A. Gaman, M. Leboyer, C. Poupon, J.-F. Mangin, and J. Houenou, "Local structural connectivity is associated with social cognition in autism spectrum disorder," *Brain*, vol. 141, pp. 3472–3481, Dec. 2018.

[12] R. O'Halloran, R. Feldman, L. Marcuse, M. Fields, B. Delman, S. Frangou, and P. Balchandani, "A method for u-fiber quantification from 7 t diffusion-weighted mri data tested in patients with nonlesional focal epilepsy," *NeuroReport*, vol. 28, pp. 457–461, May 2017.

[13] M. N. Gallay, D. Jeanmonod, J. Liu, and A. Morel, "Human pallidothalamic and cerebellothalamic tracts: anatomical basis for functional stereotactic neurosurgery," *Brain Structure and Function*, vol. 212, pp. 443–463, Aug. 2008.

[14] M. A. Sommer, "The role of the thalamus in motor control," *Current Opinion in Neurobiology*, vol. 13, pp. 663–670, Dec. 2003.

[15] G. d. Hollander, M. C. Keuken, and B. U. Forstmann, "The subcortical cocktail problem; mixed signals from the subthalamic nucleus and substantia nigra," *PLOS ONE*, vol. 10, p. e0120572, Mar. 2015.

[16] J. Klingler, *Erleichterung der makrokopischen Präparation des Gehirns durch den Gefrierprozess*. Orell Füssli, 1935.

[17] K. Oishi, S. Mori, J. C. Troncoso, and F. A. Lenz, "Mapping tracts in the human subthalamic area by 11.7 t ex vivo diffusion tensor imaging," *Brain Struct Funct*, vol. 225, no. 4, p. 20, 2020.

[18] I. I. Rabi, J. R. Zacharias, S. Millman, and P. Kusch, "A new method of measuring nuclear magnetic moment," *Phys. Rev.*, vol. 53, pp. 318–318, Feb. 1938.

[19] F. Bloch, W. W. Hansen, and M. Packard, "Nuclear induction," *Phys. Rev.*, vol. 69, pp. 127–127, Feb. 1946.

[20] E. M. Purcell, H. C. Torrey, and R. V. Pound, "Resonance absorption by nuclear magnetic moments in a solid," *Phys. Rev.*, vol. 69, pp. 37–38, Jan. 1946.

[21] R. R. Ernst and W. A. Anderson, "Application of fourier transform spectroscopy to magnetic resonance," *Review of Scientific Instruments*, vol. 37, pp. 93–102, Jan. 1966.

[22] P. C. Lauterbur, "Image formation by induced local interactions: Examples employing nuclear magnetic resonance," *Nature*, vol. 242, pp. 190–191, Mar. 1973.

[23] P. Mansfield and P. K. Grannell, "Nmr 'diffraction' in solids?," *Journal of Physics C: solid state physics*, vol. 6, no. 22, p. L422, 1973.

[24] A. Kumar, D. Welti, and R. R. Ernst, "NMR Fourier zeugmatography," *Journal of Magnetic Resonance (1969)*, vol. 18, pp. 69–83, Apr. 1975.

[25] E. L. Hahn, "Spin echoes," *Phys. Rev.*, vol. 80, pp. 580–594, Nov. 1950.

[26] D. W. McRobbie, E. A. Moore, M. J. Graves, and M. R. Prince, *MRI from Picture to Proton*. Cambridge University Press, 2 ed., 2006.

[27] C. Constantinides, *Magnetic Resonance Imaging: The Basics*. Boca Raton: CRC Press, Dec. 2015.

[28] D. Le Bihan, E. Breton, D. Lallemand, P. Grenier, E. Cabanis, and M. Laval-Jeantet, "Mr imaging of intravoxel incoherent motions: application to diffusion and perfusion in neurologic disorders.," *Radiology*, vol. 161, pp. 401–407, Nov. 1986.

[29] M. E. Moseley, Y. Cohen, J. Mintorovitch, L. Chileuitt, H. Shimizu, J. Kucharczyk, M. F. Wendland, and P. R. Weinstein, "Early detection of regional cerebral ischemia in cats: Comparison of diffusion- and t2-weighted mri and spectroscopy," *Magnetic Resonance in Medicine*, vol. 14, no. 2, pp. 330–346, 1990.

[30] E. O. Stejskal and J. E. Tanner, "Spin diffusion measurements: Spin echoes in the presence of a time-dependent field gradient," *The Journal of Chemical Physics*, vol. 42, pp. 288–292, Jan. 1965.

[31] P. Douek, R. Turner, J. Pekar, N. Patronas, and D. Le Bihan, "Mr color mapping of myelin fiber orientation," *J Comput Assist Tomogr*, vol. 15, no. 6, pp. 923–929, 1991.

[32] P. J. Basser, J. Mattiello, and D. LeBihan, "Mr diffusion tensor spectroscopy and imaging.," *Biophysical Journal*, vol. 66, pp. 259–267, Jan. 1994.

[33] C. R. Figley, M. N. Uddin, K. Wong, J. Kornelsen, J. Puig, and T. D. Figley, "Potential Pitfalls of Using Fractional Anisotropy, Axial Diffusivity, and Radial Diffusivity as Biomarkers of Cerebral White Matter Microstructure," *Frontiers in Neuroscience*, vol. 15, 2022.

[34] B. Jeurissen, A. Leemans, J. Tournier, D. K. Jones, and J. Sijbers, "Investigating the prevalence of complex fiber configurations in white matter tissue with diffusion magnetic resonance imaging," *Human Brain Mapping*, vol. 34, pp. 2747–2766, May 2012.

[35] D. Alexander, G. Barker, and S. Arridge, "Detection and modeling of non-gaussian apparent diffusion coefficient profiles in human brain data," *Magnetic Resonance in Medicine: An Official Journal of the International Society for Magnetic Resonance in Medicine*, vol. 48, no. 2, pp. 331–340, 2002.

[36] J. D. Tournier, F. Calamante, D. G. Gadian, and A. Connelly, "Direct estimation of the fiber orientation density function from diffusion-weighted MRI data using spherical deconvolution," *NeuroImage*, vol. 23, pp. 1176–1185, Nov. 2004.

[37] J.-D. Tournier, F. Calamante, and A. Connelly, "Robust determination of the fibre orientation distribution in diffusion mri: Non-negativity constrained super-resolved spherical deconvolution," *NeuroImage*, vol. 35, pp. 1459–1472, May 2007.

[38] J. D. Tournier, C.-H. Yeh, F. Calamante, K.-H. Cho, A. Connelly, and C.-P. Lin, "Resolving crossing fibres using constrained spherical deconvolution: Validation using diffusion-weighted imaging phantom data," *NeuroImage*, vol. 42, pp. 617–625, Aug. 2008.

[39] I. O. Jelescu and M. D. Budde, "Design and validation of diffusion mri models of white matter," *Frontiers in physics*, vol. 5, p. 61, 2017.

[40] H. Zhang, T. Schneider, C. A. Wheeler-Kingshott, and D. C. Alexander, "NODDI: Practical in vivo neurite orientation dispersion and density imaging of the human brain," *NeuroImage*, vol. 61, pp. 1000–1016, July 2012.

[41] S. N. Sotiropoulos and A. Zalesky, "Building connectomes using diffusion mri: why, how and but," *NMR in Biomedicine*, vol. 32, no. 4, p. e3752, 2019.

[42] P. J. Basser, S. Pajevic, C. Pierpaoli, J. Duda, and A. Aldroubi, "In vivo fiber tractography using dt-mri data," *Magnetic Resonance in Medicine*, vol. 44, pp. 625–632, Oct. 2000.

[43] S. Mori, B. J. Crain, V. P. Chacko, and P. C. M. Van Zijl, "Three-dimensional tracking of axonal projections in the brain by magnetic resonance imaging," *Annals of Neurology*, vol. 45, no. 2, pp. 265–269, 1999.

[44] D. K. Jones, "Tractography gone wild: Probabilistic fibre tracking using the wild bootstrap with diffusion tensor mri," *IEEE Transactions on Medical Imaging*, vol. 27, pp. 1268–1274, Sept. 2008.

[45] M. Descoteaux, R. Deriche, T. R. Knosche, and A. Anwander, "Deterministic and probabilistic tractography based on complex fibre orientation distributions," *IEEE Transactions on Medical Imaging*, vol. 28, pp. 269–286, Feb. 2009.

[46] T. E. J. Behrens, H. Johansen-Berg, M. W. Woolrich, S. M. Smith, C. a. M. Wheeler-Kingshott, P. A. Boulby, G. J. Barker, E. L. Sillery, K. Sheehan, O. Ciccarelli, A. J. Thompson, J. M. Brady, and P. M. Matthews, "Non-invasive mapping of connections between human thalamus and cortex using diffusion imaging," *Nature Neuroscience*, vol. 6, pp. 750–757, July 2003.

[47] T. Sarwar, K. Ramamohanarao, and A. Zalesky, "Mapping connectomes with diffusion mri: deterministic or probabilistic tractography?," *Magnetic Resonance in Medicine*, vol. 81, no. 2, pp. 1368–1384, 2019.

[48] B. Tunç, W. A. Parker, M. Ingalhalikar, and R. Verma, "Automated tract extraction via atlas based adaptive clustering," *NeuroImage*, vol. 102, pp. 596–607, 2014.

[49] S. Mori and P. C. M. van Zijl, "Fiber tracking: principles and strategies – a technical review," *NMR in Biomedicine*, vol. 15, no. 7-8, pp. 468–480, 2002.

[50] S. Wakana, A. Caprihan, M. M. Panzenboeck, J. H. Fallon, M. Perry, R. L. Gollub, K. Hua, J. Zhang, H. Jiang, P. Dubey, A. Blitz, P. van Zijl, and S. Mori, "Reproducibility of quantitative tractography methods applied to cerebral white matter," *NeuroImage*, vol. 36, pp. 630–644, July 2007.

[51] M. Maddah, W. E. L. Grimson, S. K. Warfield, and W. M. Wells, "A unified framework for clustering and quantitative analysis of white matter fiber tracts," *Medical Image Analysis*, vol. 12, no. 2, pp. 191–202, 2008.

[52] L. J. O'Donnell and C. F. Westin, "Automatic tractography segmentation using a high-dimensional white matter atlas," *IEEE Transactions on Medical Imaging*, vol. 26, pp. 1562–1575, Nov. 2007.

[53] E. Garyfallidis, M. Brett, M. Correia, G. Williams, and I. Nimmo-Smith, "Quickbundles, a method for tractography simplification," *Frontiers in Neuroscience*, vol. 6, p. 175, 2012.

[54] K. H. Maier-Hein, P. F. Neher, J.-C. Houde, M.-A. Côté, E. Garyfallidis, J. Zhong, M. Chamberland, F.-C. Yeh, Y.-C. Lin, Q. Ji, and others, "The challenge of mapping the human connectome based on diffusion tractography," *Nature communications*, vol. 8, no. 1, pp. 1–13, 2017.

[55] K. G. Schilling, A. Daducci, K. Maier-Hein, C. Poupon, J.-C. Houde, V. Nath, A. W. Anderson, B. A. Landman, and M. Descoteaux, "Challenges in diffusion mri tractography – lessons learned from international benchmark competitions," *Magnetic Resonance Imaging*, vol. 57, pp. 194–209, 2019.

[56] M. Guevara, C. Román, J. Houenou, D. Duclap, C. Poupon, J. F. Mangin, and P. Guevara, "Reproducibility of superficial white matter tracts using diffusion-weighted imaging tractography," *NeuroImage*, vol. 147, pp. 703–725, Feb. 2017.

[57] S. Mori and J.-D. Tournier, *Introduction to Diffusion Tensor Imaging: And Higher Order Models*. Academic Press, Aug. 2013.

[58] D. B. Aydogan, R. Jacobs, S. Dulawa, S. L. Thompson, M. C. Francois, A. W. Toga, H. Dong, J. A. Knowles, and Y. Shi, "When tractography meets tracer injections: a systematic study of trends and variation sources of diffusion-based connectivity," *Brain structure & function*, vol. 223, pp. 2841–2858, July 2018.

[59] S. Jbabdi, S. N. Sotiropoulos, S. N. Haber, D. C. Van Essen, and T. E. Behrens, "Measuring macroscopic brain connections in vivo," *Nature neuroscience*, vol. 18, no. 11, p. 1546, 2015.

[60] F. N. Mushtaha, T. K. Kuehn, O. El-Deeb, S. A. Rohani, L. W. Helpard, J. Moore, H. Ladak, A. Moehring, C. A. Baron, and A. R. Khan, "Design and characterization of a 3d-printed axon-mimetic phantom for diffusion mri," *Magnetic Resonance in Medicine*, vol. 86, no. 5, pp. 2482–2496, 2021.

[61] K. Rojkova, E. Volle, M. Urbanski, F. Humbert, F. Dell'Acqua, and M. Thiebaut de Schotten, "Atlasing the frontal lobe connections and their variability due to age and education: a spherical deconvolution tractography study," *Brain Structure and Function*, vol. 221, pp. 1751–1766, Apr. 2016.

[62] F. Vergani, L. Lacerda, J. Martino, J. Attems, C. Morris, P. Mitchell, M. T. d. Schotten, and F. Dell'Acqua, "White matter connections of the supplementary motor area in humans," *Journal of Neurology, Neurosurgery & Psychiatry*, vol. 85, pp. 1377–1385, Dec. 2014.

[63] F. Movahedian Attar, E. Kirilina, D. Haenelt, K. J. Pine, R. Trampel, L. J. Edwards, and N. Weiskopf, "Mapping Short Association Fibers in the Early Cortical Visual Processing Stream Using In Vivo Diffusion Tractography," *Cerebral Cortex (New York, N.Y.: 1991)*, vol. 30, pp. 4496–4514, June 2020.

[64] T. Zhang, H. Chen, L. Guo, K. Li, L. Li, S. Zhang, D. Shen, X. Hu, and T. Liu, "Characterization of u-shape streamline fibers: Methods and applications," *Medical Image Analysis*, vol. 18, pp. 795–807, July 2014.

[65] P. Guevara, C. Poupon, D. Rivière, Y. Cointepas, M. Descoteaux, B. Thirion, and J. F. Mangin, "Robust clustering of massive tractography datasets," *NeuroImage*, vol. 54, pp. 1975–1993, Feb. 2011.

[66] P. Guevara, D. Duclap, C. Poupon, L. Marrakchi-Kacem, P. Fillard, D. Le Bihan, M. Leboyer, J. Houenou, and J. F. Mangin, "Automatic fiber bundle segmentation in massive tractography datasets using a multi-subject bundle atlas," *NeuroImage*, vol. 61, pp. 1083–1099, July 2012.

[67] E. Pardo, P. Guevara, D. Duclap, J. Houenou, A. Lebois, B. Schmitt, D. L. Bihan, J. Mangin, and C. Poupon, "Study of the variability of short association bundles on a HARDI database," in *2013 35th Annual International Conference of the IEEE Engineering in Medicine and Biology Society (EMBC)*, pp. 77–80, July 2013.

[68] A. A. Oyefiade, S. Ameis, J. P. Lerch, C. Rockel, K. U. Szulc, N. Scantlebury, A. Decker, J. Jefferson, S. Spichak, and D. J. Mabbott, "Development of short-range white matter in healthy children and adolescents," *Human Brain Mapping*, vol. 39, no. 1, pp. 204–217, 2018.

[69] C. Román, N. Cárdenas, C. Poupon, J.-F. Mangin, and P. Guevara, "The effect of the number of fibers in tractography reconstruction of white matter bundles," in *2019 41st Annual International Conference of the IEEE Engineering in Medicine and Biology Society (EMBC)*, pp. 2825–2829, July 2019.

[70] A. Pron, C. Deruelle, and O. Coulon, "U-shape short-range extrinsic connectivity organisation around the human central sulcus," *Brain Structure and Function*, vol. 226, pp. 179–193, Jan. 2021.

[71] L. M. Ostrowski, D. Y. Song, E. L. Thorn, E. E. Ross, S. M. Stoyell, D. M. Chinappen, U. T. Eden, M. A. Kramer, B. C. Emerton, A. K. Morgan, S. M. Stufflebeam, and C. J. Chu, "Dysmature superficial white matter microstructure in developmental focal epilepsy," *Brain Communications*, vol. 1, Jan. 2019.

[72] W. Reginold, A. C. Luedke, J. Itorralba, J. Fernandez-Ruiz, O. Islam, and A. Garcia, "Altered Superficial White Matter on Tractography MRI in Alzheimer's Disease," *Dementia and Geriatric Cognitive Disorders Extra*, vol. 6, no. 2, pp. 233–241, 2016.

[73] B. Bigham, S. A. Zamanpour, F. Zemorshidi, F. Boroumand, H. Zare, and f. t. A. D. N. Initiative, "Identification of Superficial White Matter Abnormalities in Alzheimer's Disease and Mild Cognitive Impairment Using Diffusion Tensor Imaging," *Journal of Alzheimer's Disease Reports*, vol. 4, pp. 49–59, Jan. 2020.

[74] K. Buyukturkoglu, C. Vergara, V. Fuentealba, C. Tozlu, J. B. Dahan, B. E. Carroll, A. Kuceyeski, C. S. Riley, J. F. Sumowski, C. G. Oliva, R. Sitaram, P. Guevara, and V. M. Leavitt, "Machine learning to investigate superficial white matter integrity in early multiple sclerosis," *Journal of Neuroimaging*, vol. 32, no. 1, pp. 36–47, 2022.

[75] Y. Zhang, B. Huang, Q. Chen, L. Wang, L. Zhang, K. Nie, Q. Huang, and R. Huang, "Altered microstructural properties of superficial white matter in patients with Parkinson's disease," *Brain Imaging and Behavior*, vol. 16, pp. 476–491, Feb. 2022.

[76] E. Ji, P. Guevara, M. Guevara, A. Grigis, N. Labra, S. Sarrazin, N. Hamdani, F. Bellivier, M. Delavest, M. Leboyer, R. Tamouza, C. Poupon, J.-F. Mangin, and J. Houenou, "Increased and decreased superficial white matter structural connectivity in schizophrenia and bipolar disorder," *Schizophrenia Bulletin*, vol. 45, pp. 1367–1378, Oct. 2019.

[77] V. E. Rozanski, N. M. d. Silva, S.-A. Ahmadi, J. Mehrkens, J. d. S. Cunha, J.-C. Houde, C. Vollmar, K. Bötzel, and M. Descoteaux, "The role of the pallidothalamic fibre tracts in deep brain stimulation for dystonia: A diffusion MRI tractography study," *Human Brain Mapping*, vol. 38, no. 3, pp. 1224–1232, 2017.

[78] J. M. Avecillas-Chasin and C. R. Honey, "Modulation of nigrofugal and pallidofugal pathways in deep brain stimulation for parkinson disease," *Neurosurgery*, vol. 86, pp. E387–E397, Apr. 2020.

[79] S. Bertino, G. A. Basile, A. Bramanti, G. P. Anastasi, A. Quartarone, D. Milardi, and A. Cacciola, "Spatially coherent and topographically organized pathways of the human globus pallidus," *Human Brain Mapping*, vol. 41, no. 16, pp. 4641–4661, 2020.

[80] A. L. B. Raghu, J. Eraifej, N. Sarangmat, J. Stein, J. J. FitzGerald, S. Payne, T. Z. Aziz, and A. L. Green, "Pallido-putaminal connectivity predicts outcomes of deep brain stimulation for cervical dystonia," *Brain: A Journal of Neurology*, p. awab280, July 2021.

[81] C. Wernicke, *Grundrisse der Psychiatrie*. Leipzig, Germany: Thieme, 1906.

[82] K. E. Stephan, K. J. Friston, and C. D. Frith, "Dysconnection in Schizophrenia: From Abnormal Synaptic Plasticity to Failures of Self-monitoring," *Schizophrenia Bulletin*, vol. 35, pp. 509–527, May 2009.

[83] A. Fornito, A. Zalesky, C. Pantelis, and E. T. Bullmore, "Schizophrenia, neuroimaging and connectomics," *NeuroImage*, vol. 62, pp. 2296–2314, Oct. 2012.

[84] S. Jauhar, M. Johnstone, and P. J. McKenna, "Schizophrenia," *The Lancet*, vol. 399, pp. 473–486, Jan. 2022.

[85] S. Kelly, N. Jahanshad, A. Zalesky, P. Kochunov, I. Agartz, C. Alloza, O. A. Andreassen, C. Arango, N. Banaj, S. Bouix, C. A. Bousman, R. M. Brouwer, J. Bruggemann, J. Bustillo, W. Cahn, V. Calhoun, D. Cannon, V. Carr, S. Catts, J. Chen, J.-x. Chen, X. Chen, C. Chiapponi, K. K. Cho, V. Ciullo, A. S. Corvin, B. Crespo-Facorro, V. Cropley, P. De Rossi, C. M. Diaz-Caneja, E. W. Dickie, S. Ehrlich, F.-m. Fan, J. Faskowitz, H. Fatouros-Bergman, L. Flyckt, J. M. Ford, J.-P. Fouche, M. Fukunaga, M. Gill, D. C. Glahn, R. Gollub, E. D. Goudzwaard, H. Guo, R. E. Gur, R. C. Gur, T. P. Gurholt, R. Hashimoto, S. N. Hatton, F. A. Henskens, D. P. Hibar, I. B. Hickie, L. E. Hong, J. Horacek, F. M. Howells, H. E. Hulshoff Pol, C. L. Hyde, D. Isaev, A. Jablensky, P. R. Jansen, J. Janssen, E. G. Jönsson, L. A. Jung, R. S. Kahn, Z. Kikinis, K. Liu, P. Klauser, C. Knöchel, M. Kubicki, J. Lagopoulos, C. Langen, S. Lawrie, R. K. Lenroot, K. O. Lim, C. Lopez-Jaramillo, A. Lyall, V. Magnotta, R. C. W. Mandl, D. H. Mathalon, R. W. McCarley, S. McCarthy-Jones, C. McDonald, S. McEwen, A. McIntosh, T. Melicher, R. I. Mesholam-Gately, P. T. Michie, B. Mowry, B. A. Mueller, D. T. Newell, P. O'Donnell, V. Oertel-Knöchel, L. Oestreich, S. A. Paciga, C. Pantelis, O. Pasternak, G. Pearlson, G. R. Pellicano, A. Pereira, J. Pineda Zapata, F. Piras, S. G. Potkin, A. Preda, P. E. Rasser, D. R. Roalf, R. Roiz, A. Roos, D. Rotenberg, T. D. Satterthwaite, P. Savadjiev, U. Schall, R. J. Scott, M. L. Seal, L. J. Seidman, C. Shannon Weickert, C. D. Whelan, M. E. Shenton, J. S. Kwon, G. Spalletta, F. Spaniel, E. Sprooten, M. Stäblein, D. J. Stein, S. Sundram, Y. Tan, S. Tan, S. Tang, H. S. Temmingh, L. T. Westlye, S. Tønnesen, D. Tordesillas-Gutierrez, N. T. Doan, J. Vaidya, N. E. M. van Haren, C. D. Vargas, D. Vecchio, D. Velakoulis, A. Voineskos, J. Q. Voyvodic, Z. Wang, P. Wan, D. Wei, T. W. Weickert, H. Whalley, T. White, T. J. Whitford, J. D. Wojcik, H. Xiang, Z. Xie, H. Yamamori, F. Yang, N. Yao, G. Zhang, J. Zhao, T. G. M. van Erp, J. Turner, P. M. Thompson, and G. Donohoe, "Widespread white matter microstructural differences in schizophrenia across 4322 individuals: results from the ENIGMA Schizophrenia DTI Working Group," *Molecular Psychiatry*, vol. 23, pp. 1261–1269, May 2018.

[86] E. Vitolo, M. K. Tatu, C. Pignolo, F. Cauda, T. Costa, A. Ando', and A. Zennaro, "White matter and schizophrenia: A meta-analysis of voxel-based morphometry and diffusion tensor imaging studies," *Psychiatry Research: Neuroimaging*, vol. 270, pp. 8–21, Dec. 2017.

[87] F. Rheault, P. Poulin, A. V. Caron, E. St-Onge, and M. Descoteaux, "Common misconceptions, hidden biases and modern challenges of dmri tractography," *Journal of neural engineering*, vol. 17, no. 1, p. 011001, 2020.

[88] M. Mesulam, "From sensation to cognition," *Brain*, vol. 121, pp. 1013–1052, June 1998.

[89] T. Klingberg, C. J. Vaidya, J. D. E. Gabrieli, M. E. Moseley, and M. Hedehus, "Myelination and organization of the frontal white matter in children: a diffusion tensor mri study," *NeuroReport*, vol. 10, pp. 2817–2821, Sept. 1999.

[90] C. M. Filley and R. D. Fields, "White matter and cognition: making the connection," *Journal of Neurophysiology*, vol. 116, pp. 2093–2104, Aug. 2016.

[91] T. E. Conturo, N. F. Lori, T. S. Cull, E. Akbudak, A. Z. Snyder, J. S. Shimony, R. C. McKinstry, H. Burton, and M. E. Raichle, "Tracking neuronal fiber pathways in the living human brain," *Proceedings of the National Academy of Sciences*, vol. 96, pp. 10422–10427, Aug. 1999.

[92] R. Bammer, "Basic principles of diffusion-weighted imaging," *European Journal of Radiology*, vol. 45, pp. 169–184, Mar. 2003.

[93] N. Bernasconi, S. Duchesne, A. Janke, J. Lerch, D. L. Collins, and A. Bernasconi, "Whole-brain voxel-based statistical analysis of gray matter and white matter in temporal lobe epilepsy," *NeuroImage*, vol. 23, pp. 717–723, Oct. 2004.

[94] R. M. Govindan, M. I. Makki, S. K. Sundaram, C. Juhász, and H. T. Chugani, "Diffusion tensor analysis of temporal and extra-temporal lobe tracts in temporal lobe epilepsy," *Epilepsy Research*, vol. 80, pp. 30–41, July 2008.

[95] J. D. Riley, D. L. Franklin, V. Choi, R. C. Kim, D. K. Binder, S. C. Cramer, and J. J. Lin, "Altered white matter integrity in temporal lobe epilepsy: Association with cognitive and clinical profiles," *Epilepsia*, vol. 51, pp. 536–545, Apr. 2010.

[96] Y. Wu, F. Zhang, N. Makris, Y. Ning, I. Norton, S. She, H. Peng, Y. Rathi, Y. Feng, H. Wu, and L. J. O'Donnell, "Investigation into local white matter abnormality in emotional processing and sensorimotor areas using an automatically annotated fiber clustering in major depressive disorder," *NeuroImage*, vol. 181, pp. 16–29, Nov. 2018.

[97] F. Zhang, P. Savadjiev, W. Cai, Y. Song, Y. Rathi, B. Tunç, D. Parker, T. Kapur, R. T. Schultz, N. Makris, R. Verma, and L. J. O'Donnell, "Whole brain white matter connectivity analysis using machine learning: An application to autism," *NeuroImage*, vol. 172, pp. 826–837, May 2018.

[98] A. Yendiki, P. Panneck, P. Srinivasan, A. Stevens, L. Zöllei, J. Augustinack, R. Wang, D. Salat, S. Ehrlich, T. Behrens, S. Jbabdi, R. Gollub, and B. Fischl, "Automated probabilistic reconstruction of white-matter pathways in health and disease using an atlas of the underlying anatomy," *Frontiers in Neuroinformatics*, vol. 5, 2011.

[99] A. N. Voineskos, L. J. O'Donnell, N. J. Lobaugh, D. Markant, S. H. Ameis, M. Niethammer, B. H. Mulsant, B. G. Pollock, J. L. Kennedy, C. F. Westin, and M. E. Shenton, "Quantitative examination of a novel clustering method using magnetic resonance diffusion tensor tractography," *NeuroImage*, vol. 45, pp. 370–376, Apr. 2009.

[100] E. Garyfallidis, M.-A. Côté, F. Rheault, J. Sidhu, J. Hau, L. Petit, D. Fortin, S. Cunanne, and M. Descoteaux, "Recognition of white matter bundles using local and global streamline-based registration and clustering," *NeuroImage*, vol. 170, pp. 283–295, Apr. 2018.

[101] F. Zhang, Y. Wu, I. Norton, L. Rigolo, Y. Rathi, N. Makris, and L. J. O'Donnell, "An anatomically curated fiber clustering white matter atlas for consistent white matter tract parcellation across the lifespan," *NeuroImage*, vol. 179, pp. 429–447, Oct. 2018.

[102] C. Román, M. Guevara, R. Valenzuela, M. Figueroa, J. Houenou, D. Duclap, C. Poupon, J.-F. Mangin, and P. Guevara, "Clustering of whole-brain white matter short association bundles using hardi data," *Frontiers in Neuroinformatics*, vol. 11, 2017.

[103] F. Zhang, Y. Wu, I. Norton, Y. Rathi, A. J. Golby, and L. J. O'Donnell, "Test–retest reproducibility of white matter parcellation using diffusion mri tractography fiber clustering," *Human Brain Mapping*, vol. 40, no. 10, pp. 3041–3057, 2019.

[104] K. Gorgolewski, C. D. Burns, C. Madison, D. Clark, Y. O. Halchenko, M. L. Waskom, and S. S. Ghosh, "Nipype: a flexible, lightweight and extensible neuroimaging data processing framework in python," *Frontiers in Neuroinformatics*, vol. 5, p. 13, 2011.

[105] J.-D. Tournier, R. Smith, D. Raffelt, R. Tabbara, T. Dhollander, M. Pietsch, D. Christiaens, B. Jeurissen, C.-H. Yeh, and A. Connelly, "Mrtrix3: A fast, flexible and open software framework for medical image processing and visualisation," *NeuroImage*, vol. 202, p. 116137, Nov. 2019.

[106] E. Garyfallidis, M. Brett, B. Amirbekian, A. Rokem, S. van der Walt, M. Descoteaux, I. Nimmo-Smith, and Dipy Contributors, "Dipy, a library for the analysis of diffusion mri data," *Frontiers in Neuroinformatics*, vol. 8, Feb. 2014.

[107] M. F. Glasser, S. N. Sotiropoulos, J. A. Wilson, T. S. Coalson, B. Fischl, J. L. Andersson, J. Xu, S. Jbabdi, M. Webster, J. R. Polimeni, D. C. Van Essen, and M. Jenkinson, "The minimal preprocessing pipelines for the human connectome project," *NeuroImage*, vol. 80, pp. 105–124, Oct. 2013.

[108] D. C. Van Essen, S. M. Smith, D. M. Barch, T. E. J. Behrens, E. Yacoub, and K. Ugurbil, "The wu-minn human connectome project: An overview," *NeuroImage*, vol. 80, pp. 62–79, Oct. 2013.

[109] B. Fischl, A. van der Kouwe, C. Destrieux, E. Halgren, F. Ségonne, D. H. Salat, E. Busa, L. J. Seidman, J. Goldstein, D. Kennedy, V. Caviness, N. Makris, B. Rosen, and A. M. Dale, "Automatically parcellating the human cerebral cortex," *Cerebral Cortex*, vol. 14, pp. 11–22, Jan. 2004.

[110] D. C. Van Essen, K. Ugurbil, E. Auerbach, D. Barch, T. E. J. Behrens, R. Bucholz, A. Chang, L. Chen, M. Corbetta, S. W. Curtiss, S. Della Penna, D. Feinberg, M. F. Glasser, N. Harel, A. C. Heath, L. Larson-Prior, D. Marcus, G. Michalareas, S. Moeller, R. Oostenveld, S. E. Petersen, F. Prior, B. L. Schlaggar, S. M. Smith, A. Z. Snyder, J. Xu, and E. Yacoub, "The human connectome project: A data acquisition perspective," *NeuroImage*, vol. 62, pp. 2222–2231, Oct. 2012.

[111] S. N. Sotiropoulos, S. Jbabdi, J. Xu, J. L. Andersson, S. Moeller, E. J. Auerbach, M. F. Glasser, M. Hernandez, G. Sapiro, M. Jenkinson, D. A. Feinberg, E. Yacoub, C. Lenglet,

D. C. Ven Essen, K. Ugurbil, and T. E. Behrens, "Advances in diffusion mri acquisition and processing in the human connectome project," *NeuroImage*, vol. 80, pp. 125–143, Oct. 2013.

[112] R. A. Poldrack, T. O. Laumann, O. Koyejo, B. Gregory, A. Hover, M.-Y. Chen, K. J. Gorgolewski, J. Luci, S. J. Joo, R. L. Boyd, S. Hunicke-Smith, Z. B. Simpson, T. Caven, V. Sochat, J. M. Shine, E. Gordon, A. Z. Snyder, B. Adeyemo, S. E. Petersen, D. C. Glahn, D. Reese Mckay, J. E. Curran, H. H. H. Göring, M. A. Carless, J. Blangero, R. Dougherty, A. Leemans, D. A. Handwerker, L. Frick, E. M. Marcotte, and J. A. Mumford, "Long-term neural and physiological phenotyping of a single human," *Nature Communications*, vol. 6, p. 8885, Dec. 2015.

[113] A. Khan, D. Hemachandra, and J. Kai, "Prepdwi (v0.0.7g)," June 2021.

[114] J. Veraart, D. S. Novikov, D. Christiaens, B. Ades-aron, J. Sijbers, and E. Fieremans, "Denoising of diffusion mri using random matrix theory," *NeuroImage*, vol. 142, pp. 394–406, Nov. 2016.

[115] J. Veraart, E. Fieremans, and D. S. Novikov, "Diffusion mri noise mapping using random matrix theory," *Magnetic Resonance in Medicine*, vol. 76, pp. 1582–1593, Nov. 2016.

[116] E. Kellner, B. Dhital, V. G. Kiselev, and M. Reisert, "Gibbs-ringing artifact removal based on local subvoxel-shifts," *Magnetic Resonance in Medicine*, vol. 76, pp. 1574–1581, Nov. 2016.

[117] J. L. R. Andersson, S. Skare, and J. Ashburner, "How to correct susceptibility distortions in spin-echo echo-planar images: application to diffusion tensor imaging," *NeuroImage*, vol. 20, pp. 870–888, Oct. 2003.

[118] S. M. Smith, M. Jenkinson, M. W. Woolrich, C. F. Beckmann, T. E. J. Behrens, H. Johansen-Berg, P. R. Bannister, M. De Luca, I. Drobnjak, D. E. Flitney, R. K. Niazy, J. Saunders, J. Vickers, Y. Zhang, N. De Stefano, J. M. Brady, and P. M. Matthews, "Advances in functional and structural mr image analysis and implementation as fsl," *NeuroImage*, vol. 23 Suppl 1, pp. S208–219, 2004.

[119] J. L. R. Andersson and S. N. Sotiropoulos, "An integrated approach to correction for off-resonance effects and subject movement in diffusion mr imaging," *NeuroImage*, vol. 125, pp. 1063–1078, Jan. 2016.

[120] T. Dhollander, D. Raffelt, and A. Connelly, "Unsupervised 3-tissue response function estimation from single-shell or multi-shell diffusion mr data without a co-registered t1 image," in *Proceedings of ISMRM Workshop on Breaking the Barriers of Diffusion MRI*, (Lisbon, Portugal), p. 5, June 2016.

[121] B. Jeurissen, J.-D. Tournier, T. Dhollander, A. Connelly, and J. Sijbers, "Multi-tissue constrained spherical deconvolution for improved analysis of multi-shell diffusion mri data," *NeuroImage*, vol. 103, pp. 411–426, Dec. 2014.

[122] D. Raffelt, J.-D. Tournier, J. Fripp, S. Crozier, A. Connelly, and O. Salvado, "Symmetric diffeomorphic registration of fibre orientation distributions," *NeuroImage*, vol. 56, pp. 1171–1180, June 2011.

[123] J.-D. Tournier, F. Calamante, and A. Connelly, "Improved probabilistic streamlines tractography by 2nd order integration over fibre orientation distributions," in *Proceedings of the International Society for Magnetic Resonance in Medicine*, (Stockholm, Sweden), p. 1670, May 2010.

[124] R. E. Smith, J.-D. Tournier, F. Calamante, and A. Connelly, "Sift: Spherical-deconvolution informed filtering of tractograms," *NeuroImage*, vol. 67, pp. 298–312, Feb. 2013.

[125] J. Veraart, J. Sijbers, S. Sunaert, A. Leemans, and B. Jeurissen, "Weighted linear least squares estimation of diffusion mri parameters: Strengths, limitations, and pitfalls," *NeuroImage*, vol. 81, pp. 335–346, Nov. 2013.

[126] U. von Luxburg, "A tutorial on spectral clustering," *Statistics and Computing*, vol. 17, pp. 395–416, Dec. 2007.

[127] E. Visser, E. H. J. Nijhuis, J. K. Buitelaar, and M. P. Zwiers, "Partition-based mass clustering of tractography streamlines," *NeuroImage*, vol. 54, pp. 303–312, Jan. 2011.

[128] V. Siless, S. Medina, G. Varoquaux, and B. Thirion, "A comparison of metrics and algorithms for fiber clustering," in *2013 International Workshop on Pattern Recognition in Neuroimaging*, pp. 190–193, June 2013.

[129] L. J. O'Donnell, Y. Suter, L. Rigolo, P. Kahali, F. Zhang, I. Norton, A. Albi, O. Olubiyi, A. Meola, W. I. Essayed, P. Unadkat, P. A. Ciris, W. M. Wells III, Y. Rathi, C.-F. Westin, and A. J. Golby, "Automated white matter fiber tract identification in patients with brain tumors," *NeuroImage: Clinical*, vol. 13, pp. 138–153, 2017.

[130] V. Siless, K. Chang, B. Fischl, and A. Yendiki, "Anatomicuts: Hierarchical clustering of tractography streamlines based on anatomical similarity," *NeuroImage*, vol. 166, pp. 32–45, 2018.

[131] A. Y. Ng, M. I. Jordan, and Y. Weiss, "On spectral clustering: Analysis and an algorithm," in *Advances in neural information processing systems*, (Cambridge), pp. 849–856, MIT Press, 2002.

[132] A. Brun, H.-J. Park, H. Knutsson, and C.-F. Westin, "Coloring of dt-mri fiber traces using laplacian eigenmaps," in *Proceedings of the Eurocast 2003, Neuro Image Workshop*, Lecture Notes in Computer Science, pp. 518–529, Springer Berlin Heidelberg, 2003.

[133] M. Cousineau, P.-M. Jodoin, E. Garyfallidis, M.-A. Côté, F. C. Morency, V. Rozanski, M. Grand'Maison, B. J. Bedell, and M. Descoteaux, "A test-retest study on parkinson's ppmi dataset yields statistically significant white matter fascicles," *NeuroImage: Clinical*, vol. 16, pp. 222–233, Jan. 2017.

[134] L. R. Dice, "Measures of the amount of ecologic association between species," *Ecology*, vol. 26, no. 3, pp. 297–302, 1945.

[135] M. Cousineau, M. Descoteaux, and H. Takemura, "Effect of different seeding strategies on tractometry reproducibility," in *International Society for Magnetic Resonance in Medicine*, vol. 2017, (Honolulu, HI, USA), Apr. 2017.

[136] K. O. McGraw and S. P. Wong, "Forming inferences about some intraclass correlation coefficients," *Psychological Methods*, vol. 1, pp. 30–46, Mar. 1996.

[137] Y. Benjamini and Y. Hochberg, "Controlling the false discovery rate: A practical and powerful approach to multiple testing," *Journal of the Royal Statistical Society: Series B (Methodological)*, vol. 57, no. 1, pp. 289–300, 1995.

[138] F. Rheault, A. D. Benedictis, A. Daducci, C. Maffei, C. M. W. Tax, D. Romascano, E. Caverzasi, F. C. Morency, F. Corrivetti, F. Pestilli, G. Girard, G. Theaud, I. Zemmoura, J. Hau, K. Glavin, K. M. Jordan, K. Pomiecko, M. Chamberland, M. Barakovic, N. Goyette, P. Poulin, Q. Chenot, S. S. Panesar, S. Sarubbo, L. Petit, and M. Descoteaux, "Tractostorm: The what, why, and how of tractography dissection reproducibility," *Human Brain Mapping*, vol. 41, no. 7, pp. 1859–1874, 2020.

[139] B. Q. Chandio, S. L. Risacher, F. Pestilli, D. Bullock, F.-C. Yeh, S. Koudoro, A. Rokem, J. Harezlak, and E. Garyfallidis, "Bundle analytics, a computational framework for investigating the shapes and profiles of brain pathways across populations," *Scientific Reports*, vol. 10, p. 17149, Oct. 2020.

[140] M. A. Kramer and S. S. Cash, "Epilepsy as a disorder of cortical network organization," *The Neuroscientist*, vol. 18, pp. 360–372, Aug. 2012.

[141] M. Rubinov and E. Bullmore, "Schizophrenia and abnormal brain network hubs," *Dialogues in Clinical Neuroscience*, vol. 15, pp. 339–349, Sept. 2013.

[142] O. Sporns, "The human connectome: a complex network: The human connectome," *Annals of the New York Academy of Sciences*, vol. 1224, pp. 109–125, Apr. 2011.

[143] A. W. Toga, K. A. Clark, P. M. Thompson, D. W. Shattuck, and J. D. Van Horn, "Mapping the Human Connectome," *Neurosurgery*, vol. 71, pp. 1–5, July 2012.

[144] K. Hua, J. Zhang, S. Wakana, H. Jiang, X. Li, D. S. Reich, P. A. Calabresi, J. J. Pekar, P. C. M. van Zijl, and S. Mori, "Tract probability maps in stereotaxic spaces: Analyses of white matter anatomy and tract-specific quantification," *NeuroImage*, vol. 39, pp. 336–347, Jan. 2008.

[145] S. Mori, S. Wakana, P. C. M. v. Zijl, and L. M. Nagae-Poetscher, *MRI Atlas of Human White Matter*. Elsevier, May 2005.

[146] T. E. J. Behrens, M. W. Woolrich, M. Jenkinson, H. Johansen-Berg, R. G. Nunes, S. Clare, P. M. Matthews, J. M. Brady, and S. M. Smith, "Characterization and propagation of uncertainty in diffusion-weighted MR imaging," *Magnetic Resonance in Medicine*, vol. 50, pp. 1077–1088, Nov. 2003.

[147] S. Delli Pizzi, R. Franciotti, J.-P. Taylor, A. Thomas, A. Tartaro, M. Onofrj, and L. Bonanni, "Thalamic involvement in fluctuating cognition in dementia with lewy bodies: Magnetic resonance evidences," *Cerebral Cortex*, vol. 25, pp. 3682–3689, Oct. 2015.

[148] D. F. Siwek and D. N. Pandya, "Prefrontal projections to the mediodorsal nucleus of the thalamus in the rhesus monkey," *Journal of Comparative Neurology*, vol. 312, no. 4, pp. 509–524, 1991.

[149] E. H. Yeterian and D. N. Pandya, "Prefrontostriatal connections in relation to cortical architectonic organization in rhesus monkeys," *Journal of Comparative Neurology*, vol. 312, no. 1, pp. 43–67, 1991.

[150] E. H. Yeterian and D. N. Pandya, "Striatal connections of the parietal association cortices in rhesus monkeys," *Journal of Comparative Neurology*, vol. 332, no. 2, pp. 175–197, 1993.

[151] M. R. DeLong and T. Wichmann, "Circuits and circuit disorders of the basal ganglia," *Archives of Neurology*, vol. 64, pp. 20–24, Jan. 2007.

[152] G. E. Alexander, M. R. DeLong, and P. L. Strick, "Parallel organization of functionally segregated circuits linking basal ganglia and cortex," *Annual Review of Neuroscience*, vol. 9, pp. 357–381, 1986.

[153] F. A. Middleton and P. L. Strick, "Basal ganglia and cerebellar loops: motor and cognitive circuits," *Brain Research Reviews*, vol. 31, pp. 236–250, Mar. 2000.

[154] Y. Smith, M. Bevan, E. Shink, and J. P. Bolam, "Microcircuitry of the direct and indirect pathways of the basal ganglia.," *Neuroscience*, vol. 86, no. 2, pp. 353–387, 1998.

[155] S. N. Haber, E. Lynd-Balta, and S. J. Mitchell, "The organization of the descending ventral pallidal projections in the monkey," *Journal of Comparative Neurology*, vol. 329, no. 1, pp. 111–128, 1993.

[156] C. Lenglet, A. Abosch, E. Yacoub, F. D. Martino, G. Sapiro, and N. Harel, "Comprehensive in vivo mapping of the human basal ganglia and thalamic connectome in individuals using 7t mri," *PLOS ONE*, vol. 7, p. e29153, Jan. 2012.

[157] C. R. Buchanan, C. R. Pernet, K. J. Gorgolewski, A. J. Storkey, and M. E. Bastin, "Test–retest reliability of structural brain networks from diffusion mri," *NeuroImage*, vol. 86, pp. 231–243, Feb. 2014.

[158] K. G. Schilling, F. Rheault, L. Petit, C. B. Hansen, V. Nath, F.-C. Yeh, G. Girard, M. Barakovic, J. Rafael-Patino, T. Yu, E. Fischi-Gomez, M. Pizzolato, M. Ocampo-Pineda, S. Schiavi, E. J. Canales-Rodríguez, A. Daducci, C. Granziera, G. Innocenti, J.-P. Thiran, L. Mancini, S. Wastling, S. Cocozza, M. Petracca, G. Pontillo, M. Mancini, S. B. Vos, V. N. Vakharia, J. S. Duncan, H. Melero, L. Manzanedo, E. Sanz-Morales, A. Peña Melián, F. Calamante, A. Attyé, R. P. Cabeen, L. Korobova, A. W. Toga, A. A. Vijayakumari, D. Parker, R. Verma, A. Radwan, S. Sunaert, L. Emsell, A. De Luca,

A. Leemans, C. J. Bajada, H. Haroon, H. Azadbakht, M. Chamberland, S. Genc, C. M. W. Tax, P.-H. Yeh, R. Srikanchana, C. D. Mcknight, J. Y.-M. Yang, J. Chen, C. E. Kelly, C.-H. Yeh, J. Cochereau, J. J. Maller, T. Welton, F. Almairac, K. K. Seunarine, C. A. Clark, F. Zhang, N. Makris, A. Golby, Y. Rathi, L. J. O'Donnell, Y. Xia, D. B. Aydogan, Y. Shi, F. G. Fernandes, M. Raemaekers, S. Warrington, S. Michielse, A. Ramírez-Manzanares, L. Concha, R. Aranda, M. R. Meraz, G. Lerma-Usabiaga, L. Roitman, L. S. Fekonja, N. Calarco, M. Joseph, H. Nakua, A. N. Voineskos, P. Karan, G. Grenier, J. H. Legarreta, N. Adluru, V. A. Nair, V. Prabhakaran, A. L. Alexander, K. Kamagata, Y. Saito, W. Uchida, C. Andica, M. Abe, R. G. Bayrak, C. A. M. G. Wheeler-Kingshott, E. D'Angelo, F. Palesi, G. Savini, N. Rolandi, P. Guevara, J. Houenou, N. López-López, J.-F. Mangin, C. Poupon, C. Román, A. Vázquez, C. Maffei, M. Arantes, J. P. Andrade, S. M. Silva, V. D. Calhoun, E. Caverzasi, S. Sacco, M. Lauricella, F. Pestilli, D. Bullock, Y. Zhan, E. Brignoni-Perez, C. Lebel, J. E. Reynolds, I. Nestrasil, R. Labounek, C. Lenglet, A. Paulson, S. Aulicka, S. R. Heilbronner, K. Heuer, B. Q. Chandio, J. Guaje, W. Tang, E. Garyfallidis, R. Raja, A. W. Anderson, B. A. Landman, and M. Descoteaux, "Tractography dissection variability: What happens when 42 groups dissect 14 white matter bundles on the same dataset?," *NeuroImage*, vol. 243, p. 118502, Nov. 2021.

[159] J. P. Mugler and J. R. Brookeman, "Three-dimensional magnetization-prepared rapid gradient-echo imaging (3D MP RAGE)," *Magnetic Resonance in Medicine*, vol. 15, no. 1, pp. 152–157, 1990.

[160] J. E. Iglesias, R. Insausti, G. Lerma-Usabiaga, M. Bocchetta, K. Van Leemput, D. N. Greve, A. van der Kouwe, B. Fischl, C. Caballero-Gaudes, and P. M. Paz-Alonso, "A probabilistic atlas of the human thalamic nuclei combining ex vivo mri and histology," *NeuroImage*, vol. 183, pp. 314–326, Dec. 2018.

[161] J. DeKraker, J. C. Lau, K. M. Ferko, A. R. Khan, and S. Köhler, "Hippocampal subfields revealed through unfolding and unsupervised clustering of laminar and morphological features in 3d bigbrain," *NeuroImage*, vol. 206, p. 116328, Feb. 2020.

[162] H. M. Duvernoy, *The Human Hippocampus: An Atlas of Applied Anatomy*. J.F. Bergmann-Verlag, Mar. 2013.

[163] Y. Xiao, J. C. Lau, T. Anderson, J. DeKraker, D. L. Collins, T. Peters, and A. R. Khan, "An accurate registration of the BigBrain dataset with the MNI PD25 and ICBM152 atlases," *Scientific Data*, vol. 6, p. 210, Oct. 2019.

[164] V. Fonov, A. C. Evans, K. Botteron, C. R. Almli, R. C. McKinstry, and D. L. Collins, "Unbiased average age-appropriate atlases for pediatric studies," *NeuroImage*, vol. 54, pp. 313–327, Jan. 2011.

[165] B. B. Avants, N. Tustison, and H. Johnson, "Advanced normalization tools (ants)," *Insight Journal*, vol. 2, pp. 1–35, June 2009.

[166] D. Raffelt, J.-D. Tournier, S. Rose, G. R. Ridgway, R. Henderson, S. Crozier, O. Salvado, and A. Connelly, "Apparent Fibre Density: a novel measure for the analysis of diffusion-weighted magnetic resonance images," *NeuroImage*, vol. 59, pp. 3976–3994, Feb. 2012.

[167] D. Raffelt, T. Dhollander, J.-D. Tournier, R. Tabbara, R. E. Smith, E. Pierre, and A. Connelly, "Bias field correction and intensity normalisation for quantitative analysis of apparent fibre density," in *Proc. Intl. Soc. Mag. Reson. Med*, vol. 25, p. 3541, 2017.

[168] R. E. Smith, J.-D. Tournier, F. Calamante, and A. Connelly, "Sift2: Enabling dense quantitative assessment of brain white matter connectivity using streamlines tractography," *NeuroImage*, vol. 119, pp. 338–351, Oct. 2015.

[169] B. A. Kreilkamp, L. Lisanti, G. R. Glenn, U. C. Wieshmann, K. Das, A. G. Marson, and S. S. Keller, "Comparison of manual and automated fiber quantification tractography in patients with temporal lobe epilepsy," *NeuroImage : Clinical*, vol. 24, p. 102024, Oct. 2019.

[170] K. Shadi, S. Bakhshi, D. A. Gutman, H. S. Mayberg, and C. Dovrolis, "A Symmetry-Based Method to Infer Structural Brain Networks from Probabilistic Tractography Data," *Frontiers in Neuroinformatics*, vol. 10, p. 46, 2016.

[171] Z. Zhang, M. Descoteaux, J. Zhang, G. Girard, M. Chamberland, D. Dunson, A. Srivastava, and H. Zhu, "Mapping population-based structural connectomes," *NeuroImage*, vol. 172, pp. 130–145, May 2018.

[172] Y. Li, Y. Liu, J. Li, W. Qin, K. Li, C. Yu, and T. Jiang, "Brain Anatomical Network and Intelligence," *PLOS Computational Biology*, vol. 5, p. e1000395, May 2009.

[173] L. Li, J. K. Rilling, T. M. Preuss, M. F. Glasser, and X. Hu, "The effects of connection reconstruction method on the interregional connectivity of brain networks via diffusion tractography," *Human Brain Mapping*, vol. 33, no. 8, pp. 1894–1913, 2012.

[174] A. Parent and M. B. Carpenter, *Carpenter's Human Neuroanatomy*. Williams & Wilkins, 1996.

[175] F. Sato, P. Lavallée, M. Lévesque, and A. Parent, "Single-axon tracing study of neurons of the external segment of the globus pallidus in primate," *Journal of Comparative Neurology*, vol. 417, no. 1, pp. 17–31, 2000.

[176] F. Sato, M. Parent, M. Levesque, and A. Parent, "Axonal branching pattern of neurons of the subthalamic nucleus in primates," *Journal of Comparative Neurology*, vol. 424, no. 1, pp. 142–152, 2000.

[177] S. N. Haber, A. Yendiki, and S. Jbabdi, "Four deep brain stimulation targets for obsessive-compulsive disorder: Are they different?," *Biological Psychiatry*, vol. 90, pp. 667–677, Nov. 2021.

[178] T. Tsuboi, J. K. Wong, R. S. Eisinger, L. Okromelidze, M. R. Burns, A. Ramirez-Zamora, L. Almeida, A. Wagle Shukla, K. D. Foote, M. S. Okun, S. S. Grewal, and E. H. Middlebrooks, "Comparative connectivity correlates of dystonic and essential tremor deep brain stimulation," *Brain*, vol. 144, pp. 1774–1786, June 2021.

[179] A. Abos, H. C. Baggio, B. Segura, A. Campabadal, C. Uribe, D. M. Giraldo, A. Perez-Soriano, E. Muñoz, Y. Compta, C. Junque, and M. J. Marti, "Differentiation of multiple system atrophy from Parkinson's disease by structural connectivity derived from probabilistic tractography," *Scientific Reports*, vol. 9, p. 16488, Nov. 2019.

[180] C. Karachi, J. Yelnik, D. Tandé, L. Tremblay, E. C. Hirsch, and C. François, "The pallidosubthalamic projection: An anatomical substrate for nonmotor functions of the subthalamic nucleus in primates," *Movement Disorders*, vol. 20, no. 2, pp. 172–180, 2005.

[181] M. D. Johnson, S. Miocinovic, C. C. McIntyre, and J. L. Vitek, "Mechanisms and targets of deep brain stimulation in movement disorders," *Neurotherapeutics*, vol. 5, pp. 294–308, Apr. 2008.

[182] L. Cammoun, X. Gigandet, D. Meskaldji, J. P. Thiran, O. Sporns, K. Q. Do, P. Maeder, R. Meuli, and P. Hagmann, "Mapping the human connectome at multiple scales with diffusion spectrum mri," *Journal of Neuroscience Methods*, vol. 203, pp. 386–397, Jan. 2012.

[183] M. Boukadi, K. Marcotte, C. Bedetti, J.-C. Houde, A. Desautels, S. Deslauriers-Gauthier, M. Chapleau, A. Boré, M. Descoteaux, and S. M. Brambati, "Test-retest reliability of diffusion measures extracted along white matter language fiber bundles using hardi-based tractography," *Frontiers in Neuroscience*, vol. 12, p. 1055, 2019.

[184] J. C. Lau, Y. Xiao, R. A. M. Haast, G. Gilmore, K. Uludağ, K. W. MacDougall, R. S. Menon, A. G. Parrent, T. M. Peters, and A. R. Khan, "Direct visualization and characterization of the human zona incerta and surrounding structures," *Human Brain Mapping*, vol. 41, no. 16, pp. 4500–4517, 2020.

[185] A. R. Khan, N. M. Hiebert, A. Vo, B. T. Wang, A. M. Owen, K. N. Seergobin, and P. A. MacDonald, "Biomarkers of Parkinson's disease: Striatal sub-regional structural morphometry and diffusion MRI," *NeuroImage: Clinical*, vol. 21, p. 101597, Jan. 2019.

[186] A. C. Tziortzi, S. N. Haber, G. E. Searle, C. Tsoumpas, C. J. Long, P. Shotbolt, G. Douaud, S. Jbabdi, T. E. J. Behrens, E. A. Rabiner, M. Jenkinson, and R. N. Gunn, "Connectivity-based functional analysis of dopamine release in the striatum using diffusion-weighted MRI and positron emission tomography," *Cerebral Cortex (New York, N.Y.: 1991)*, vol. 24, pp. 1165–1177, May 2014.

[187] Y. Tian, D. S. Margulies, M. Breakspear, and A. Zalesky, "Topographic organization of the human subcortex unveiled with functional connectivity gradients," *Nature Neuroscience*, vol. 23, pp. 1421–1432, Nov. 2020.

[188] S. Arslan, S. I. Ktena, A. Makropoulos, E. C. Robinson, D. Rueckert, and S. Parisot, "Human brain mapping: A systematic comparison of parcellation methods for the human cerebral cortex," *NeuroImage*, vol. 170, pp. 5–30, Apr. 2018.

[189] D. Wassermann, N. Makris, Y. Rathi, M. Shenton, R. Kikinis, M. Kubicki, and C.-F. Westin, "The white matter query language: a novel approach for describing human white matter anatomy," *Brain Structure and Function*, vol. 221, pp. 4705–4721, Dec. 2016.

[190] G. Grisot, S. N. Haber, and A. Yendiki, "Diffusion mri and anatomic tracing in the same brain reveal common failure modes of tractography," *NeuroImage*, vol. 239, p. 118300, Oct. 2021.

[191] M. Takada, K. Itoh, Y. Yasui, T. Sugimoto, and N. Mizuno, "Topographical projections from the posterior thalamic regions to the striatum in the cat, with reference to possible tecto-thalamo-striatal connections," *Experimental Brain Research*, vol. 60, pp. 385–396, Oct. 1985.

[192] A. M. McIntosh, S. M. Maniega, G. K. S. Lymer, J. McKirdy, J. Hall, J. E. D. Sussmann, M. E. Bastin, J. D. Clayden, E. C. Johnstone, and S. M. Lawrie, "White Matter Tractography in Bipolar Disorder and Schizophrenia," *Biological Psychiatry*, vol. 64, pp. 1088–1092, Dec. 2008.

[193] A. Mubarik and H. Tohid, "Frontal lobe alterations in schizophrenia: a review," *Trends in Psychiatry and Psychotherapy*, vol. 38, pp. 198–206, Dec. 2016.

[194] I. Ellison-Wright and E. Bullmore, "Meta-analysis of diffusion tensor imaging studies in schizophrenia," *Schizophrenia Research*, vol. 108, pp. 3–10, Mar. 2009.

[195] H. B. Sarnat, W. Hader, L. Flores-Sarnat, and L. Bello-Espinosa, "Synaptic plexi of U-fibre layer beneath focal cortical dysplasias: Role in epileptic networks.," *Clinical neuropathology*, vol. 37, no. 6, pp. 262–276, 2018.

[196] S. K. Sundaram, A. Kumar, M. I. Makki, M. E. Behen, H. T. Chugani, and D. C. Chugani, "Diffusion tensor imaging of frontal lobe in autism spectrum disorder," *Cerebral Cortex*, vol. 18, pp. 2659–2665, Nov. 2008.

[197] A. M. Butt and M. Berry, "Oligodendrocytes and the control of myelination in vivo: new insights from the rat anterior medullary velum," *Journal of Neuroscience Research*, vol. 59, no. 4, pp. 477–488, 2000.

[198] V. Haroutunian, P. Katsel, P. Roussos, K. L. Davis, L. L. Altshuler, and G. Bartzokis, "Myelination, oligodendrocytes, and serious mental illness," *Glia*, vol. 62, no. 11, pp. 1856–1877, 2014.

[199] P. M. Thompson, C. Schwartz, R. T. Lin, A. A. Khan, and A. W. Toga, "Three-Dimensional Statistical Analysis of Sulcal Variability in the Human Brain," *Journal of Neuroscience*, vol. 16, pp. 4261–4274, July 1996.

[200] J. Kai and A. R. Khan, "Assessing the Reliability of Template-Based Clustering for Tractography in Healthy Human Adults," *Frontiers in Neuroinformatics*, vol. 16, 2022.

[201] V. Menon and M. D'Esposito, "The role of PFC networks in cognitive control and executive function," *Neuropsychopharmacology*, vol. 47, pp. 90–103, Jan. 2022.

[202] J. Fessel, "Abnormal oligodendrocyte function in schizophrenia explains the long latent interval in some patients," *Translational Psychiatry*, vol. 12, pp. 1–8, Mar. 2022.

[203] M. F. Alonso-Sánchez, S. D. Ford, M. MacKinley, A. Silva, R. Limongi, and L. Palaniyappan, "Progressive changes in descriptive discourse in First Episode Schizophrenia: a longitudinal computational semantics study," *Schizophrenia*, vol. 8, pp. 1–9, Apr. 2022.

[204] K. Dempster, P. Jeon, M. MacKinley, P. Williamson, J. Théberge, and L. Palaniyappan, "Early treatment response in first episode psychosis: a 7-T magnetic resonance spectroscopic study of glutathione and glutamate," *Molecular Psychiatry*, vol. 25, pp. 1640–1650, Aug. 2020.

[205] R. Limongi, P. Jeon, M. Mackinley, T. Das, K. Dempster, J. Théberge, R. Bartha, D. Wong, and L. Palaniyappan, "Glutamate and Dysconnection in the Salience Network: Neurochemical, Effective Connectivity, and Computational Evidence in Schizophrenia," *Biological Psychiatry*, vol. 88, pp. 273–281, Aug. 2020.

[206] C.-H. Lin, H.-S. Lin, S.-C. Lin, C.-C. Kuo, F.-C. Wang, and Y.-H. Huang, "Early improvement in PANSS-30, PANSS-8, and PANSS-6 scores predicts ultimate response and remission during acute treatment of schizophrenia," *Acta Psychiatrica Scandinavica*, vol. 137, no. 2, pp. 98–108, 2018.

[207] W. Guy, *ECDEU assessment manual for psychopharmacology*. US Department of Health, Education, and Welfare, Public Health Service . . . , 1976.

[208] P. L. Morosini, L. Magliano, L. Brambilla, S. Ugolini, and R. Pioli, "Development, reliability and acceptability of a new version of the DSM-IV Social and Occupational Functioning Assessment Scale (SOFAS) to assess routine social functioning," *Acta Psychiatrica Scandinavica*, vol. 101, pp. 323–329, Apr. 2000.

[209] J. P. Marques, T. Kober, G. Krueger, W. van der Zwaag, P.-F. Van de Moortele, and R. Gruetter, "MP2RAGE, a self bias-field corrected sequence for improved segmentation and T1-mapping at high field," *NeuroImage*, vol. 49, pp. 1271–1281, Jan. 2010.

[210] O. Esteban, C. J. Markiewicz, R. W. Blair, C. A. Moodie, A. I. Isik, A. Erramuzpe, J. D. Kent, M. Goncalves, E. DuPre, M. Snyder, H. Oya, S. S. Ghosh, J. Wright, J. Durnez, R. A. Poldrack, and K. J. Gorgolewski, "fMRIPrep: a robust preprocessing pipeline for functional MRI," *Nature Methods*, vol. 16, pp. 111–116, Jan. 2019.

[211] O. Esteban, C. J. Markiewicz, E. DuPre, M. Goncalves, J. D. Kent, R. Ciric, R. W. Blair, R. A. Poldrack, and K. J. Gorgolewski, "fMRIPrep: a robust preprocessing pipeline for functional MRI," Mar. 2020.

[212] A. M. Dale, B. Fischl, and M. I. Sereno, "Cortical surface-based analysis. I. Segmentation and surface reconstruction," *NeuroImage*, vol. 9, pp. 179–194, Feb. 1999.

[213] R. S. Desikan, F. Ségonne, B. Fischl, B. T. Quinn, B. C. Dickerson, D. Blacker, R. L. Buckner, A. M. Dale, R. P. Maguire, B. T. Hyman, M. S. Albert, and R. J. Killiany, "An automated labeling system for subdividing the human cerebral cortex on mri scans into gyral based regions of interest," *NeuroImage*, vol. 31, pp. 968–980, July 2006.

[214] A. Schaefer, R. Kong, E. M. Gordon, T. O. Laumann, X.-N. Zuo, A. J. Holmes, S. B. Eickhoff, and B. T. T. Yeo, "Local-Global Parcellation of the Human Cerebral Cortex from Intrinsic Functional Connectivity MRI," *Cerebral Cortex*, vol. 28, pp. 3095–3114, Sept. 2018.

[215] B. L. Welch, "The Generalization of 'Students' Problem When Seveveral Difference Population Variances Are Involved," *Biometrika*, vol. 34, pp. 28–35, Jan. 1947.

[216] T. E. Nichols and A. P. Holmes, "Nonparametric permutation tests for functional neuroimaging: A primer with examples," *Human Brain Mapping*, vol. 15, pp. 1–25, Jan. 2002.

[217] J. B. Colby, L. Soderberg, C. Lebel, I. D. Dinov, P. M. Thompson, and E. R. Sowell, "Along-tract statistics allow for enhanced tractography analysis," *NeuroImage*, vol. 59, pp. 3227–3242, Feb. 2012.

[218] J. Wasserthal, K. H. Maier-Hein, P. F. Neher, G. Northoff, K. M. Kubera, S. Fritze, A. Harneit, L. S. Geiger, H. Tost, R. C. Wolf, and D. Hirjak, "Multiparametric mapping of white matter microstructure in catatonia," *Neuropsychopharmacology*, vol. 45, pp. 1750–1757, Sept. 2020.

[219] A. Nazeri, M. M. Chakravarty, D. Felsky, N. J. Lobaugh, T. K. Rajji, B. H. Mulsant, and A. N. Voineskos, "Alterations of Superficial White Matter in Schizophrenia and Relationship to Cognitive Performance," *Neuropsychopharmacology*, vol. 38, pp. 1954–1962, Sept. 2013.

[220] O. R. Phillips, K. H. Nuechterlein, R. F. Asarnow, K. A. Clark, R. Cabeen, Y. Yang, R. P. Woods, A. W. Toga, and K. L. Narr, "Mapping Corticocortical Structural Integrity in Schizophrenia and Effects of Genetic Liability," *Biological Psychiatry*, vol. 70, pp. 680–689, Oct. 2011.

[221] A. L. MacKay and C. Laule, "Magnetic resonance of myelin water: an in vivo marker for myelin," *Brain plasticity*, vol. 2, no. 1, pp. 71–91, 2016.

[222] M. Ouyang, H. Kang, J. A. Detre, T. P. Roberts, and H. Huang, "Short-range connections in the developmental connectome during typical and atypical brain maturation," *Neuroscience and biobehavioral reviews*, vol. 83, pp. 109–122, Dec. 2017.

[223] M. Yoshino, K. Saito, K. Kawasaki, T. Horiike, Y. Shinmyo, and H. Kawasaki, "The origin and development of subcortical U-fibers in gyrencephalic ferrets," *Molecular Brain*, vol. 13, p. 37, Mar. 2020.

[224] Y. Jiang, C. Luo, X. Li, Y. Li, H. Yang, J. Li, X. Chang, H. Li, H. Yang, J. Wang, M. Duan, and D. Yao, "White-matter functional networks changes in patients with schizophrenia," *NeuroImage*, vol. 190, pp. 172–181, Apr. 2019.

[225] N. V. Kraguljac, D. M. White, J. A. Hadley, K. Visscher, D. Knight, L. ver Hoef, B. Falola, and A. C. Lahti, "Abnormalities in large scale functional networks in unmedicated patients with schizophrenia and effects of risperidone," *NeuroImage: Clinical*, vol. 10, pp. 146–158, Jan. 2016.

[226] D. R. Weinberger, K. F. Berman, and R. F. Zec, "Physiologic dysfunction of dorsolateral prefrontal cortex in schizophrenia: I. Regional cerebral blood flow evidence," *Archives of general psychiatry*, vol. 43, no. 2, pp. 114–124, 1986.

[227] T. A. Hummer, M. G. Yung, J. Goñi, S. K. Conroy, M. M. Francis, N. F. Mehdiyoun, and A. Breier, "Functional network connectivity in early-stage schizophrenia," *Schizophrenia Research*, vol. 218, pp. 107–115, Apr. 2020.

[228] G. Mingoia, G. Wagner, K. Langbein, R. Maitra, S. Smesny, M. Dietzek, H. P. Burmeister, J. R. Reichenbach, R. G. M. Schlösser, C. Gaser, H. Sauer, and I. Nenadic, "Default mode network activity in schizophrenia studied at resting state using probabilistic ICA," *Schizophrenia Research*, vol. 138, pp. 143–149, July 2012.

[229] W. Byne, A. Tatusov, G. Yiannoulos, G. S. Vong, and S. Marcus, "Effects of mental illness and aging in two thalamic nuclei," *Schizophrenia Research*, vol. 106, pp. 172–181, Dec. 2008.

[230] P. R. Hof, V. Haroutunian, V. L. Friedrich, W. Byne, C. Buitron, D. P. Perl, and K. L. Davis, "Loss and altered spatial distribution of oligodendrocytes in the superior frontal gyrus in schizophrenia," *Biological Psychiatry*, vol. 53, pp. 1075–1085, June 2003.

[231] M. I. Mighdoll, R. Tao, J. E. Kleinman, and T. M. Hyde, "Myelin, myelin-related disorders, and psychosis," *Schizophrenia Research*, vol. 161, pp. 85–93, Jan. 2015.

[232] A. K. Stark, H. B. Uylings, E. Sanz-Arigita, and B. Pakkenberg, "Glial Cell Loss in the Anterior Cingulate Cortex, a Subregion of the Prefrontal Cortex, in Subjects With Schizophrenia," *American Journal of Psychiatry*, vol. 161, pp. 882–888, May 2004.

[233] D. A. Maas, A. Vallès, and G. J. M. Martens, "Oxidative stress, prefrontal cortex hypomyelination and cognitive symptoms in schizophrenia," *Translational Psychiatry*, vol. 7, pp. e1171–e1171, July 2017.

[234] N. A. Uranova, O. V. Vikhreva, V. I. Rachmanova, and D. D. Orlovskaya, "Ultrastructural Alterations of Myelinated Fibers and Oligodendrocytes in the Prefrontal Cortex in Schizophrenia: A Postmortem Morphometric Study," *Schizophrenia Research and Treatment*, vol. 2011, p. e325789, June 2011.

[235] W. Y. Aung, S. Mar, and T. L. Benzinger, "Diffusion tensor MRI as a biomarker in axonal and myelin damage," *Imaging in medicine*, vol. 5, pp. 427–440, Oct. 2013.

[236] P. Mäki, J. Veijola, P. B. Jones, G. K. Murray, H. Koponen, P. Tienari, J. Miettunen, P. Tanskanen, K.-E. Wahlberg, J. Koskinen, E. Lauronen, and M. Isohanni, "Predictors of schizophrenia—a review," *British Medical Bulletin*, vol. 73-74, pp. 1–15, Jan. 2005.

[237] S. A. Stilo and R. M. Murray, "Non-Genetic Factors in Schizophrenia," *Current Psychiatry Reports*, vol. 21, p. 100, Sept. 2019.

[238] D. Shastin, S. Genc, G. D. Parker, K. Koller, C. M. W. Tax, J. Evans, K. Hamandi, W. P. Gray, D. K. Jones, and M. Chamberland, "Surface-based tracking for short association fibre tractography," *NeuroImage*, vol. 260, p. 119423, Oct. 2022.

Appendix A

Chapter 2 Supplementary Material

A.1 Supplementary table 1

Table S1. Evaluated metrics for all clusters across the two datasets using two different clustering techniques. Datasets evaulated with QuickBundles are identified by the suffix "QB". Tracts with at least one subject or session failing to cluster are indicated by the missing evaluation.

Dataset	Label	Euclidean Distance [mm] (avg ±sd)	Streamline Count (avg ±sd) [cv]	wDSC - Clusters (avg ±sd)	ICC [95% CI]
MyConnectome	0	1.071 ±0.849	2988 ±972 [32.534]	0.925 ±0.032	0.947 [0.90, 0.98]
MyConnectome	1	0.979 ±0.561	883 ±318 [36.022]	0.910 ±0.052	0.868 [0.77, 0.94]
MyConnectome	2	0.915 ±0.627	2108 ±844 [40.028]	0.909 ±0.044	0.954 [0.90, 0.98]
MyConnectome	3	3.627 ±2.123	624 ±367 [58.754]	0.622 ±0.125	0.960 [0.93, 0.98]
MyConnectome	4	1.752 ±1.216	3687 ±1682 [45.634]	0.920 ±0.035	0.879 [0.76, 0.95]
MyConnectome	5	1.932 ±1.532	3261 ±1024 [31.399]	0.859 ±0.080	0.767 [0.59, 0.89]
MyConnectome	6	-	-	-	-
MyConnectome	7	1.017 ±1.083	1419 ±547 [38.551]	0.897 ±0.050	0.913 [0.82, 0.96]
MyConnectome	8	4.268 ±3.407	4676 ±1615 [34.537]	0.911 ±0.038	0.674 [0.44, 0.84]
MyConnectome	9	3.137 ±1.466	882 ±806 [91.436]	0.642 ±0.106	0.803 [0.65, 0.91]
MyConnectome	10	1.437 ±1.785	5341 ±810 [15.169]	0.942 ±0.022	0.814 [0.66, 0.91]
MyConnectome	11	2.136 ±1.351	2921 ±1307 [44.753]	0.890 ±0.086	0.872 [0.73, 0.95]
MyConnectome	12	1.156 ±0.801	1932 ±901 [46.640]	0.918 ±0.049	0.972 [0.95, 0.99]
MyConnectome	13	2.833 ±1.865	4461 ±1887 [42.298]	0.829 ±0.087	0.259 [0.12, 0.47]
MyConnectome	14	1.785 ±1.136	996 ±535 [53.682]	0.842 ±0.100	0.943 [0.87, 0.98]
MyConnectome	15	1.088 ±0.969	2069 ±829 [40.059]	0.918 ±0.060	0.945 [0.88, 0.98]
MyConnectome	16	1.640 ±1.590	886 ±368 [41.513]	0.842 ±0.079	0.737 [0.55, 0.87]
MyConnectome	17	4.657 ±2.152	169 ±199 [118.000]	0.334 ±0.206	0.292 [0.16, 0.49]
MyConnectome	18	1.569 ±1.097	2357 ±885 [37.569]	0.837 ±0.061	0.725 [0.56, 0.86]
MyConnectome	19	3.918 ±2.090	1191 ±649 [54.479]	0.721 ±0.121	0.573 [0.36, 0.77]
MyConnectome	20	0.975 ±1.166	1983 ±698 [35.217]	0.930 ±0.047	0.953 [0.89, 0.98]
MyConnectome	21	1.622 ±1.180	1246 ±701 [56.246]	0.869 ±0.073	0.878 [0.74, 0.95]
MyConnectome	22	2.103 ±3.036	788 ±172 [21.872]	0.833 ±0.075	0.882 [0.77, 0.95]
MyConnectome	23	3.130 ±2.335	3162 ±1867 [59.037]	0.760 ±0.120	0.381 [0.19, 0.61]
MyConnectome	24	2.854 ±1.381	784 ±518 [66.114]	0.714 ±0.120	0.960 [0.93, 0.98]
MyConnectome	25	0.863 ±0.555	590 ±270 [45.770]	0.876 ±0.073	0.904 [0.83, 0.96]
MyConnectome	26	1.066 ±0.671	425 ±160 [37.565]	0.790 ±0.074	0.990 [0.98, 1.00]
MyConnectome	27	3.218 ±1.296	503 ±276 [54.891]	0.702 ±0.105	0.871 [0.74, 0.94]
MyConnectome	28	2.163 ±1.604	1883 ±611 [32.433]	0.922 ±0.024	0.931 [0.85, 0.97]
MyConnectome	29	3.810 ±1.739	988 ±1018 [103.097]	0.599 ±0.163	0.300 [0.14, 0.52]
MyConnectome	30	8.539 ±4.894	1744 ±1419 [81.393]	0.637 ±0.135	0.294 [0.14, 0.51]
MyConnectome	31	2.290 ±1.151	630 ±350 [55.622]	0.723 ±0.089	0.975 [0.96, 0.99]
MyConnectome	32	1.940 ±1.028	1284 ±842 [65.607]	0.751 ±0.105	0.736 [0.54, 0.87]
MyConnectome	33	2.031 ±1.928	1714 ±828 [48.309]	0.840 ±0.097	0.896 [0.79, 0.95]

A.2 Supplementary table 2

Table S2. Evaluated metrics and connectivity for all "U"-shaped clusters across the two datasets using spectral clustering, excluding cerebellar clusters. Lobular connectivity identified via Freesurfer parcellations, with hemispheres indicated by "R" or "L" for right and left hemispheres respectively. Tracts with at least one subject or session failing to cluster are indicated by the missing evaluation.

Dataset	Label	Euclidean Distance [mm] (avg ±sd)	Streamline Count (avg ±sd) [cv]	wDSC - Clusters (avg ±sd)	ICC [95% CI]	Connectivity
MyConnectome	0	2.051 ±0.378	254 ±88 [34.544]	0.869 ±0.050	0.977 [0.95, 0.99]	R Frontal - R Parietal
MyConnectome	1	2.658 ±0.510	129 ±44 [33.957]	0.688 ±0.061	0.971 [0.95, 0.99]	L Frontal - L Frontal
MyConnectome	2	1.741 ±0.387	254 ±77 [30.477]	0.785 ±0.072	0.987 [0.98, 0.99]	L Frontal - L Frontal
MyConnectome	3	6.722 ±3.240	618 ±135 [21.758]	0.679 ±0.066	0.974 [0.95, 0.99]	R Frontal - R Temporal
MyConnectome	4	1.896 ±0.494	165 ±65 [39.463]	0.813 ±0.062	0.969 [0.94, 0.99]	R Frontal - R Frontal
MyConnectome	5	2.221 ±0.791	352 ±72 [20.323]	0.832 ±0.051	0.989 [0.98, 1.00]	L Occipital - L Occipital
MyConnectome	6	2.614 ±0.576	219 ±82 [37.290]	0.772 ±0.068	0.968 [0.94, 0.99]	R Frontal - R Frontal
MyConnectome	7	2.109 ±0.341	94 ±31 [33.177]	0.779 ±0.052	0.976 [0.96, 0.99]	L Parietal - L Parietal
MyConnectome	8	2.892 ±0.502	183 ±58 [31.779]	0.751 ±0.058	0.972 [0.95, 0.99]	L Frontal - L Frontal
MyConnectome	9	2.758 ±0.389	280 ±136 [48.579]	0.868 ±0.063	0.983 [0.97, 0.99]	R Frontal - R Frontal
MyConnectome	10	3.083 ±0.580	94 ±25 [26.235]	0.781 ±0.042	0.989 [0.98, 1.00]	L Parietal - L Parietal
MyConnectome	11	2.687 ±0.552	72 ±22 [29.799]	0.718 ±0.066	0.972 [0.95, 0.99]	L Parietal - L Parietal
MyConnectome	12	2.626 ±1.158	267 ±60 [22.475]	0.715 ±0.055	0.964 [0.93, 0.98]	R Occipital - R Occipital
MyConnectome	13	3.136 ±0.398	213 ±94 [44.124]	0.804 ±0.084	0.985 [0.97, 0.99]	L Frontal - L Frontal
MyConnectome	14	2.275 ±0.321	139 ±52 [37.507]	0.775 ±0.069	0.988 [0.98, 0.99]	L Frontal - L Frontal
MyConnectome	15	2.231 ±0.564	106 ±43 [40.383]	0.649 ±0.117	0.977 [0.96, 0.99]	R Frontal - R Frontal
MyConnectome	16	2.956 ±0.832	72 ±27 [37.881]	0.663 ±0.081	0.973 [0.95, 0.99]	R Parietal - R Parietal
MyConnectome	17	2.325 ±0.512	97 ±41 [42.347]	0.738 ±0.092	0.968 [0.94, 0.99]	L Parietal - L Parietal
MyConnectome	18	2.528 ±0.362	160 ±47 [29.252]	0.748 ±0.046	0.981 [0.96, 0.99]	L Frontal - L Parietal
MyConnectome	19	2.475 ±0.932	280 ±128 [45.749]	0.728 ±0.129	0.977 [0.95, 0.99]	R Temporal - R Temporal
MyConnectome	20	2.955 ±1.240	292 ±89 [30.303]	0.744 ±0.097	0.989 [0.98, 1.00]	L Frontal - L Frontal
MyConnectome	21	2.335 ±0.618	86 ±34 [39.716]	0.636 ±0.093	0.970 [0.94, 0.99]	R Frontal - R Frontal
MyConnectome	22	2.269 ±0.791	439 ±132 [30.058]	0.863 ±0.065	0.995 [0.99, 1.00]	R Parietal - R Parietal
MyConnectome	23	1.912 ±0.750	475 ±114 [24.010]	0.771 ±0.044	0.990 [0.98, 1.00]	L Temporal - L Temporal
MyConnectome	24	2.060 ±0.637	268 ±60 [22.383]	0.828 ±0.051	0.995 [0.99, 1.00]	R Frontal - R Frontal
MyConnectome	25	2.830 ±0.380	165 ±54 [32.471]	0.805 ±0.080	0.982 [0.96, 0.99]	L Frontal - L Frontal
MyConnectome	26	2.088 ±0.554	130 ±44 [33.653]	0.720 ±0.083	0.976 [0.96, 0.99]	L Frontal - L Frontal
MyConnectome	27	2.236 ±0.284	90 ±36 [39.337]	0.721 ±0.067	0.977 [0.96, 0.99]	L Frontal - L Frontal
MyConnectome	28	2.320 ±0.305	147 ±35 [23.415]	0.829 ±0.052	0.978 [0.96, 0.99]	L Parietal - L Parietal
MyConnectome	29	2.447 ±0.881	333 ±125 [37.613]	0.853 ±0.067	0.987 [0.97, 0.99]	R Parietal - R Temporal
MyConnectome	30	2.571 ±1.034	275 ±108 [39.182]	0.713 ±0.081	0.985 [0.97, 0.99]	R Occipital - R Occipital
MyConnectome	31	2.259 ±0.596	139 ±39 [27.767]	0.670 ±0.042	0.947 [0.89, 0.98]	R Temporal - R Temporal
MyConnectome	32	1.911 ±0.373	68 ±19 [28.599]	0.736 ±0.056	0.980 [0.96, 0.99]	L Frontal - L Parietal
MyConnectome	33	1.987 ±0.633	253 ±60 [23.940]	0.886 ±0.045	0.985 [0.97, 0.99]	R Occipital - R Occipital
MyConnectome	34	2.548 ±0.915	184 ±74 [40.263]	0.679 ±0.086	0.978 [0.96, 0.99]	R Temporal - R Temporal
MyConnectome	35	2.097 ±2.114	257 ±65 [25.315]	0.783 ±0.077	0.983 [0.97, 0.99]	L Occipital - L Occipital
MyConnectome	36	1.207 ±0.511	115 ±30 [25.932]	0.756 ±0.056	0.979 [0.96, 0.99]	L Frontal - L Frontal
MyConnectome	37	3.607 ±0.856	152 ±65 [42.698]	0.813 ±0.079	0.987 [0.98, 0.99]	L Frontal - L Frontal
MyConnectome	38	2.678 ±0.484	156 ±51 [32.666]	0.740 ±0.050	0.970 [0.94, 0.99]	R Frontal - R Frontal
MyConnectome	39	2.255 ±0.716	226 ±103 [45.627]	0.795 ±0.093	0.988 [0.98, 0.99]	L Parietal - L Parietal

A.3 Supplementary table 3

Table S3. Summarized "U"-shaped tract metrics by lobular organization as defined by Freesurfer parcellations, including the number of clusters found between connected lobes. Lobes connected in only one hemisphere appear near the bottom of the list with respect to the hemisphere. Cerebellar connectivity is excluded.

Dataset	Connectivity	No. clusters	Euclidean Distance [mm] (avg ±sd)	Streamline count (avg ±sd) [CV %]	wDSC (avg ±sd)	ICC [95% CI]
MyConnectome	Cerebellum	14	3.833 ±1.044	191 ±197 [27.228]	0.488 ±0.178	0.697 [0.55, 0.83]
MyConnectome	L Frontal - L Cingulate	3	3.424 ±0.485	64 ±41 [14.154]	0.488 ±0.184	0.882 [0.80, 0.94]
MyConnectome	L Frontal - L Frontal	107	2.418 ±0.597	82 ±60 [24.690]	0.602 ±0.166	0.947 [0.91, 0.97]
MyConnectome	L Frontal - L Parietal	22	2.487 ±0.563	56 ±37 [22.634]	0.613 ±0.120	0.948 [0.91, 0.97]
MyConnectome	L Frontal - L Temporal	4	3.144 ±0.802	66 ±40 [25.510]	0.451 ±0.134	0.899 [0.82, 0.95]
MyConnectome	L Occipital - L Occipital	15	2.365 ±0.369	192 ±150 [15.616]	0.714 ±0.117	0.953 [0.92, 0.98]
MyConnectome	L Parietal - L Cingulate	1	1.534 ±0	328 ±0 [0]	0.837 ±0	0.987 [0.98, 0.99]
MyConnectome	L Parietal - L Occipital	4	1.813 ±0.297	81 ±35 [16.380]	0.657 ±0.020	0.973 [0.95, 0.99]
MyConnectome	L Parietal - L Parietal	63	2.525 ±0.703	77 ±56 [27.845]	0.614 ±0.153	0.958 [0.93, 0.98]
MyConnectome	L Parietal - L Temporal	4	2.701 ±0.845	73 ±17 [31.284]	0.608 ±0.091	0.962 [0.93, 0.98]
MyConnectome	L Temporal - L Occipital	1	2.297 ±0	88 ±0 [0]	0.657 ±0	0.930 [0.86, 0.97]
MyConnectome	L Temporal - L Temporal	16	2.627 ±0.731	139 ±120 [27.840]	0.619 ±0.150	0.957 [0.92, 0.98]
MyConnectome	R Frontal - R Cingulate	3	2.625 ±0.575	183 ±62 [21.893]	0.751 ±0.113	0.973 [0.95, 0.99]
MyConnectome	R Frontal - R Frontal	112	2.402 ±0.597	79 ±56 [24.840]	0.620 ±0.153	0.938 [0.90, 0.97]
MyConnectome	R Frontal - R Parietal	24	2.417 ±0.582	61 ±48 [24.082]	0.610 ±0.129	0.936 [0.89, 0.97]
MyConnectome	R Frontal - R Temporal	1	6.722 ±0	618 ±0 [0]	0.679 ±0	0.974 [0.95, 0.99]
MyConnectome	R Occipital - R Occipital	13	2.177 ±0.487	140 ±98 [22.359]	0.653 ±0.138	0.947 [0.90, 0.97]
MyConnectome	R Parietal - R Cingulate	1	3.094 ±0	197 ±0 [0]	0.681 ±0	0.976 [0.95, 0.99]
MyConnectome	R Parietal - R Parietal	73	2.605 ±0.923	66 ±73 [35.423]	0.564 ±0.165	0.942 [0.90, 0.97]
MyConnectome	R Parietal - R Temporal	6	2.971 ±0.737	116 ±111 [24.815]	0.630 ±0.178	0.947 [0.91, 0.97]
MyConnectome	R Temporal - R Cingulate	1	3.715 ±0	332 ±0 [0]	0.577 ±0	0.884 [0.77, 0.95]
MyConnectome	R Temporal - R Temporal	12	2.734 ±0.622	135 ±91 [22.758]	0.617 ±0.095	0.948 [0.91, 0.98]
HCP	Cerebellum	14	3.218 ±1.301	346 ±221 [40.436]	0.668 ±0.146	0.633 [0.44, 0.80]
HCP	L Frontal - L Cingulate	3	3.176 ±0.318	103 ±51 [10.004]	0.471 ±0.083	0.847 [0.74, 0.93]
HCP	L Frontal - L Frontal	107	2.877 ±0.529	117 ±82 [18.371]	0.507 ±0.117	0.894 [0.81, 0.95]
HCP	L Frontal - L Parietal	22	2.749 ±0.728	92 ±52 [26.494]	0.598 ±0.098	0.913 [0.84, 0.96]
HCP	L Frontal - L Temporal	4	4.303 ±1.086	53 ±32 [25.230]	0.367 ±0.053	0.829 [0.71, 0.92]
HCP	L Occipital - L Occipital	15	2.972 ±0.471	266 ±229 [15.844]	0.552 ±0.120	0.875 [0.78, 0.94]
HCP	L Parietal - L Cingulate	1	3.312 ±0	361 ±0 [0]	0.650 ±0	0.953 [0.91, 0.98]
HCP	L Parietal - L Occipital	4	2.778 ±0.521	129 ±91 [18.737]	0.493 ±0.100	0.890 [0.79, 0.95]
HCP	L Parietal - L Parietal	63	3.311 ±0.727	113 ±85 [21.968]	0.462 ±0.117	0.899 [0.82, 0.95]
HCP	L Parietal - L Temporal	4	2.917 ±0.494	111 ±26 [16.940]	0.601 ±0.073	0.886 [0.78, 0.95]
HCP	L Temporal - L Occipital	1	2.657 ±0	108 ±0 [0]	0.484 ±0	0.913 [0.83, 0.96]
HCP	L Temporal - L Temporal	16	2.967 ±0.544	203 ±146 [18.329]	0.549 ±0.080	0.903 [0.81, 0.96]
HCP	R Frontal - R Cingulate	3	2.738 ±0.388	175 ±43 [14.168]	0.576 ±0.042	0.911 [0.83, 0.96]
HCP	R Frontal - R Frontal	112	2.892 ±0.518	104 ±59 [17.903]	0.505 ±0.105	0.879 [0.79, 0.94]
HCP	R Frontal - R Parietal	24	2.706 ±0.692	95 ±69 [25.554]	0.623 ±0.127	0.908 [0.84, 0.95]
HCP	R Frontal - R Temporal	1	5.117 ±0	1432 ±0 [0]	0.727 ±0	0.856 [0.71, 0.94]
HCP	R Occipital - R Occipital	13	2.625 ±0.256	251 ±199 [9.751]	0.549 ±0.119	0.894 [0.79, 0.95]
HCP	R Parietal - R Cingulate	1	2.905 ±0	423 ±0 [0]	0.681 ±0	0.942 [0.88, 0.97]

A.4 Supplementary video 1

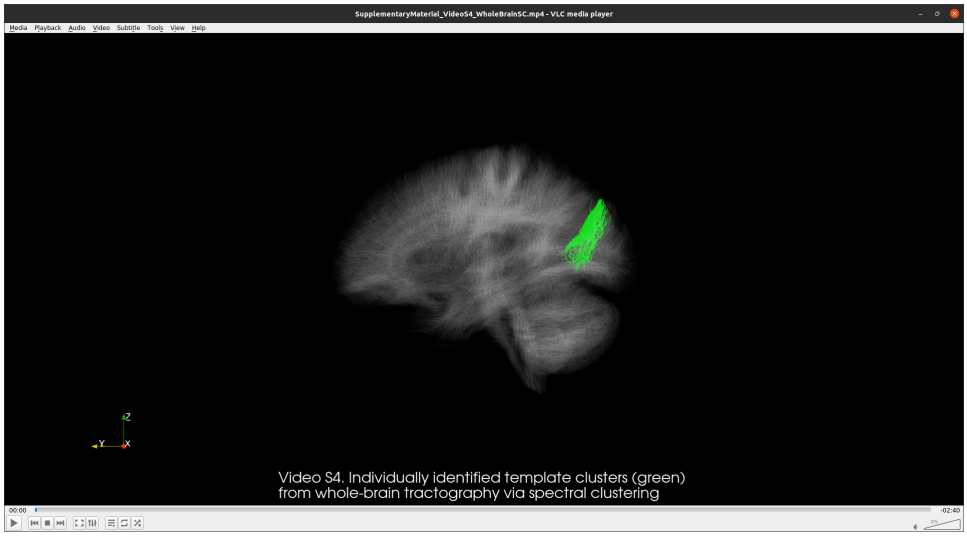

A.5 Supplementary video 2

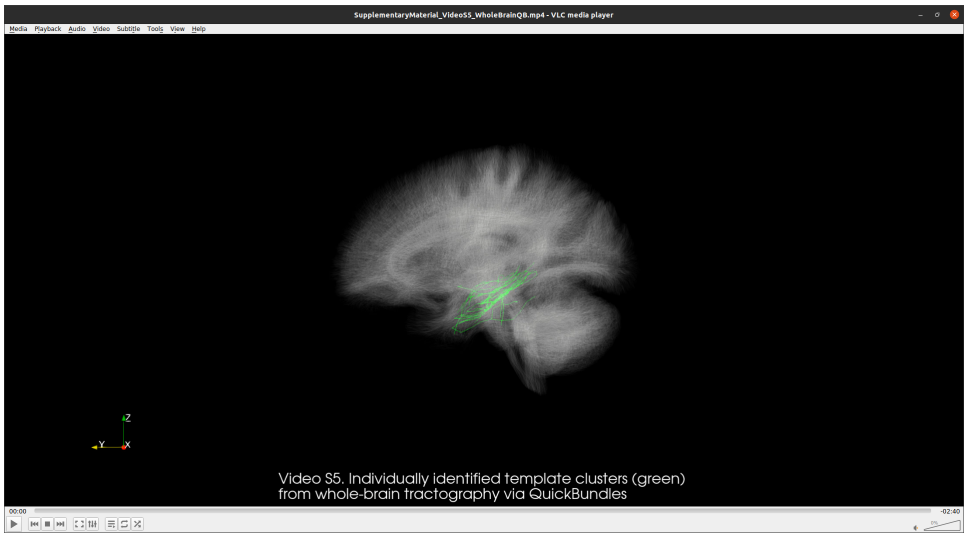

A.6 Supplementary video 3

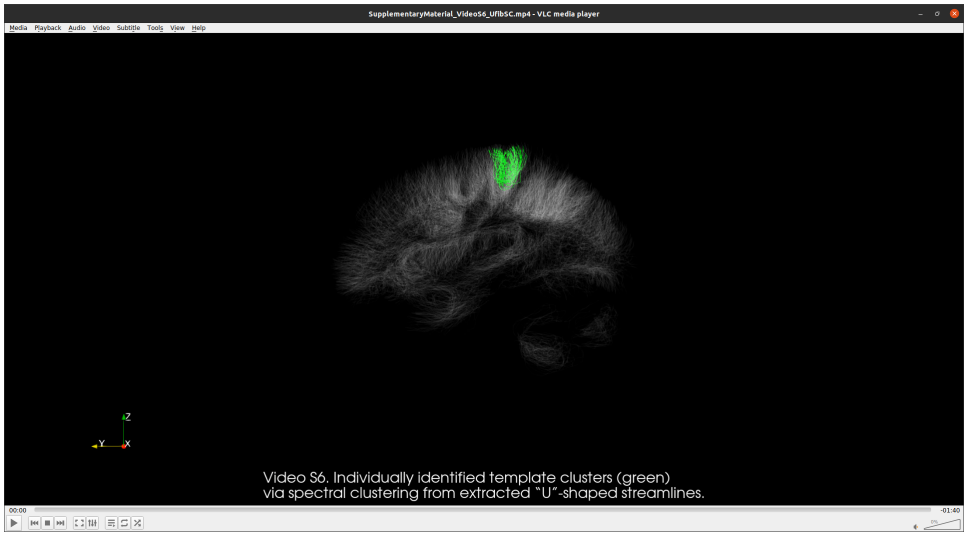

A.7 Supplementary video 4

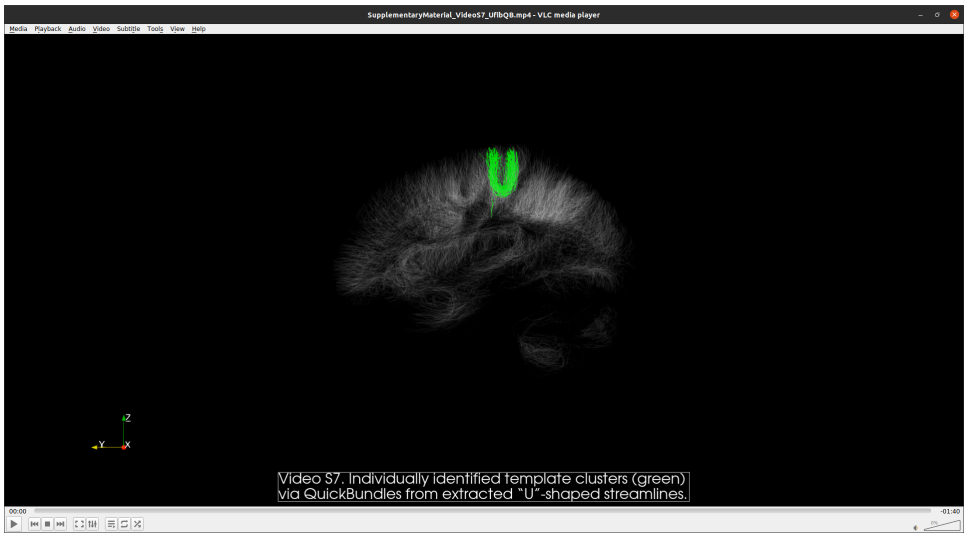

Please refer to original article Kai & Khan (2022) for supplementary tables and to view supplementary videos.

Appendix B

Chapter 3 Supplementary Material

B.1 Supplementary Figure 1

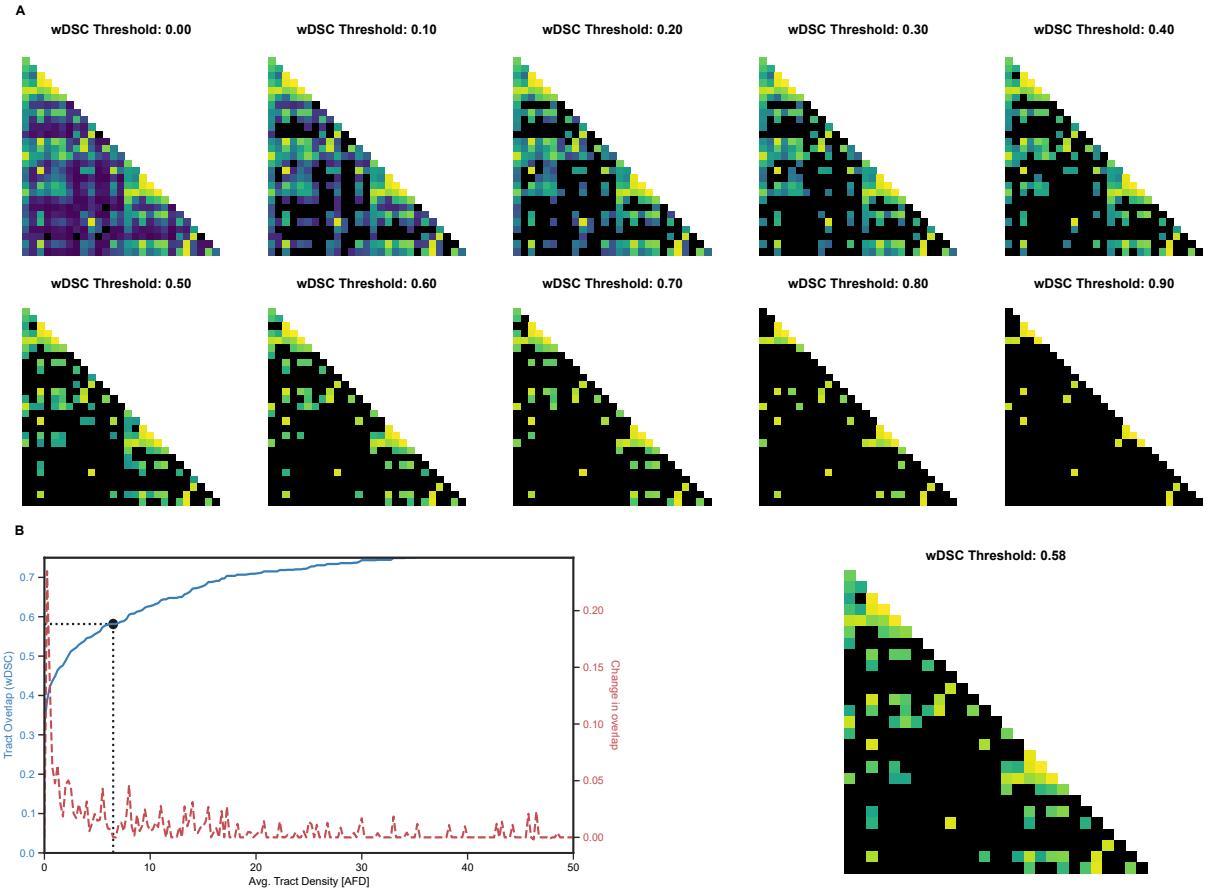

Supplementary Figure B.1. Example of connectivity matrices at difference spatial overlap (wDSC) thresholds. Connections unable to meet the thresholds are discarded and are shown in the connectivity matrices as black boxes.

B.2 Supplementary Figure 2

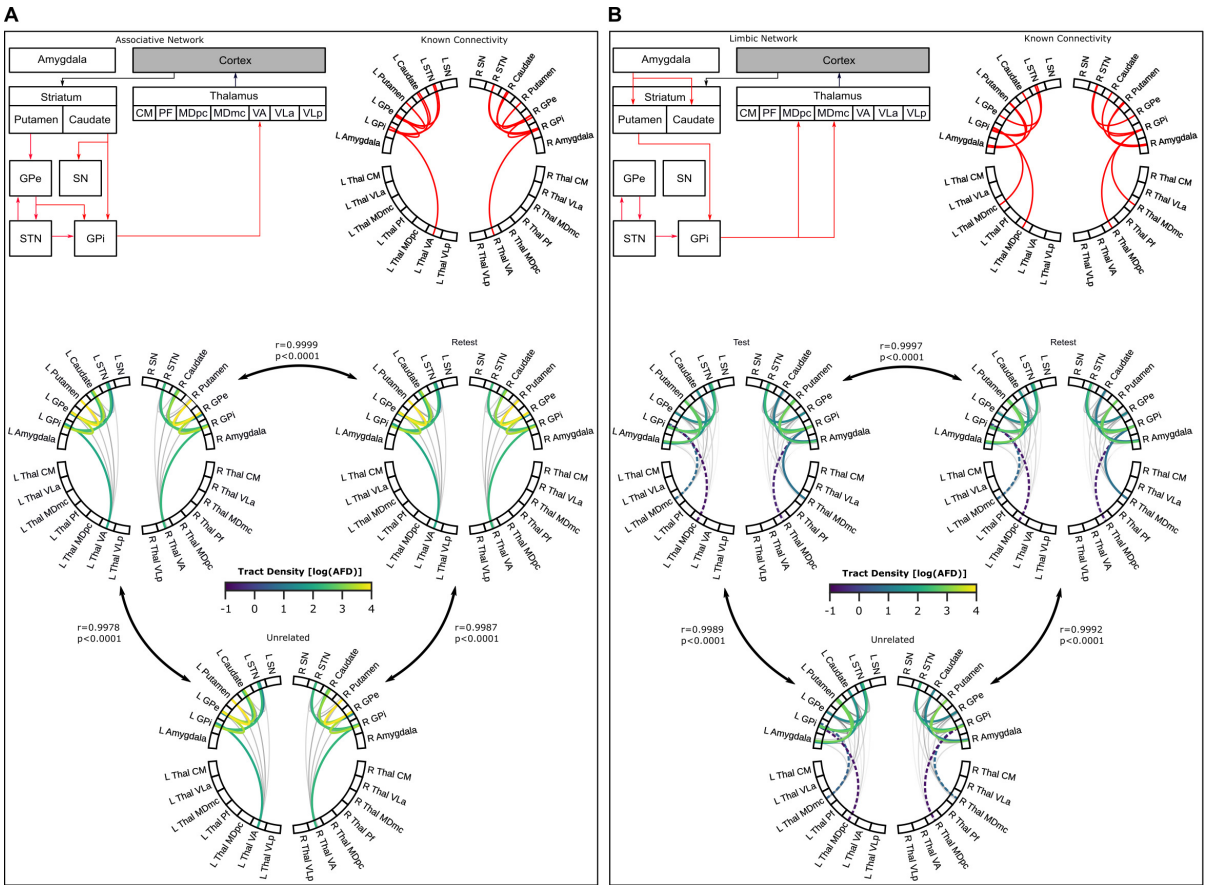

Supplementary Figure B.2. Known subcortical connections (in red) of the (A) associative network and (B) limbic network. For each network, connectivity identified from literature was depicted in a diagram (top-left) and chord plot (top-right), while chord plots exhibit the average log-transformed tract densities for test-retest (middle-left, middle-right) and unrelated (bottom) datasets of the Human Connectome Project. Dashed lines represent connections that did not meet the selected tract density threshold. Pearson correlations between datasets are shown next to the comparison indicators.

B.3 Supplementary Figure 3

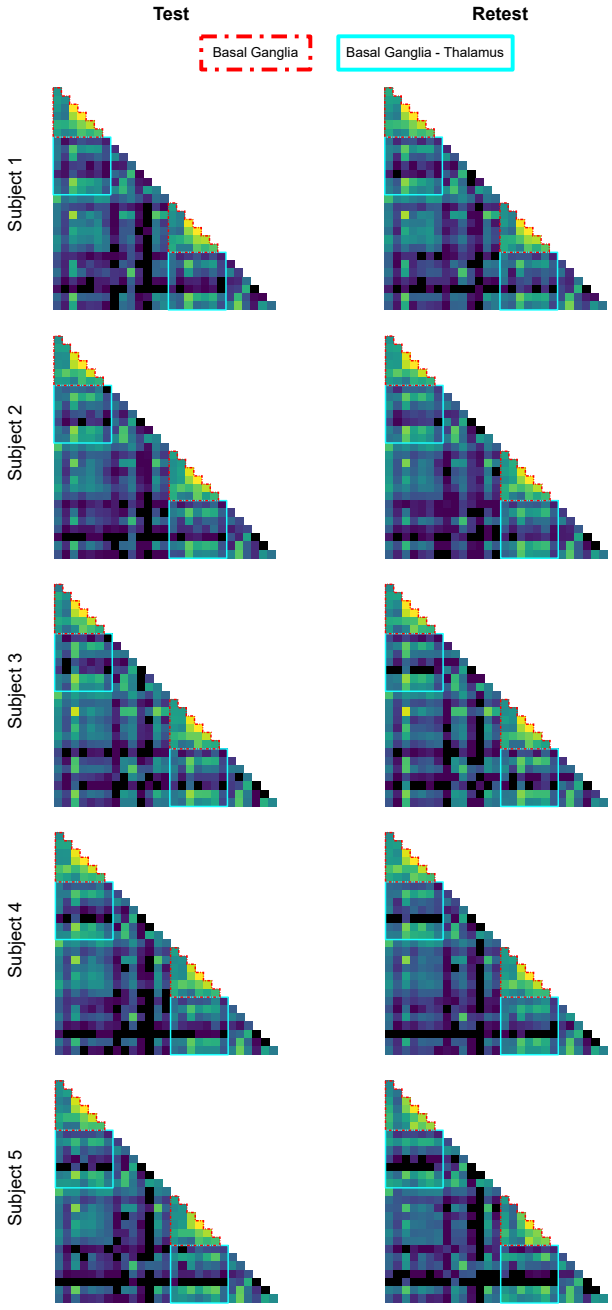

Supplementary Figure B.3. Examples of connectivity matrices exhibiting tract density are shown for 5 different subjects, with connectivity from the test session on the left and retest session on the right. Outlined boxes highlight the connectivity of the basal ganglia (red) and between the basal ganglia and thalamus (cyan).

B.4 Supplementary Figure 4

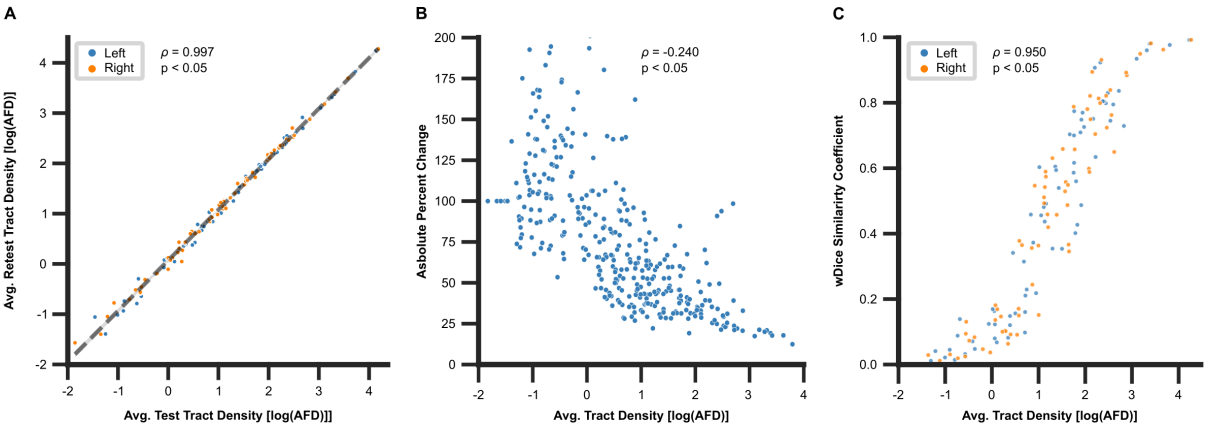

Supplementary Figure B.4 Relationships exhibited between different computed metrics. (A) Linear relationship between the average log-transformed tract density of test vs retest sessions, separated by hemispheric connectivity (B) Negative logarithmic relationship between the absolute percent change of tract density between the two sessions vs the average tract density of the two sessions. (C) Sigmoid relationship identified between the average spatial overlap (wDSC) and the average log-transformed tract density, separated by hemisphere.

B.5 Supplementary Table 1

Supplementary Table B.5. Visual observations of tract trajectories between subcortical structures.

Nodes	Node 1	Node 2	Hemi	Notes
3-9	left substantia nigra	left putamen	Left	- Geting most anterior and posterior tracts; missing trajectory through middle which would have to cut through pallidum - Loop of streamlines going into brainstem; ventral-lateral connectivity to striatum in right hemisphere of some subjects; may be driven by CST - A few streamlines cross mid-plane
5-11	left subthalamic nucleus	left globus pallidus externa	Left	- Projections to limbic (medial; more dense), associative, and motor (lateral) - Some assoc. connectivity may be lost due to GPi presence - Brain stem loop seen
5-13	left subthalamic nucleus	left globus pallidus interna	Left	- Similar projections to GPe - Some brainstem projections again seen
7-11	left caudate	left globus pallidus externa	Left	- Fans onto dorsal surface of GPe, direct connections are plausible - Abherrent projections into brain stem loop - Some cross mid sagittal, go into ventricle (medial to caudate)
7-13	left caudate	left globus pallidus interna	Left	- Direct connections plausible - CST may impact shape - Less dense - Medial to caudate streamlines going into ventricle - Abherent midline projections into brain stem loop
7-19	left caudate	left amygdala	Left	- Direct connection to posterior amygdala - Some projections curve medially to anterior amygdala - Largely driven by CST - Sparse in majority of subjects - Gap seen in some subjects in the middle - Brainstem loop
9-11	left putamen	left globus pallidus externa	Left	- Very dense, plausibility high - Some abherrent projections
9-13	left putamen	left globus pallidus interna	Left	- Not as dense (likely having to deal with GPe) - Some loops and abherent projections - May be running into CST when it loops around GPe
9-19	left putamen	left amygdala	Left	- May be following uncinate fasciculus - Extremely dense
11-13	left globus pallidus externa	left globus pallidus interna	Left	- Direct connectivity - Some loops that are likely false - Brain stem projections
13-37	left globus pallidus interna	left thalamus ventral lateral anterior	Left	- Capturing some of the ansa curvature - FP of brainstem loop and capturing some CST (dense) - Abherent connectivity crossing midline
13-41	left globus pallidus interna	left thalamus mediodorsal medial magnocellular	Left	- Sparse. medial GPi to ventroposterior aspect MD (looks like portion of ansa) - Spurious tracts into brainstem - Does not meet tract density threshold in HCP unrelated dataset

Nodes	Node 1	Node 2	Hemi	Notes
13-47	left globus pallidus interna	left thalamus mediodorsal lateral parvocellular	Left	- Very sparse, even for those found in subjects - Does not meet tract density threshold in any dataset
13-51	left globus pallidus interna	left thalamus ventral anterior	Left	- More associative / limbic (in GPi) - Still capturing some CST (less dense) - Brain stem and some crossing of midline
13-69	left globus pallidus interna	left thalamus ventral lateral posterior	Left	- Medial bend likely real - Some integration of CST, difficult to pinpoint - Abherrent dorsal-lateral loops - Brainstem loops
9-35	left putamen	left thalamus centromedian	Left	- Capturing most lateral and medial aspects - Sparse, could be due to structures in between - Does not meet tract density threshold in any dataset
9-43	left putamen	left thalamus parafascicular	Left	- Very sparse, again could be due to inbetween structures - Does not meet tract density threshold in any dataset
4-10	right substantia nigra	right putamen	Right	- Geting most anterior and posterior tracts; missing middle which would have to cut through GP - Loop of streamlines going into brainstem; ventral-lateral connectivity to striatum in right hemisphere of some subjects (185442); may be driven by CST - A few streamlines cross mid-plane
6-12	right subthalamic nucleus	right globus pallidus externa	Right	- Projections to limbic (medial; more dense), associative, and motor (lateral) - Some assoc. connectivity may be lost due to GPi presence - Brain stem loop seen
6-14	right subthalamic nucleus	right globus pallidus Interna	Right	- Similar projections to GPe - Some brainstem projections again seen
8-12	right caudate	right globus pallidus externa	Right	- Fans onto dorsal surface of GPe, direct connections are plausible - Abherrent projections into brain stem loop - Some cross mid sagittal, go into ventricle (medial to caudate)
8-14	right caudate	right globus pallidus Interna	Right	- Direct connections plausible - CST may impact shape - Less dense - Medial to caudate streamlines going into ventricle - Abherent midline projections into brain stem loop
8-20	right caudate	right amygdala	Right	- Direct connection to posterior amygdala - Some projections curve medially to anterior amygdala - Largely driven by CST - Sparse in majority of subjects - Gap seen in some subjects in the middle - Brainstem loop
10-12	right putamen	right globus pallidus externa	Right	- Very dense, plausibility high - Some abherrent projections

Nodes	Node 1	Node 2	Hemi	Notes
10-14	right putamen	right globus pallidus Interna	Right	- Not as dense (likely having to deal with GPe) - Some loops and abherent projections - May be running into CST when it loops around GPe
10-20	right putamen	right amygdala	Right	- May be following uncinate fasciculus - Extremely dense
12-14	right globus pallidus externa	right globus pallidus Interna	Right	- Direct connectivity - Some loops that are likely false - Brain stem projections
10-36	right putamen	right thalamus centromedian	Right	- Capturing most lateral and medial aspects - Sparse, could be due to structures in between - Does not meet tract density threshold in any dataset
10-44	right putamen	right thalamus parafascicular	Right	- Very sparse, again could be due to inbetween structures - Does not meet tract density threshold in any dataset
14-38	right globus pallidus Interna	right thalamus ventral lateral anterior	Right	- Capturing some of the ansa curvature - FP of brainstem loop and capturing some CST (dense) - Abherent connectivity crossing midline
14-42	right globus pallidus Interna	right thalamus mediodorsal medial magnocellular	Right	- Sparse. medial GPi to ventroposterior aspect MD (looks like portion of ansa) - Spurious tracts into brainstem - Does not meet tract density threshold in HCP unrelated dataset
14-48	right globus pallidus Interna	right thalamus mediodorsal lateral parvocellular	Right	- Very sparse, even for those found in subjects - Does not meet tract density threshold in any dataset
14-52	right globus pallidus Interna	right thalamus ventral anterior	Right	- More associative / limbic (in GPi) - Still capturing some CST (less dense) - Brain stem and some crossing of midline
14-70	right globus pallidus Interna	right thalamus ventral lateral posterior	Right	- Medial bend likely real - Some integration of CST, difficult to pinpoint - Abherrent dorsal-lateral loops - Brainstem loops

B.6 Supplementary Materials - Results from HCP unrelated dataset

B.6.1 Networks of the subcortical connectome

Known connections within the networks of interest (i.e. motor, associative, and limbic) were examined for the HCP unrelated dataset. Figure 3.2 demonstrated the connectivity and the associated AFDs for the assessed motor network (see Supplementary Figure B.2A and Supplementary Figure B.2B for associative and limbic network). Using the same threshold of 6.5 AFD previously determined, connectivity was observed to be similar to both sessions of the test-retest dataset. 78% (14 out of 18) of the known connections of the motor network met the previously determined threshold, while 100% and 71% (10 out of 14) connections of the associative and limbic networks satisfied the threshold respectively. Moderate density between subcortical structures of interest were observed except with certain thalamic nuclei as before. The same subcortical connections which had previously failed to meet the tract density threshold also failed to meet the threshold for the HCP unrelated dataset. Visual inspection of connectivity noted identical observations as with the test-retest dataset with shorter, more direct connections between basal ganglia structures, and longer connections with a more curved trajectory between the basal ganglia and thalamus.

B.6.2 Reliability of the HCP unrelated dataset

Connectivity matrices were first created for subjects of the HCP unrelated dataset, before an average AFD matrix across subjects was computed and examined (Supplementary Figure B.6A). Furthermore, a box plot of the AFD exhibited in each hemisphere was created and overlaid by a swarmplot of individual AFDs between subcortical structures of interest (Supplementary Fibre B.6B). A visual comparison with similar plots created for the test-retest dataset suggested comparable connectivity being demonstrated in the unrelated subjects. A Pearson's correlation was performed between the average AFD of the unrelated dataset and the average AFD for the test and retest sessions respectively, where a Pearson's correlation coefficient of 0.99 was exhibited against both test ($p < 0.05$) and retest sessions ($p < 0.05$).

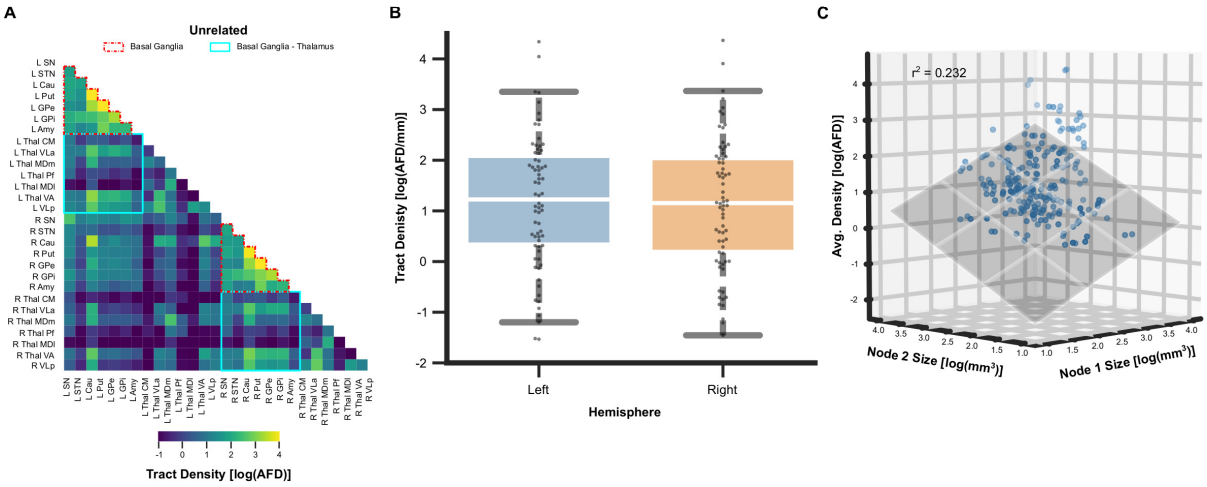

Supplementary Figure B.6 (A) Log-transformed average tract density of the HCP unrelated subjects are shown in a connectivity matrix, visualizing connectivity between subcortical structures of known subcortical networks. (B) The tract density, exhibited in a box plot and overlaid with a swarmplot to exhibit individual AFDs, is separated by hemispheric connectivity. The middle line of the boxplot marks the median metric, while whiskers define the maximum and minimum values of each metric, excluding outliers. Average tract densities similar to those previously exhibited in both HCP test and retest sessions. (C) A 3-dimensional scatterplot is shown, observing the relationship between the average tract density of connections and the volume of the terminal nodes. A similar relationship to that from the test-retest dataset was observed.

The AFD was evaluated against the size of the two connecting subcortical structures for the unrelated dataset. A positive linear relationship was observed (Supplementary Figure B.6C; $r^2 = 0.232$, $p < 0.05$), with an increase in average TD associated with an increase in size of one or both subcortical structures, demonstrating a positive linear relationship when an ordinary least squares regression was performed.

Appendix C

Chapter 4 Supplementary Material

The following document provides a more in-depth statistical analysis of the segments demonstrating significant differences between controls and patients with first-episode schizophrenia (FES) along the length of identified aberrant tracts.

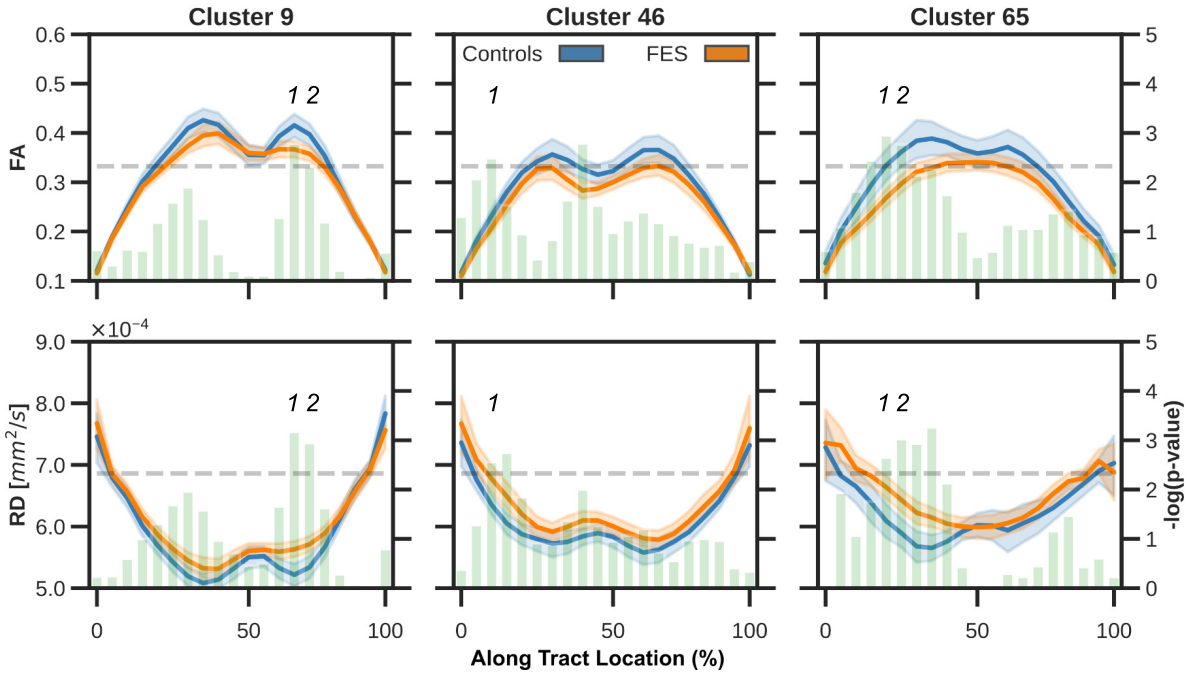

Supplementary Figure C.1. Along-tract measures for fractional anisotropy (FA) and radial diffusivity (RD) for controls and patients with FES. Segments exhibiting differences in both FA and RD are indicated by the number above, corresponding with segments from Supplementary Table C.1.

Supplementary Table C.1. Observed t-statistic and p-value from segments demonstrating differences from both along-tract FA and RD. Segment numbers correspond with the segments shown in Supplementary Figure C.1.

		Cluster 9		**Cluster 46**		**Cluster 65**	
Metric	**Segment**	t-stat	p-val	t-stat	p-val	t-stat	p-val
FA	1	3.337	0.00164	3.092	0.00323	3.600	0.00110
	2	2.962	0.00472			3.443	0.00170
MD	1	-3.638	0.000667	-3.126	0.00273	-3.284	0.00221
	2	-3.469	0.00113			-3.555	0.000943

Supplementary Table C.2. Correlations between DTI-derived measures (from aberrant segments along-tract) and cognitive measures in patients with first-episode schizophrenia. MD of tract 9 and AD not included (no identified aberrant segments).

Variable	**Tract 9** **FA**			**RD**			**MD**		
	r	$p_{uncorrected}$	$p_{corrected}$	r	$p_{uncorrected}$	$p_{corrected}$	r	$p_{uncorrected}$	$p_{corrected}$
Trail Making Time	-0.0613	0.842	0.949	-0.135	0.659	0.911			
Trail Making Error	0.0191	0.951	0.962	-0.187	0.542	0.911			
Category Fluency	0.406	0.169	0.845	-0.327	0.276	0.845			
	Tract 46								
Trail Making Time	0.505	0.137	0.845	-0.486	0.155	0.845	-0.302	0.396	0.911
Trail Making Error	0.726	0.0175	0.690	-0.446	0.196	0.845	-0.180	0.619	0.911
Category Fluency	-0.132	0.717	0.921	0.0559	0.0878	0.962	0.0499	0.891	0.962
	Tract 65								
Trail Making Time	-0.0801	0.815	0.949	-0.243	0.472	0.911	-0.433	0.183	0.845
Trail Making Error	-0.0255	0.941	0.962	-0.168	0.620	0.911	-0.235	0.486	0.911
Category Fluency	0.0954	0.780	0.949	0.252	0.455	0.911	0.366	0.268	0.845

r: Pearson's correlation coefficient;

Appendix D

Ethics Approvals

D.1 Psychosis Study

Western Research

Date: 30 September 2020

To: Dr. Lena Palaniyappan

Project ID: 108268

Study Title: The Pathophysiology of Thought Disorder in Psychosis (TOPSY)

Application Type: Continuing Ethics Review (CER) Form

Review Type: Delegated

REB Meeting Date: 20/Oct/2020

Date Approval Issued: 30/Sep/2020

REB Approval Expiry Date: 24/Oct/2021

Dear Dr. Lena Palaniyappan,

The Western University Research Ethics Board has reviewed the application. This study, including all currently approved documents, has been re-approved until the expiry date noted above.

REB members involved in the research project do not participate in the review, discussion or decision.

Western University REB operates in compliance with, and is constituted in accordance with, the requirements of the TriCouncil Policy Statement: Ethical Conduct for Research Involving Humans (TCPS 2); the International Conference on Harmonisation Good Clinical Practice Consolidated Guideline (ICH GCP); Part C, Division 5 of the Food and Drug Regulations; Part 4 of the Natural Health Products Regulations; Part 3 of the Medical Devices Regulations and the provisions of the Ontario Personal Health Information Protection Act (PHIPA 2004) and its applicable regulations. The REB is registered with the U.S. Department of Health & Human Services under the IRB registration number IRB 00000940.

Please do not hesitate to contact us if you have any questions.

Sincerely,

The Office of Human Research Ethics

Note: This correspondence includes an electronic signature (validation and approval via an online system that is compliant with all regulations).

Western Research

Date: 2 March 2022

To: Dr. Hooman Ganjavi

Project ID: 108268

Study Title: The Pathophysiology of Thought Disorder in Psychosis (TOPSY)

Study Sponsor: Lawson HRI

Application Type: HSREB Amendment Form

Review Type: Delegated

Meeting Date / Full Board Reporting Date: 15/Mar/2022

Date Approval Issued: 02/Mar/2022

REB Approval Expiry Date: 24/Oct/2022

Dear Dr. Hooman Ganjavi ,

The Western University Health Sciences Research Ethics Board (HSREB) has reviewed and approved the WREM application form for the amendment, as of the date noted above.

Documents Approved:

Document Name	Document Type	Document Date
TOPSY LOI FEP FEBRUARY 9, 2022	Consent Form	09/Feb/2022
TOPSY LOI HEALTHY CONTROLS FEBRUARY 9, 2022	Consent Form	09/Feb/2022
TOPSY LOI High Risk February 9, 2022	Consent Form	09/Feb/2022
Protocol TOPSY 9_Feb_2022	Summary of Changes	

Documents Acknowledged:

Document Name	Document Type	Document Date
Summary of Changes	Summary of Changes	17/Feb/2022

REB members involved in the research project do not participate in the review, discussion or decision.

The Western University HSREB operates in compliance with, and is constituted in accordance with, the requirements of the TriCouncil Policy Statement: Ethical Conduct for Research Involving Humans (TCPS 2); the International Conference on Harmonisation Good Clinical Practice Consolidated Guideline (ICH GCP); Part C, Division 5 of the Food and Drug Regulations; Part 4 of the Natural Health Products Regulations; Part 3 of the Medical Devices Regulations and the provisions of the Ontario Personal Health Information Protection Act (PHIPA 2004) and its applicable regulations. The HSREB is registered with the U.S. Department of Health & Human Services under the IRB registration number IRB 00000940.

Please do not hesitate to contact us if you have any questions.

Sincerely,

Patricia Sargeant, Ethics Officer [redacted] on behalf of Dr. Philip Jones, HSREB Chair

Note: This correspondence includes an electronic signature (validation and approval via an online system that is compliant with all regulations).

Appendix E

Copyright Transfers and Reprint Permissions

The reprint permissions for the following accepted articles are provided:

The following accepted articles which I have primarily authored are open access:

- Chapter 2: Kai, J. & Khan, A.R. (2022). Assessing the reliability of template-based clustering for tractography in healthy human adults. Frontiers in Neuroinformatics.
- Chapter 3: Kai, J., Khan, A.R., Haast, R.A.M., Lau, J.C. (2022). Mapping the subcortical connectome using in vivo diffusion MRI: feasibility and reliability. Terra incognita: diving into the human subcortex, special issue of NeuroImage.

All other copyright material is under sole ownership by the author, including arXiv pre-prints, and articles currently under submission or revision.

Jason Kai | Curriculum Vitae

EDUCATION

Doctor of Philosophy, Medical Biophysics — 2016 - Present
Western University, London, ON, Canada

Bachelor of Engineering, Electrical and Biomedical Engineering — 2011 - 2016
McMaster University, Hamilton, ON, Canada
Summa cum laude

PUBLICATIONS

Kai, J., Mackinley, M., Khan, A.R., Palaniyappan, L. (Submitted) **Aberrant frontal lobe "U"-shaped association fibers in first-episode schizophrenia: A 7-Tesla diffusion imaging study**.

Hossain, N., Kai, J., Sallam, Y., Khan A.R., Gofton, T.E. (Submitted) **Rate of cerebral atrophy after super refractory status epilepticus is associated with clinical outcome**.

Gui, C., Kai, J., Khan, A.R., Lau, J.C., Megyesi, J.F. (Submitted) **Detection of local growth patterns in longitudinally imaged low-grade gliomas using deformating-based morphometry**.

Kai, J., Khan, A.R., Haast R.A.M., Lau, J.C. (2022, Aug) **Mapping the subcortical connectome using in vivo diffusion MRI: feasibility and reliability**. *Terra incognita: diving into the human subcortex*, special issue of *NeuroImage*. doi: 10.1016/j.neuroimage.2022.119553

Kai, J., Khan, A.R. (2022, Feb) **Assessing the reliability of template-based clustering for tractography in healthy human adults**. *Frontiers in Neuroinformatics*. doi:10.3389/fninf.2022.777853

Gau, R., Noble, S., Heuer, K., ..., Kai, J., et al. (2021, Jun) **Brainhack: developing a culture of open, inclusive, community-driven neuroscience**. *Neuron*. doi:10.1016/j.neuron.2021.04.001.

Arbabi, A., Kai, J., Khan, A.R., Baron, C.A. (2019, Nov) **Diffusion Dispersion Imaging: Mapping OGSE Frequency Dependence in the Human Brain**. *Magnetic Resonance in Medicine*. doi:10.1002/mrm.28083

Lau, J.C., Parrent, A.G., Demarco, J., Gupta, G., Kai, J., Stanley, O.W., Kuehn, T, Park, P.J., Ferko, K., Khan, A.R., Peters, T.M. (2019, Jun) **A framework for evaluating correspondence between brain images using anatomical fiducials**. *Human Brain Mapping*. doi:10.1002/hbm.2469

TALKS

Kai, J., Khan, A.R. (2019, Mar) **Assessing the reliability and reproducibility of NeuroBundle Extraction and Evaluation Resource, an automated tool for clustering diffusion tractography**. In *Proceedings of the 17th annual meeting of Imaging Network Ontario. pp 105.* London, ON, Canada

Kai, J., Kasa, L.W., Peters, T.M., Khan, A.R. (2018, Jun) **Investigating U-shape fibers from data-driven clustering of white matter tractography**. In *Pro-*

ceedings of the 26th annual meeting of International Society for Magnetic Resonance in Medicine. pp 43. Paris, France.

Kai, J., Kasa, L.W., Peters, T.M., Khan, A.R. (2018, Apr) **Investigating quantitative and structural differences in short association, U-shaped fibres in temporal lobe epilepsy**. In *CNS Research Day.* London, ON, Canada.

Kai, J., Kasa L.W., Khan, A.R. (2017, Mar) **Investigating the relationship of myelin and axonal white matter microstructure using longitudinal relaxation mapping and restricted diffusion**. In *Proceedings of the 15th annual meeting of Imaging Network Ontario. pp 93.* London, ON, Canada.

Kai, J., Khan, A.R. (2016, Nov). **Toward automated white matter parcellation using multi-parametric quantitative data**. In *Epilepsy Research Day.* London, ON, Canada.

POSTERS

Taylor, M., Kai, J., Haast, R.A.M., Nouri, M.N., Khan, A.R. (2022, Jun). **Exploratory analysis of structure-function coupling changes following temporal lobe epilepsy surgery**. In *2022 Organization for Human Brain Mapping.* Glasgow, Scotland.

Nichols, E.S., Van Dyken, P., Kai, J., Kuehn, T., Correa, S., Mueller, M.E., Al-Saoud, S., Ubhi, T., Papadopoulos, A., Christiaans, E., de Ribaupierre, S., Duerden, E.G., Khan A.R. (2022, Jun). **Funcmasker-flex: an automated BIDS-App for brain segmentation of fetal functional MRI data**. In *2022 Organization for Human Brain Mapping.* Glasgow, Scotland.

Kai, J., Khan A.R., Haast, R.A.M., Lau, J.C. (2022, Jun). **Mapping the subcortical connectome using in vivo diffusion MRI: assessing reliability**. In *2022 Organization for Human Brain Mapping.* Glasgow, Scotland.

Kai, J., Khan A.R., Palaniyappan, L. (2022, Apr). **Examining changes to frontal lobe superficial white matter in first episode schizophrenia**. In *2022 Annual Congress of Schizophrenia International Research Society.* Florence, Italy.

Kai, J., Khan, A.R., Haast, R.A.M., Lau, J.C. (2021, Jun). **Assessing the reliability of subcortical-subcortical structural connectivity**. In *2021 Organization for Human Brain Mapping Meeting.* Virtual.

Kai, J., Khan, A.R. (2020, Jun). **Towards identifying reliable short-ranged, "U"-shaped structural connectivity**. In *2020 Organization for Human Brain Mapping Meeting.* Virtual.

Park, P.J., Kai, J., Kuehn, T., Stanley, O., Gilmore, G., Loree-Spacke, J., Gupta, G., Ferko, K., Mustaha, F., Peters, T.M., Khan, A.R., Lau, J.C. (2020, Jun). **A Web Application for Quality Control of Anatomical Fiducials (AFIDs) and Teaching Neuroanatomy**. In *2020 Organization for Human Brain Mapping Meeting.* Virtual.

Kai, J., Khan, A.R. (2020, Mar). **Towards identifying reliable short-ranged, "U"-shaped structural connectivity**. In *Proceedings of the 17th annual meeting of Imaging Network Ontario.* Virtual.

Kai, J., Khan, A.R. (2019, May). **Development of a diffusion magnetic res-**

onance imaging template for investigating short-ranged U-shaped structural connectivity in the human adult brain. In *13th Annual Canadian Neuroscience Meeting*. Toronto, ON, Canada.

Kai, J., Kasa, L.W., Peters, T.M., Khan, A.R. (2018, May) **Investigating quantitative and structural differences in short association, U-shaped fibres in temporal lobe epilepsy**. In *London Health Research Day*. London, ON, Canada.

Kai, J., Kasa, L.W., Peters, T.M., Khan, A.R. (2018, Mar) **Investigating quantitative and structural differences in short association, U-shaped fibres in temporal lobe epilepsy**. In *Proceedings of the 16th annual meeting of Imaging Network Ontario. pp 113*. London, ON, Canada.

Kai, J., Kasa, L.W., Khan, A.R. (2017, Mar) **Investigation into the relationship of myelin and axonal white matter microstructure using longitudinal relaxation mapping and restricted diffusion**. In *London Health Research Day*. London, ON, Canada.

Park, P.J., Kai, J., Lau, J.C., Khan, A.R. (2016, Nov). **Nipype: building pipelines for reproducible neuroimaging research**. In *Epilepsy Research Day*. London, ON, Canada

TEACHING EXPERIENCE

Teaching Assistant 2017-2021
Western University

Teaching Assistant 2019-2020
Scinet Summer School

HONORS & AWARDS

NSERC Postgraduate Scholarships Doctoral Program 2020 - 2022
Western University

CONP Student Scholar 2019
Western University

ISMRM Summa cum laude abstract 2018
Western University

ISMRM Trainee (Educational) Stipend 2018
Western University

Ontario Graduate Scholarship (OGS) 2017 - 2018
Western University

Brainhack Travel Award 2017
Western University

ImNO, 2nd Place Oral Presentation 2017
Western University

McMaster University Dean's List 2012 - 2016
McMaster University

The University (Senate) Scholarship 2015
McMaster University

McMaster Entrance Scholarship, Level II 2011
McMaster University